PRISM CLEANROOM
RESEARCH REPORT
2019
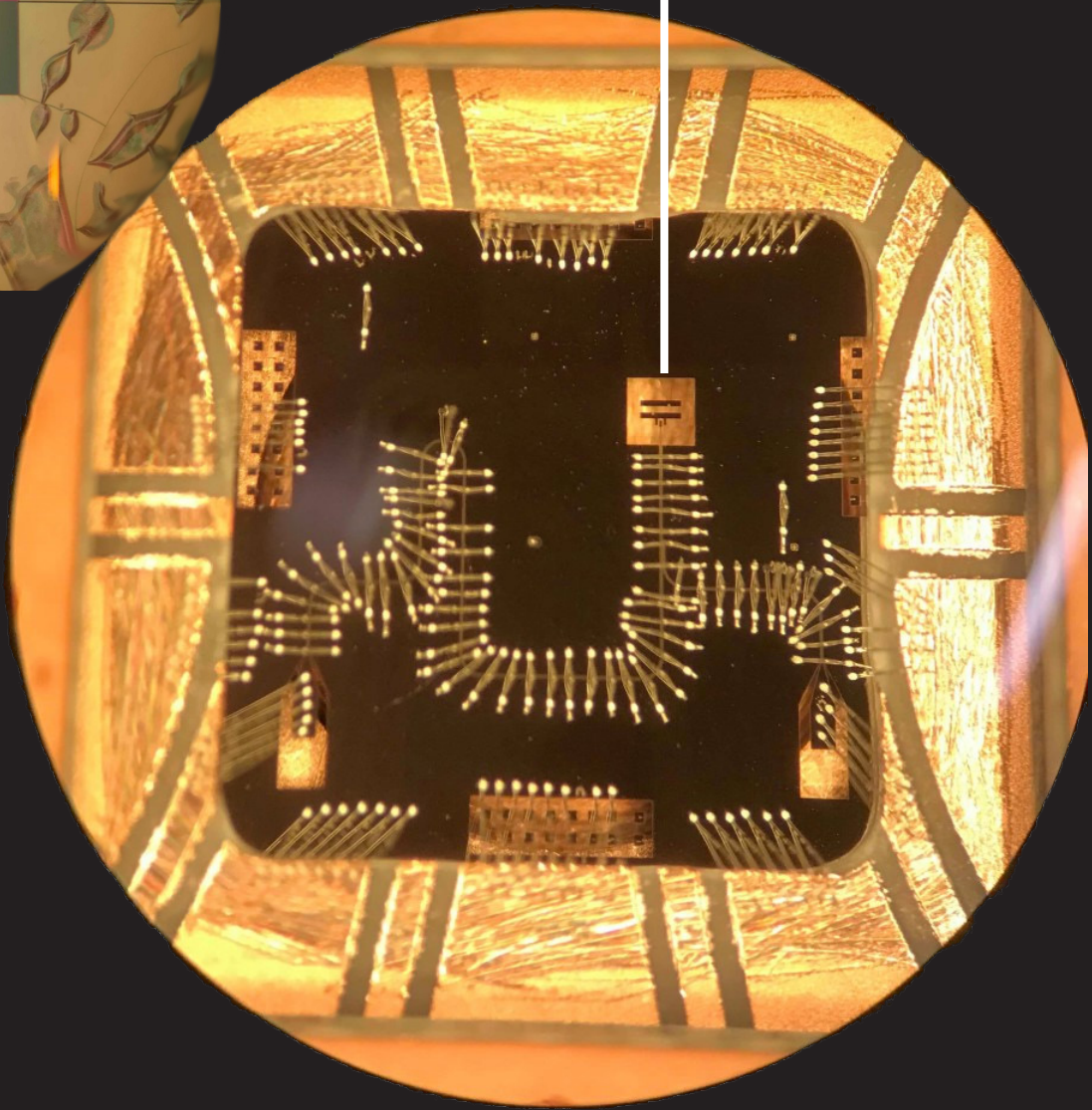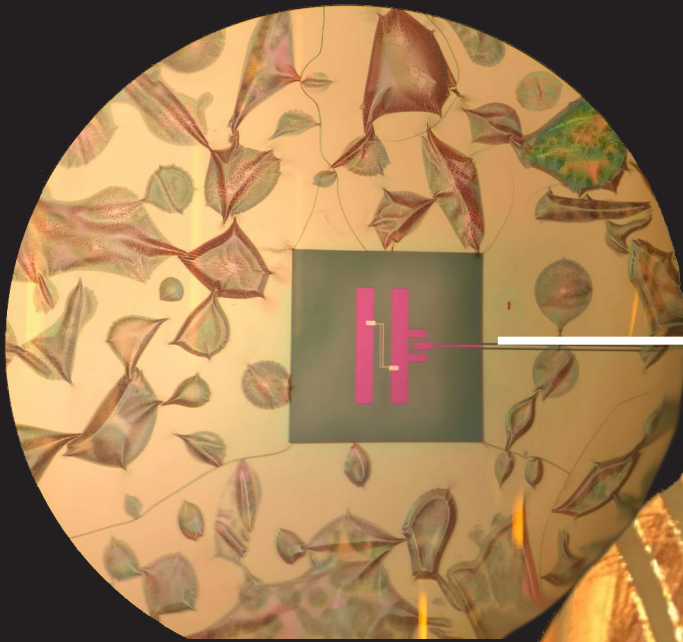
Dear PRISM Cleanroom PI's, Researchers, Labmembers and Stakeholders,

Thanks to tremendous financial support from PRISM, SEAS AND APEC, this year brought several milestones to our transition from a cleanroom microfabrication facility to a micro/nano/quantum research facility:

- We have added highly experienced personnel to our now-complete staff, and are available to support and answer questions, providing better training to our labmembers

- We expanded our Packaging Lab capabilities (scribing, wire bonding, flip-chip upgrade) and implemented ESD protocol

- We installed two versatile new metrology tools: Keyence VHX-6000 (great for color images of devices at various magnification and tilt, with high topography and everything in focus; and VK 1000 laser scanning confocal measuring microscope (UV source for high resolution)

- We have just qualified a brand new, user configurable sputtering tool

- We have completely overhauled two of our older PVD tools and are working on a third, so that we have good base vacuum and excellent deposition purity

- Our ICP-CVD tool is rebuilt and re-qualified with process trend history for materials properties

- We have implemented several safety and productivity improvements including breathable, re-usable gowns and more tactile gloves for better acid handling

- We have completed a year of usage data collection with our NEMO lab management system, enabling more accurate facility costing prediction and tool utilization assessment

Over the coming year we look forward to:
- Qualifying our new high-speed, hi-resolution, hi-accuracy-stitching EBL tool, the Raith EBPG 5150 (est. qualified June, 2020)

- Rebuilding our hazardous exhaust remediation system, installing oil-free vacuum pumps and completing an all-surface superclean and wipe-down of the facility

- Installing and qualifying two new etch tools for precision etch of Si and III-V materials (est. Fall, 2020)

- Installing systems to monitor critical water quality, flow and temperature for process cooling water and highly purified water

We appreciate your patience as we strive to continually improve the tools, infrastructure and expertise that support the world class research occurring here.

Please take a few moments to read through the report highlighting Princeton research utilizing the PRISM Cleanroom.

Thank you,

—Ian R. Harvey, Ph.D.
PRISM Cleanroom Director

TABLE OF CONTENTS

TABLE OF CONTENTS

TABLE OF CONTENTS

DEPOSITION - PVD
- Angstrom sputter (3x4"; Nb, Al, Ti)
- Angstrom sputter (4x4" configurable: Al, Cr, Ti, AlNiCo, Mo, Ho, Al 1% Si, Co, Ge, Au, Pt, Ni)
- Angstrom sputter (3x3" configurable: CoO, MnO, NiO, ZnO, ZnO w/ 2% Al_2O_3, Fe_2O_3, SiO_2, TiO_2, Al_2O_3)
- Angstrom dual chamber e-beam evaporator, six dedicated pockets (Ti, Pt, Au, Ni, Ge, Al) for precision e-beam lift-off
- Denton e-beam evaporator (four pockets; In, dielectrics, Ti, Sn, Ag, Al, Pt, Ge, Ni, Au, SiO_2, Si, Cr, Cu)
- Angstrom Nexdep e-beam evaporator (six pockets, *NO* In, Cu, Sn, dielectrics)
- Angstrom Covap thermal evaporator (dedicated Ti, Au, Cr, Al)
- Edwards evaporation (thick Indium for flipchip)

PLASMA ETCH
- PlasmaTherm Versaline Si precision etch for vertical, smooth sidewalls, no foot (pending)
- PlasmaTherm APEX GaAs on GaAlAs precision etch for vertical, smooth sidewalls, (pending)
- PlasmaTherm APEX SLR metal etcher: Cl_2, BCl_3, Ar, O_2, SF_6, and CHF_3
- PlasmaTherm APEX SLR diamond etcher: Cl_2, O_2, H_2, N_2, and Ar
- SAMCO 200iPB RIE (III-V and compound semiconductor); Cl_2, BCl_3, $SiCl_4$, Ar, and O_2
- SAMCO 800iPB Deep RIE (Si) Through-Si; SF_6, C_4F_8, O_2, CF_4, and Ar
- TePla M4L isotropic asher; O_2, Ar, and CF_4
- PlasmaPro 80 RIE; SF_6, CF_4, CHF_3, O_2, Ar, and N_2 use: Si, SiO_2, SiN_x, SiC, Al, Al_2O_3
- PlasmaTherm 720 SLR RIE shallow etching of Si, SiO2, SiN_x, some metals, and III/V's: Cl_2, BCl_3, H_2, Ar, O_2, SF_6, CF_4

ALD, CVD & THERMAL PROCESSES
- Cambridge ALD thermal Al_2O_3, HfO_2, TiO_2
- Oxford PlasmaPro ICPCVD SiO_2, SiN_x, α-Si
- RTP: one each: Si, III-V; forming gas
- RCA processing hood; Semi-Tool SRD's
- Tube Furnaces: w/d ox, solid state diff., anneal

NANO & MICRO LITHOGRAPHY
- Raith EBPG 5150; 100keV; 125 MHz; 1mm field
- Raith E-Line e-beam writer, 5-30keV
- Heidelberg DWL66+ with grayscale and backside alignment, 900nm and 2μm
- Nanonex Nanoimprinter
- Suss MA6, MJB4; Cr etch; HMDS prime

CHARACTERIZATION & METROLOGY
- Hitachi S-4700 FESEM
- Keyence VHX-6000; VK-1000 (UV) 3D imaging and laser metrology systems
- KLA Tencor P-15 Profilometer, Gaertner Ellipsometer, Filmetrix Reflectometer
- light-tight probe station and supporting tools

PACKAGING Lab (ESD protocols in place)
- ADT Dicing Saw (taping, UV curing tools)
- Wire Bonding: K&S Ball/Wedge, Questar Wedge, West-Bond Ball-Wedge
- Logitech Lapping/Polishing System
- West-Bond Manual Epoxy Die Bonder
- Tresky automated Flip Chip bonder
- Loomis LSD-100 scribe tool

SOFT MATERIALS & MICROFLUIDICS
- Heidelberg microPG101 (direct laser patterning of SU-8, 2μm and 5μm)
- Dimatics suspended nanoparticle and protein printer
- SCS Parylene coating
- PDMS Processing Tools, Plasma surface activation and wet processing, UV / ozone cleaning
- Critical point dryer, VWR 1410 Vacuum Oven, KLA Tencor D-120 Profilometer
- FormLabs Form2 3D prototyping (plastic)

STAFF SERVICES
- Microfluidics concept / simulate / design / fabricate / test support
- Process and architectural design using cleanroom tools

ACADEMIC TRACK:

- ➢ MSE 305 Engineering in the Micro/Nano Maker Space
    - o Course Instructor: Ian R. Harvey, Ph.D.
    - o Lab co-Instructors: Eric Mills, Ph.D., Phil Hochendoner, Ph.D.

- ➢ ELE 308 Electronic and Photonic Devices
    - o Course Instructor: Prof. Nathalie De Leon.
    - o Lab Instructor: Eric Mills, Ph.D.

- ➢ MSE 549 Micro-Nanofabrication and Thin-Film Processing
    - o Course Instructor: Prof. Stephen Chou

INTRODUCTORY COURSES (New Labmembers):

- ➢ **Microfluidic Boot Camp** – a concentrated course designed to engage researchers in microfluidics and the capabilities of the soft materials lab at Princeton. Attendees process microfluidics and participate in a mixture of tutorials, guest lectures, and hands-on experiences

- ➢ **First Fab** – A 3 - 4 day Microfabrication Training Course that introduces new labmembers to the basic technologies of nano/microfabrication and gives hands-on experience in making nano/microstructures. During this course, a staff member demonstrates all operations of the process tools and labmembers have an opportunity to handle varied pieces of cleanroom equipment including tools for lithography, etching, metal and dielectric deposition

- ➢ **PRISM Cleanroom Orientation 1** – A PRISM Cleanroom laboratory safety lecture and a tour of PRISM Cleanroom

- ➢ **Orientation 2** – A practical training inside the Cleanroom at the acid fume hood, focused on piranha etch and BOE etch.

FUNDAMENTAL PROCESSING PRINCIPLES:

- ➢ PVD (Physical Vapor Deposition taught by Kurt J.Lesker Co.)

- ➢ Plasma Etch Processes (Taught by Oxford Instruments)

- ➢ Nanolithography (taught by Raith, Inc.)

Individualized Technology Training (Short Courses):

- ADT Dicing Saw
- Questar Wedge Wire Bonder
- K&S Wedge Wire Bonder
- K&S Wedge Wire Bonder
- Logitech Lapping/Polishing Station
- Tresky Flip Chip Bonder
- RCA Hood – RCA cleaning procedure of the whole cassette of silicon wafers prior to high-temperature processing steps
- CVD Equipment 1034 Oxidation and Annealing Furnaces
- CVD Equipment 1033 Oxidation Furnace
- CVD Equipment 1033 LPCVD Furnaces
- Gaertner Ellipsometer
- Hitachi S-4700 SEM
- KLA Tencor P-15 Profilometer
- NanoSpec Reflectometer
- Nanonex Nanoimprinter
- Raith E-beam Writer
- KLA Tencor D-120 Profilometer
- PDMS Processing Tools
- Critical Point Dryer
- Cambridge ALD
- Oxford ALD
- Angstrom Covap Thermal Evaporator
- Angstrom Dielectrics Sputter System
- Angstrom Dual Chamber E-beam Evaporator
- Angstrom Metals Sputter System
- Angstrom Nexdep E-beam Evaporator
- Denton E-beam Evaporator
- Edwards Thermal Evaporator
- Ultraviolet/Ozone Cleaning System
- VWR 1410 Vacuum Oven
- CVD2 Stack Furnace
- Oxford ICP-CVD
- Oxford PlasmaPro80 RIE
- SAMCO 200iPB RIE III-V
- SAMCO 800iPB Deep RIE
- STS Multiplex ICP Etcher (Metals)
- TePla M4L Plasma Asher
- SSI Solaris 150 RTP Systems
- Heidelberg DWL66+
- Photoresist Spinners
- Poulos Chrome Etch Processor
- Suss MA6 Mask Aligner
- Suss MJB4 Mask Aligner
- YES Vacuum Oven
- PlasmaTherm AEPX SLR (Metals)
- PlasmaTherm APEX SLR (Semiconductors)
- Heidelberg microPG101
- Semi-Tool Spin Rinse Dryers

AFOSR

- *Observation of an Environmentally Insensitive Solid-State Spin Defect in Diamond*
- *Spin-Photon Interface for Rare-Earth Ions*
- *Thin Film Optoelectronic Device Applications*
- *Time Modulated Phased Arrays*
- *Top Emitting Perovskite LED*

ARO

- *3D Integration with Fluxonium*
- *Experimental Realization of An Error-Protected 0-π Superconducting Qubit*
- *Granular Aluminum Kinetic Inductors*
- *Novel Qubit Designs for Improved Coherence*
- *Superconducting Circuits for Quantum Device Applications*

CBRIC

- *Exploration of Large-Area Electronics in Wireless Communication at Microwave Frequency*

DARPA

- *High Yield TFTs Employing Compressed Sensing for Large Scale Tactile Sensing*
- *Nanophotonics for Telecom Quantum Networks Based on Neutral Silicon Vacancy Centers in Diamond*
- *Spin-Photon Interface for Rare-Earth Ions*

DoD

- *Quantum Simulation with Superconducting Circuits*

DOE

- *Electronic Devices Using Topological Materials*
- *Fabrication of Devices for Transport Experiments of Topological Materials*
- *Measurement of Surface Incident Ion Direction Using Engineered Targets on DiMES at DIII-D*
- *Plasma Parameters Via Fine-Structure X-Ray Spectroscopy in Short-Pulse Heated Tracer Layer Targets*
- *Probing Correlated Superconductors and Their Phase Transitions on the Nanometer Scale*
- *Probing Exotic Phases of Interacting Electrons in Low-Dimensional Systems*
- *Study of the Ballistic Motion of High-Quality Electrons in Low Dimensions*
- *Visualizing Unconventional Superconductivity in Twisted Bilayer Graphene*

DTRA

- *Ultrasensitive Nanostructured Biosensor*

Eric and Wendy Schmidt Transformative Technology Fund

- *Development of Laser Additive Manufacturing for Metal Production with In Situ Defect Control and Quality Assurance*
- *New Materials for Quantum Systems*
- *Supertank Facility*

Exxon

- *2D Lab*

Gordon and Betty Moore Foundation

- ➢ *Cavity Coupling of Molecular Systems*
- ➢ *Electron Transfer Through Entrained DNA Strands*
- ➢ *Exotic Phases of Electrons in Interacting 2D Systems*

Government SBIR (Small Business Technology Transfer Grant)

- ➢ *Reliable and Efficient of UV-Absorbing Hexabenzocoronene Derivative Organic Solar Cells*

Industrial

- ➢ *Lateral Tailoring of Gain and Current Profile in High Power Edge Emitting Lasers*
- ➢ *Photonic Integrated Circuits for Neuromorphic and Microwave Processing*
- ➢ *Quantum Optimal Control*
- ➢ *Wetting and Microfluidics*

James C. Sturm Unrestricted Fund

- ➢ *3D Neural Probe*
- ➢ *Cancer Cell Dynamics on a Complex Drug Landscape*
- ➢ *High-Yield Fabrication of Thin Film Transistors*

Jet Propulsion Laboratory (California Institute of Technology)

- ➢ *Subscale Starshade Testing*

Lawrence Livermore National Library

- ➢ *High-Resolution X-Ray Spectroscopy Studies of Ion and Electron Temperature Profiles in Buried Layer Targets*

MRSEC

- ➢ *Probing Exotic Phases of Interacting Electrons in Low-Dimensional Systems*
- ➢ *Study of the Ballistic Motion of High-Quality Electrons in Low Dimensions*

MURI

- ➢ *An Ingestible Sensor to Monitor Gut Microbiome*
- ➢ *THz Coupled Oscillator Arrays*
- ➢ *Time Modulated Phased Arrays*
- ➢ *Superconductivity of Weyl Semimetals and Applications*

NASA

- ➢ *Subscale Starshade Testing*

NIH

- ➢ *C. Elegans in PDMS Chip*

NIH/GPG STTR

- ➢ *Microfluidic*

NSF

- A Holographic Lab-On-A-Chip System for the Long-Term Study of the Interplay Among Hydrodynamics, Surface Chemistry, and Microbiology
- Active Metamaterial with a Quantum Cascade Structure
- Biopolymer Fouling of Water-Filtration Membranes
- CO_2 Driven Diffusiophoresis and Particle Separation
- Electrons on Helium
- Electron Solids in AlAs Two-Dimensional Electron System
- Engineered Batteries for Energy Harvesting
- Fiber Formation Based on Aqueous Two Phase Systems
- Flow Induced Gelation of Microfiber Suspension
- Large-Area Thin Film Transistors for Sensing Applications
- Limit Cycles and Chaos in Coupled Driven Nonlinear Superconducting Circuits
- Magnetic Particle Sensing Based on CMOS Oscillator Array
- Many Body Quantum Simulation Using Superconducting Circuits
- Microwave Striplines for Diamond
- Multiple Ion Diffusiophoresis
- Nanoscale Temperature Anemometry Probe Fabrication
- Nanoscale Thermal Anemometry Probes
- Neuromorphic Photonics
- Observation of an Environmentally Insensitive Solid-State Spin Defect in Diamond
- Optical Biosensor
- Origins of Diamond Surface Noise Probed by Correlating Single Spin Measurements with Surface Spectroscopy
- Polymer Thin Film Crystallization
- Quantum Simulation with Superconducting Circuits
- SiPM Packaging for Darkside-20K
- Si/SiGe 2DEGs Grown by UHVCVD for Quantum Computing Applications
- Spin-Photon Interface for Rare-Earth Ions
- STRR Phase I: Development of a Transparent, Near-Ultraviolet Photovoltaic Power Source for Wireless Operation of Smart Windows and IoT Devices
- Study of Ballistic Motion of High-Quality Electrons in Low Dimensions
- Supertank Facility
- Surface Loss Mitigation for Superconducting Qubits
- Ultrasensitive Nanostructured Biosensor

NSF-DMR

- Probing Exotic Phases of Interacting Electrons in Low-Dimensional Systems

NSF-GFRP

- II-VI, III-V Semiconductor Intersubband Devices

PCCM

- Observation of an Environmentally Insensitive Solid-State Spin Defect in Diamond

PEI

- Soil on a Chip

PPST

- *High-Performance Thin Film Transistors for Large Area Circuits and Systems Applications*
- *High-Yield TFTs Employing Compressed Sensing for Large-Scale Tactile Sensing*

Princeton Catalysis Initiative

- *Engineering Spindle Assembly in Droplet Microfluidics*
- *Engineering the Chromosome Segregation Machinery to Catalyze Life*
- *Self-Organization of Microtubules in Cell-Sized Droplets*

Princeton ELE Department

- *The Use of Elastic Filament Velocimetry (EFV) in Measuring Viscosity of a Passing Fluid*
- *ZnO Thin Film Technology on Flexible Substrates*

Princeton IP Accelerator Fund

- *High Sensitive Elastic Filament Velocimetry Probe*

Princeton Physics New Faculty Startup

- *Topological Quantum Phases in 2D Materials (Jia)*
- *Topological Quantum Phases in 2D Materials (Onyszczak)*
- *Quantum Devices Based on 2D Materials (Wang)*
- *Quantum Devices Based on 2D Materials (Yu)*

Princeton School of Engineering and Applied Science (SEAS)
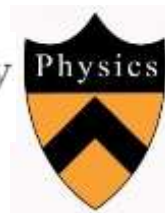
- *Visiting Research Scholar*

Princeton University

- *Quartz Wetting by Water and CO_2, and the Potential Impact of Organic Residues*

Princeton University-Yan Lab

- *High Yield Monolayer Graphene Grids for Cryo-EM*

Simons Foundation

- *Graphene Single Electron Transistor for Neutrino Detector*
- *Simons Observatory (Bruno)*
- *Simons Observatory (Li)*
- *Simons Observatory (Macakova)*

SRC

- *High-Yield TFTs Employing Compressed Sensing for Large-Scale Tactile Sensing*

Roman Akhmechet
Examining effect of focus offset on photoresist profile
The Princeton Institute for the Science and Technology of Materials (PRISM)

In order to obtain straight sidewalls in etched materials, it is important to understand the starting sidewall profile of photoresist mask. To that end, a focus study was done on DWL66+ direct writer to understand how focus offset setting affects photoresist profile. For this test, 540nm thick AZ1505 resist was used. Using standard intensity and filter settings, the test wafers were exposed with 2mm lens in optical focus mode. Cross sections were obtained on Hitachi SEM. The tested features were long 5 micron lines with 5 micron space. The resulting profiles may be different for smaller dimensions. It is also important to notice a persistent scum layer right at the foot of the resist feature.
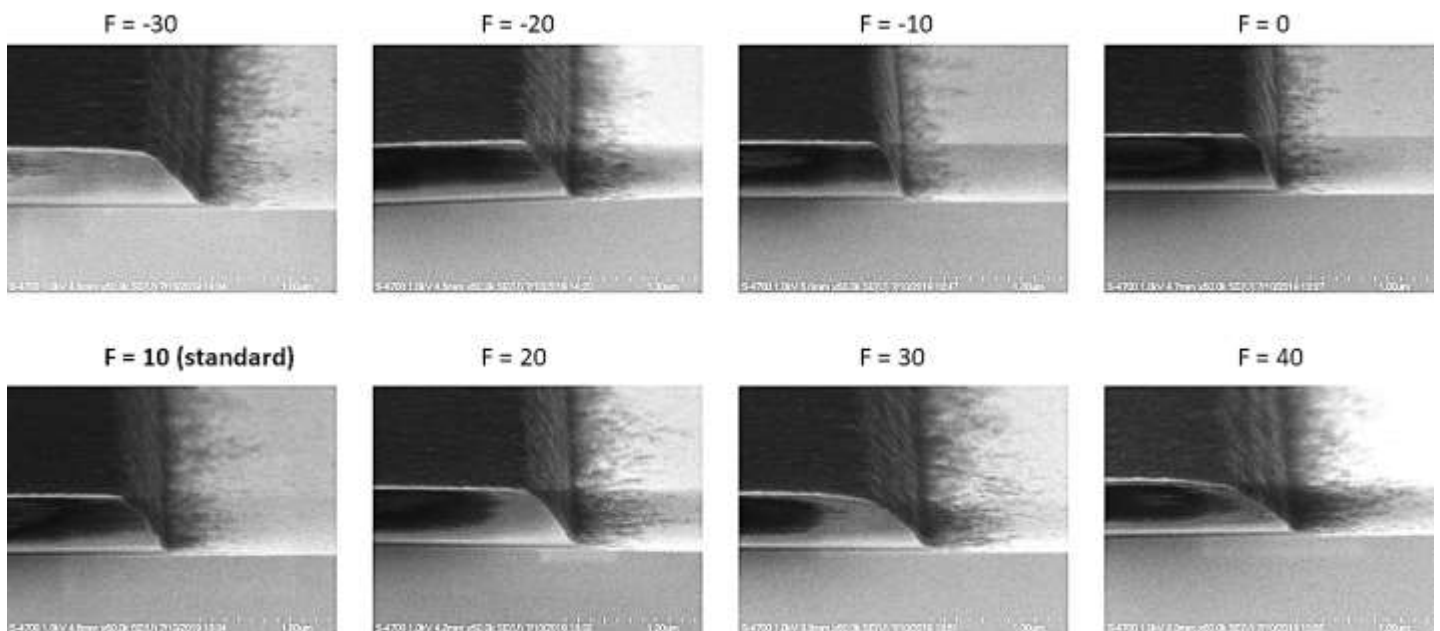
Figure 1: AZ1505 profile at different focus settings. Intensity = 35%. Filters 5%+50%.

Roman Akhmechet
Using optical emission spectroscopy to monitor etch chambers
The Princeton Institute for the Science and Technology of Materials (PRISM)

In plasma etching, the condition of the etch chamber is one of the critical factors that determine the quality of the final etch. Dirty or improperly conditioned chambers will result in uncontrollable etch rates and profiles, and can lead to rough etched surfaces from micromasking. Recently, we have started to use OceanOptics' FLAME USB spectrometer together with OceanView software to baseline chamber spectrums after wet cleans. Comparing the current spectra to baseline will give the labmembers an indication of cleanliness of the tool before committing a critical device or sample. To demonstrate the technique, we have intentionally contaminated the chamber with high flow rate of CHF_3 gas that leaves CF_x residue on the sidewalls. The figure below shows spectra at the start and end of the clean recipe, as well as baseline clean chamber. While peaks associated with CF_x residue show up at the start, they disappear by the end of the clean, which now overlaps with baseline spectrum. This means that the chamber has been returned to the original clean state.
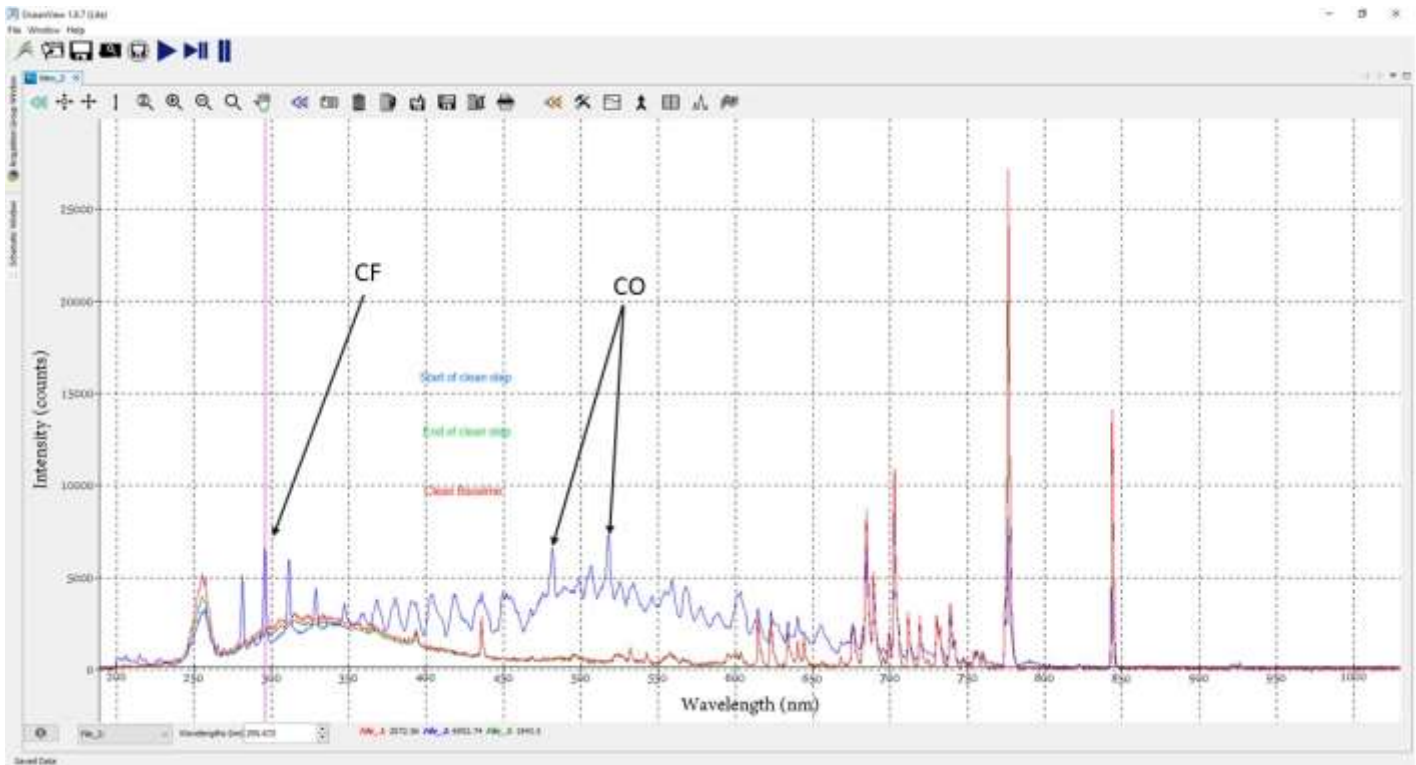
Figure 1: Overlay of spectra at the start and end of clean recipe. The spectrum for end of clean is overlapping with baseline.

Zuzanna Lewicka
The Princeton Institute for the Science and Technology of Materials (PRISM)

In this paper, the focus was on the ability to deposit high quality silicon dioxide (SiO_2) films using the Oxford PlasmaPro 100 Inductively-Coupled Plasma Chemical Vapor Deposition (ICP-CVD) system located in the PRISM Cleanroom by the reaction between 4% silane in argon (4% SiH_4/Ar) and oxygen (O_2). Process parameters discussed include film refractive index (R.I.), thickness non-uniformity and wet etch rates in buffered oxide etch solution (BOE 10:1).

The refractive index provide important information on the stoichiometry of the deposition silicon dioxide films and R.I. of 1.46-1.47 as well as low thickness non-uniformity are desirable. The responses shown in Figure 1 indicated that SiO_2 film with R.I. of about 1.465 could be obtained with O_2/SiH_4 ratio = 3.5 - 6 for ICP power 1000 - 2000 W. However, as indicated in Figure 2, lower film thickness non-uniformity (<3%) across the wafer

was observed for lower ICP power of 1000 - 1300 W. Furthermore, the results of the SiO_2 wet-etch rate in BOE solution (see Figure 3) indicated that films deposited with ICP power=1000 – 1300 W and O_2/SiH_4 = 3.75 characterized good quality and etch rate of 22 Å/sec that compared favorably to value of about 8 Å/sec for thermally-grown SiO_2.

This paper has shown that high quality silicon dioxide (SiO_2) films can be deposited in the PRISM Cleanroom using the Oxford PlasmaPro 100 Inductively-Coupled Plasm Chemical Vapor Deposition system. The optimized ICP-CVD SiO_2 process, with the following parameters: process temperature: 250°C, ICP power = 1300 W, O_2/SiH_4 = 3.75 (4% SiH_4/Ar = 100 sccm, O_2=15sccm), chamber pressure 8 mTorr, was stable and reproducible (see Figure 4).
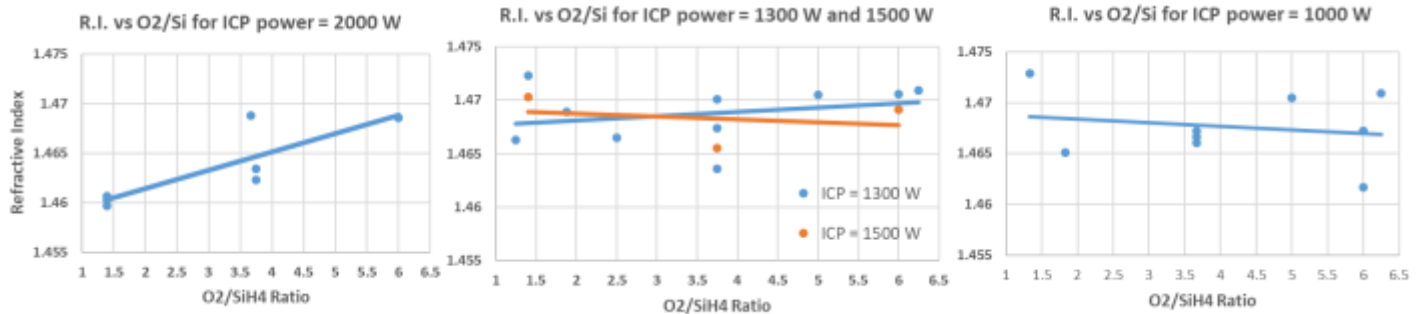
Figure 1: The effects of O_2/SiH_4 gas ratio and ICP power on the SiO_2 refractive index. All the films were deposited on 4 inch Si wafers with the typical thickness of 1000 to 2000 Å, process temperature 250°, and chamber pressure set to 8 mTorr.
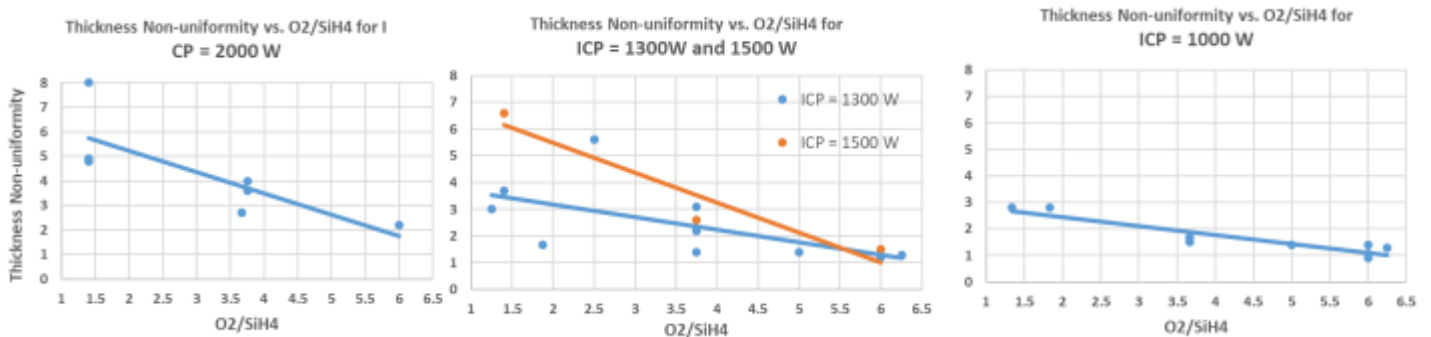
Figure 2: The effects of O_2/SiH_4 gas ratio and ICP power on the SiO_2 film thickness non-uniformity.
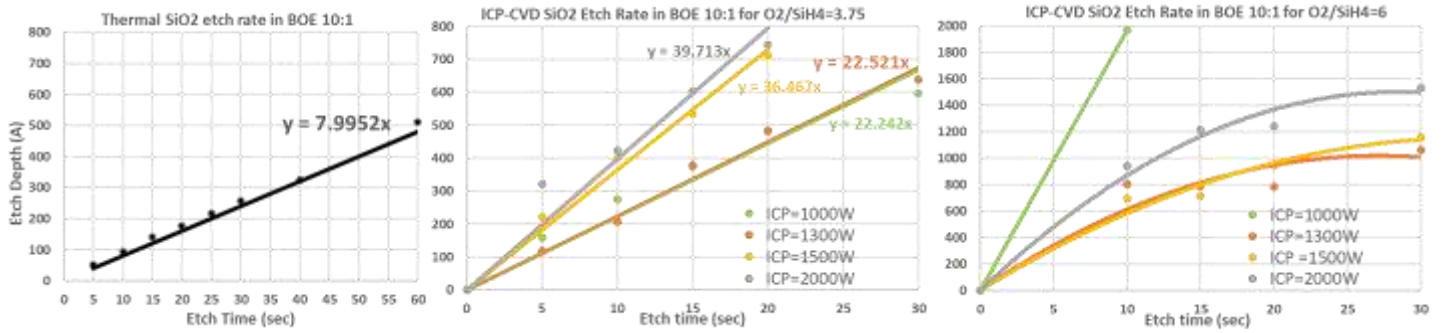
Figure 3: Etch rate in BOE solution for thermal (Left) and ICP-CVD (Center and Right) SiO2.
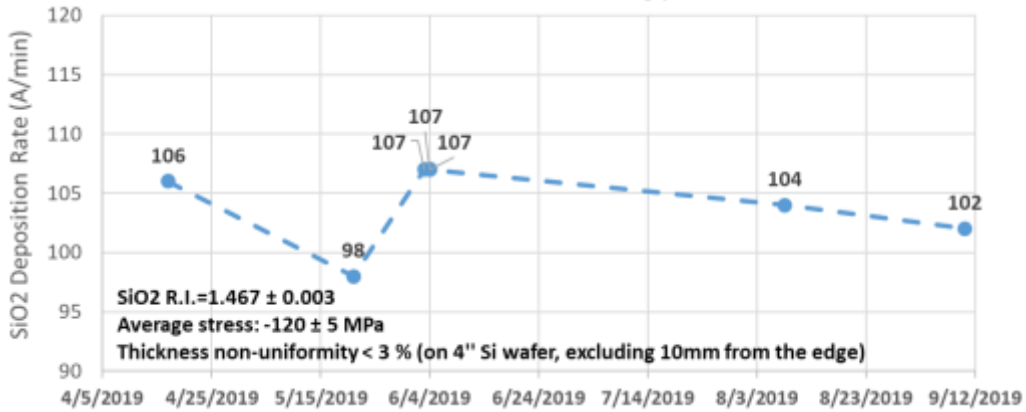
Figure 4: Wafer to wafer SiO2 deposition rate repeatability.

Acknowledgement: I would like to thank and recognize Paul DiPippo and Benjamin Harrop for helping with the collection of data.
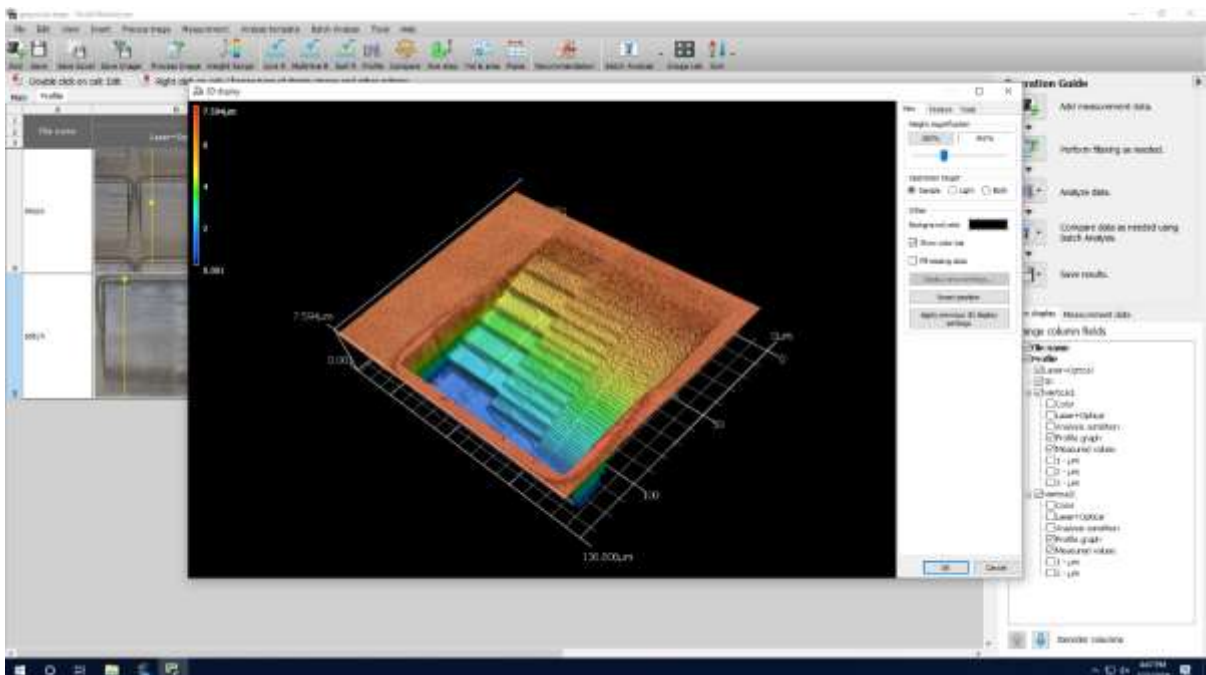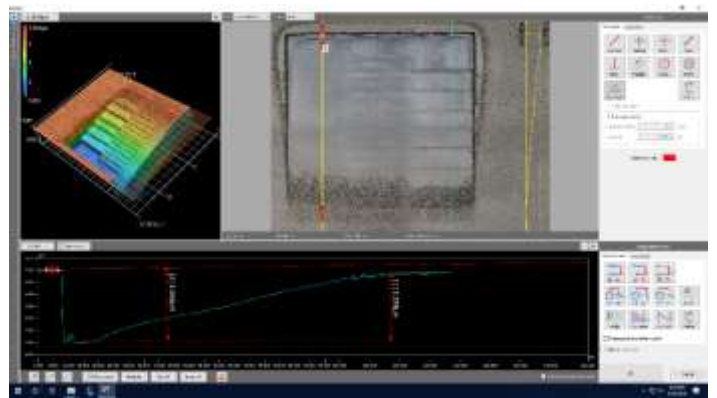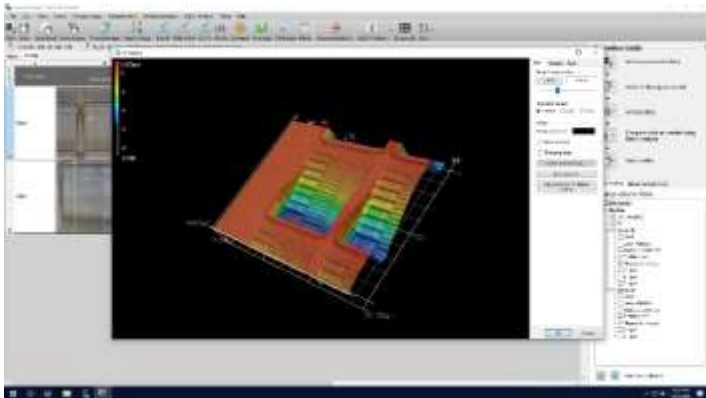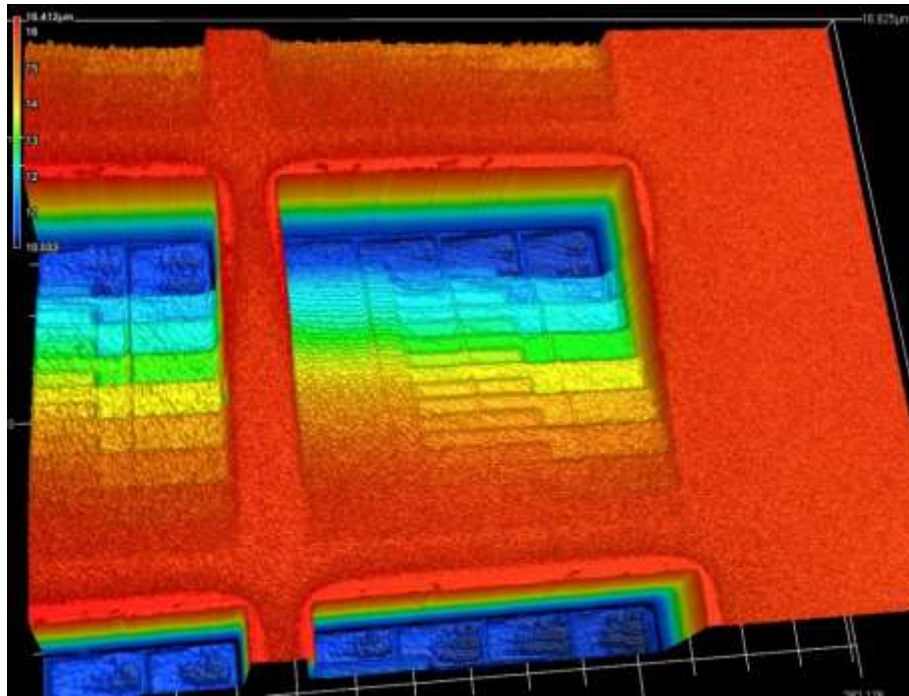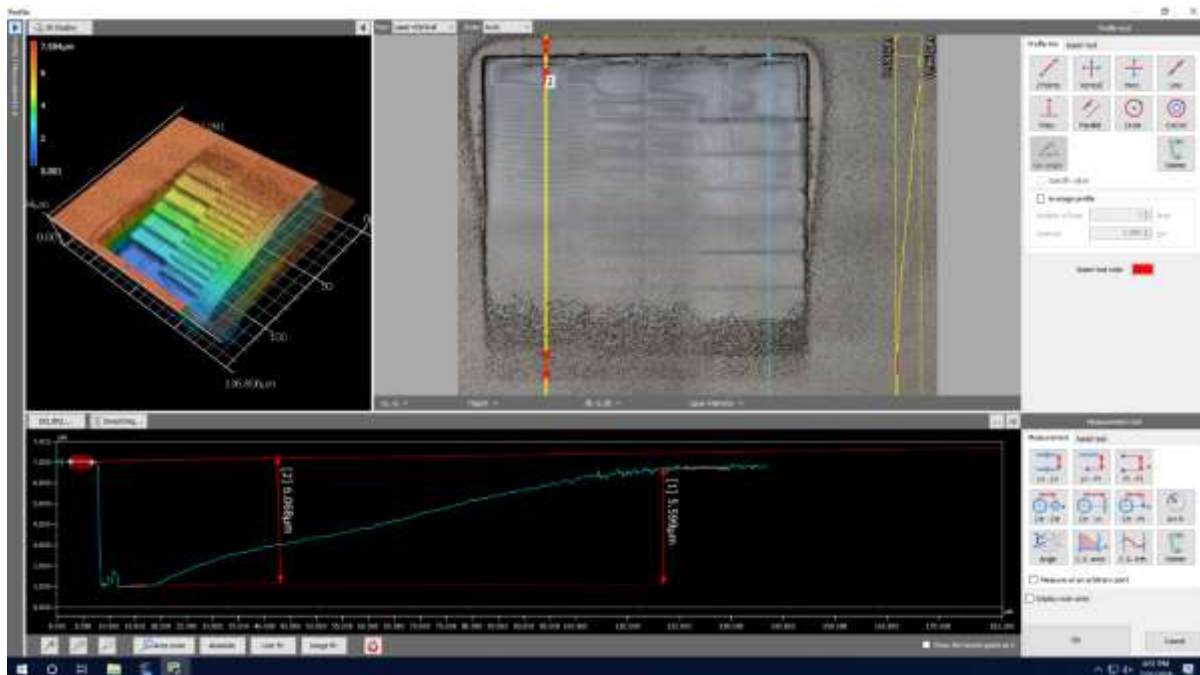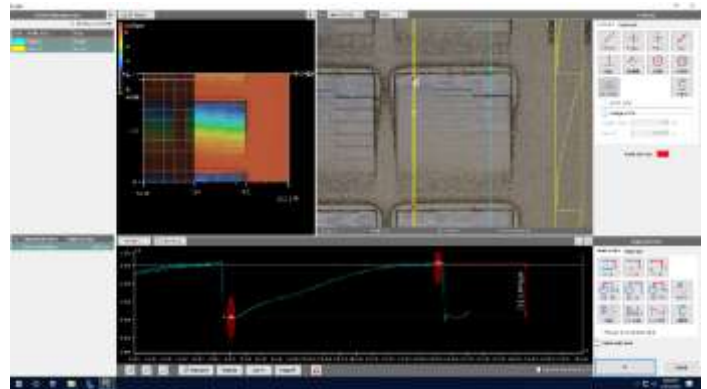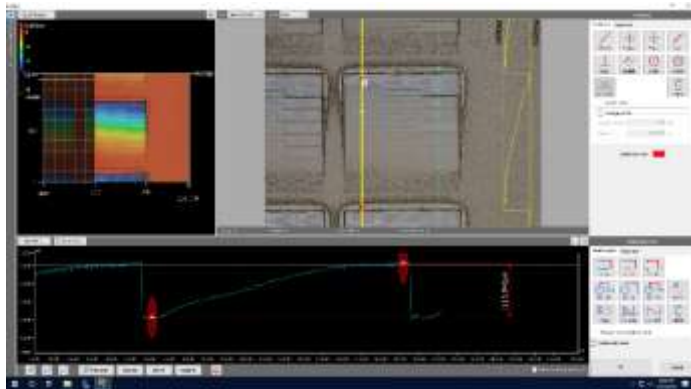
Researcher: **Shota Abe and Charles H. Skinner**
Advisor: **Bruce E. Koel (CBE)**
Sponsorship: **DOE**

The ion trajectory near plasma facing surfaces is strongly influenced by the magnetic pre-sheath [1]. The plasma physics in the pre-sheath region is crucial for understanding of plasma-material interactions such as erosion, deposition, and migration in fusion devices. However, there is a very limited number of experimental studies reported on the ion angle of incidence to the surface [2]. By using PRISM facilities, specially designed 100-nm coatings of aluminum and micron trenches were fabricated on 6-mm diameter silicon disks. When the ion incidence elevation angle is shallow enough, the trench geometry can shadow deposited material from further erosion by micron-scale surface irregularities [3]. Then, measurement of the shadow geometry will reveal the incident ion angle distributions (IADs), both in azimuth and elevation.

Roman Akhmechet (PRISM) performed mask coating on the samples using the Heidelberg DWL66+ direct write lithography system to produce the aluminum deposition pattern (Figure 1). Aluminum was deposited by the Angstrom Nexdep E-beam Evaporator. By using the Helios NanoLab G3 UC DualBeam Focused Ion Beam

(FIB) system, Yao-Wen Yeh (Rutgers University, formerly PRISM) fabricated $30 \times 30 \times 2$-µm or $30 \times 30 \times 3$-µm deep trenches (Figure 2 (a)) on silicon surfaces. Each trench has two sloping sides preventing ions reflecting back onto the trench floor. The 3D geometries of the trenches were confirmed using the Bruker Dimension ICON3 Atomic Force Microscope (AFM).

These engineered sample surfaces were exposed to L-mode deuterium discharges in the DIII-D tokamak plasma device (General Atomics, San Diego) via the Divertor Material Evaluation System (DiMES) sample exposure facility. The sample alignment with the magnetic field B_t line is shown in Figure 1. Scanning electron microscopy (SEM) (Figure 2 (b)) and Energy-dispersive X-ray spectroscopy (EDS) images obtained by using the Verios 460 Extreme High-Resolution SEM show changes on the trench floor and the material deposition pattern affected by the influence of shadowing. These patterns are analyzed with a theoretical model to give IADs for this discharge condition [1].
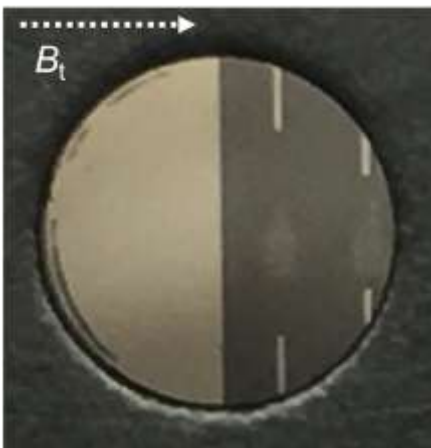
Figure 1: Microscope image of a fabricated sample. The left half of the sample was covered by aluminum. Micro trenches (not visible in this picture) and thin fiducial lines of Al were fabricated on the right half.
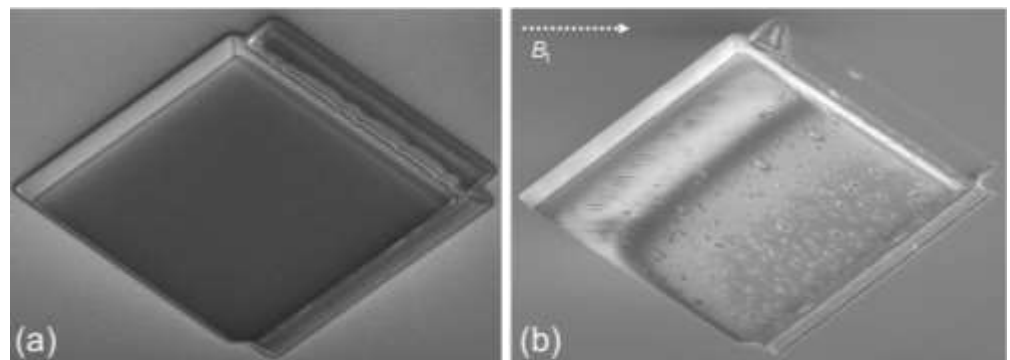
Figure 2: SEM images of an engineered trench (a) before and (b) after plasma exposures. The viewing angle is tilted for 45° from the surface normal. In figure (b), the deposited material pattern can be seen as the bright area on the top left inside the trench.

CITATIONS

➢ [1] C.P. Chrobak. et al., Nucl. Fusion 58 (2018) 106019.
➢ [2] J. Coburn, et al., Nucl. Mater. Energy 18 (2019) 316.
➢ [3] C.H. Skinner, et al., Nucl. Mater. Energy 18 (2019) 35.

Researcher: **Quinn Burlingame**
Advisor: **Lynn Loo (CBE)**
Sponsorship: **Government SBIR (Small Business Technology Transfer Grant)**

The primary aim of this project is to develop robust semi-transparent ultraviolet (UV)-absorbing organic photovoltaic (OPV) cells for integration into power generating windows, by determining their primary photochemical and morphological degradation modes and applying these insights to generate stable new chemicals and device architectures. We assert that a commercially viable semi-transparent OPV must be: (1) efficient capable of providing sufficient electrical power for the intended application (i.e., driving internet-of-things sensors, electrochromic devices, or charging batteries), (2) reliable able to maintain its performance for decades, comparable to other commercialized photovoltaic (PV) technologies and conventional building materials, and (3) semi-transparent and color neutral nearly imperceptible, such that the presence of an OPV in a window does not diminish its aesthetic appeal or functionality.
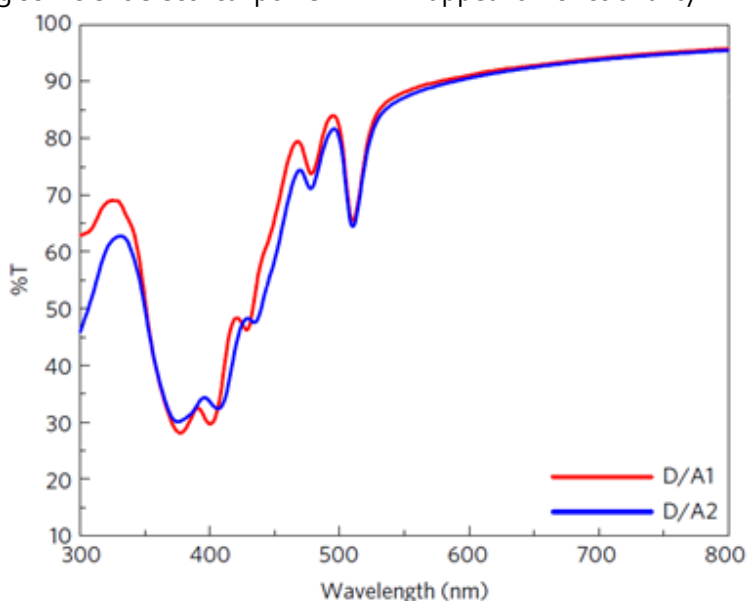
Figure 1: Optical transmission of semi-transparent UV-absorbing organic photovoltaics using the materials synthesized as part of this project.
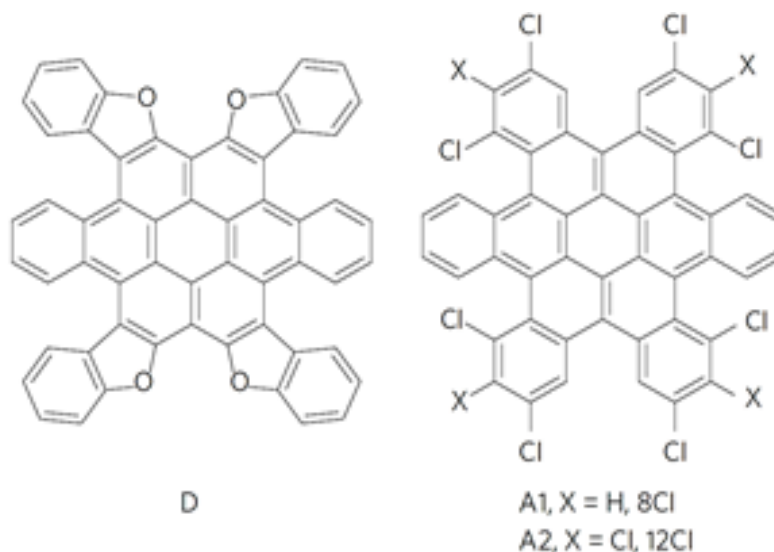
Figure 2: UV-absorbing photovoltaic materials used in the project.

CITATIONS

- None yet

Researcher: **Nick Davy** in collaboration with **Quinn Burlingame**
Research Fellow
Sponsorship: **NSF-STTR**

Transparent, near-ultraviolet photovoltaic cells could catalyze the growth of US companies developing smart window and internet-of-things technologies, boosting the energy efficiency of buildings and increasing occupant connectivity, resulting in widespread energy savings, carbon emission reductions, and quality-of-life enhancement. Postdoctoral researcher Quinn Burlingame from Professor Lynn Loo's Organic and Polymer Electronics Laboratory collaborated with PRISM member company Andluca Technologies led by research fellow Nick Davy to explore novel transparent electrodes for organic solar cells uniquely designed to harvest near-ultraviolet light. The researchers utilized material deposition and characterization equipment in the MNFL to solve key challenges on the path from laboratory to real-world manufacturing.
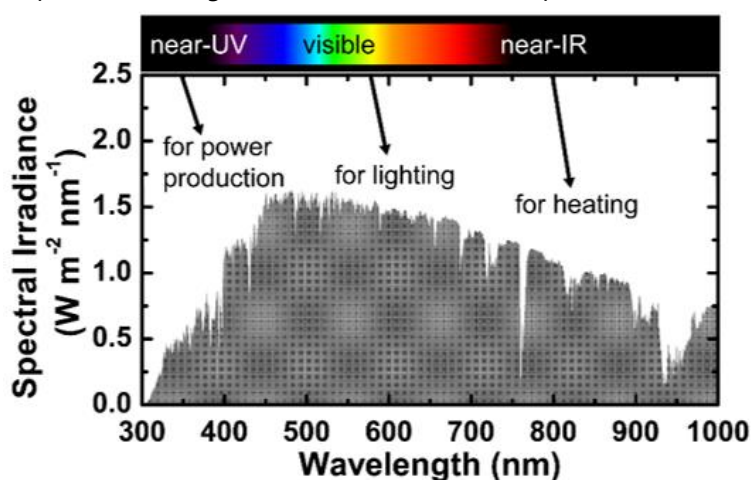
Figure 1: The solar spectrum (gray) with a color legend that provides reference for light as detected by the human eye.
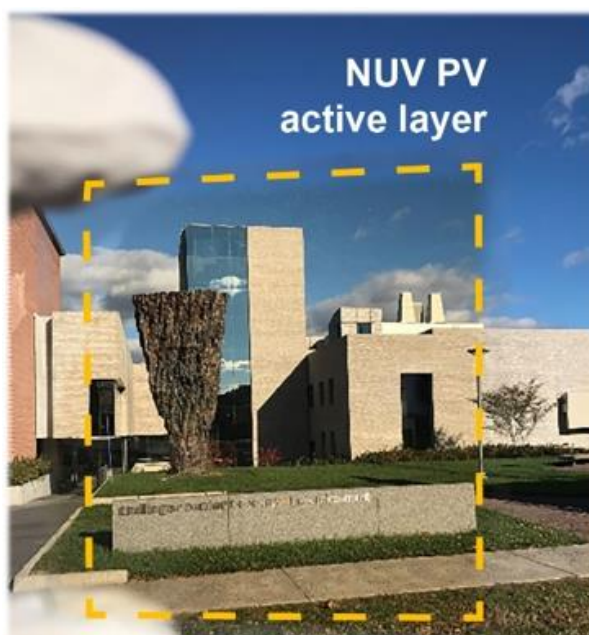
Figure 2: Photograph of near-ultraviolet organic solar cell active layer on glass.

CITATIONS

➢ Davy, N.C., Y.-L. Loo, *et al. Nature Energy* **2017**, 2, 17104.
➢ Quinn C. Burlingame, *et al. Manuscript in preparation.*

Researcher: **Avery Agles**
Advisor: **Ian C. Bourg (CEE)**
Sponsorship: **NSF**

It has recently been shown that a critical step in the biofouling of water treatment membranes occurs in the feed water *prior* to contact with the membrane surface when biopolymers referred to as extracellular polymeric substances (EPS) form aggregates known as transparent exopolymer particles (TEP) (Bar-Zeev *et al.*, 2012). The polymer networks comprising TEP are sticky and mechanically stable, which makes them suitable for microbial colonization, yet also makes them problematic for the water treatment industry. These aggregates initiate biofilm growth at much faster rates than planktonic microbes. This investigation aims to use molecular dynamics (MD) simulations and microfluidic experiments to provide researchers and water treatment engineers alike with a proper understanding of the molecular basis for the aggregation of biopolymers into TEP. In particular, we would like to design a microfluidic experiment to investigate how the hydrodynamic and ionic environments seen in water treatment facilities influence the microstructural properties of TEP that might inform its role in biofouling.
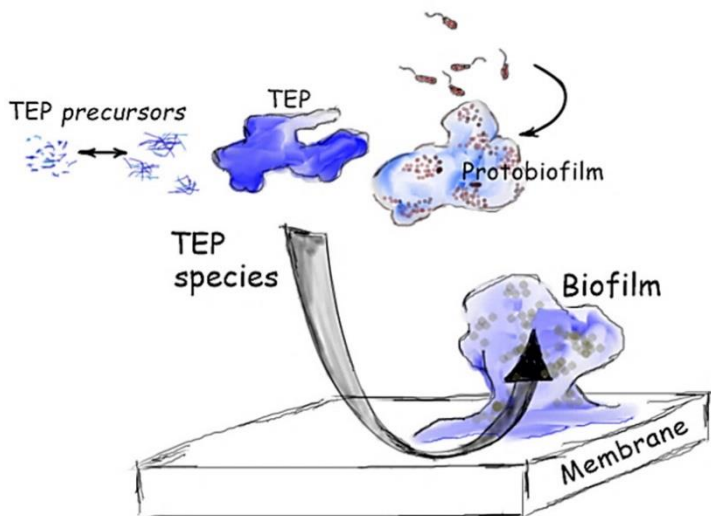
Figure 1: Current Paradigm of Biofouling of Water Treatment Membranes.
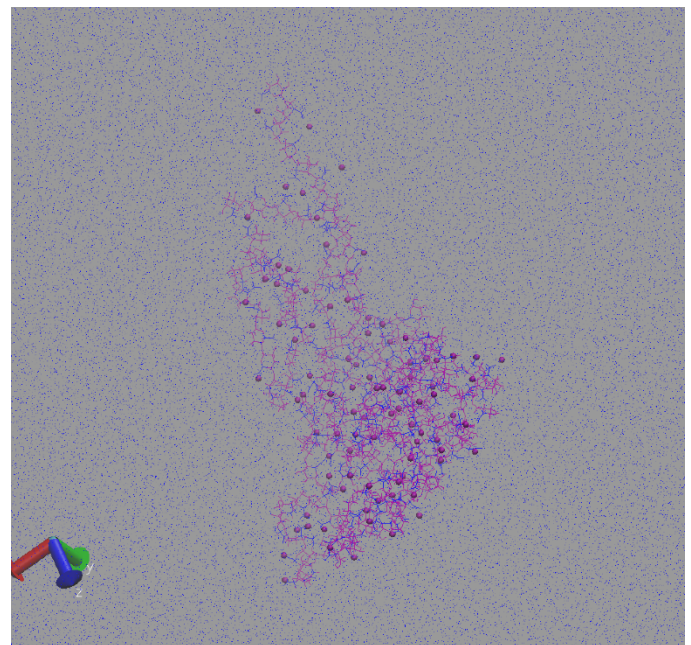
Figure 2: MD Simulation of precursor particle to TEP.

CITATIONS

➢ Bar-Zeev, E., Berman-Frank, I., Girshevitz, O. & Berman, T. *Proc. Natl. Acad. Sci.* **109**, 9119–9124 (2012).

Researcher: **Emily Wei-Hsin Sun**
Advisor: **Ian C. Bourg (CEE)**
Sponsorship: **Princeton University**

Fundamental physical and chemical features governing multiphase flow in water-CO2-quartz nanopore systems directly impact the mobility and trapping of supercritical CO2 injected into the subsurface as part of Carbon Capture and Sequestration (CCS). CCS is a potentially important approach to mitigating anthropogenic emissions, and depends largely on the capillary trapping capacities of subsurface formations. However, published experimental data on relevant properties, such as water-CO2 contact angles (CA), vary widely. The fundamental basis of this variability remains poorly known, though surface contamination and/or roughness is hypothesized to be a significant source. An important remaining knowledge gap in CCS is the influence of organic residues naturally present in sedimentary rocks on water-CO2-solid wetting and multiphase flow. We carry out a series of MD simulations to probe CAs in the presence of organic molecules. Using small organic molecules as proxies, we simulate a CO2 bubble in a water-filled 6.6 nm quartz nanopore with varying fluid pressures. We find that high concentrations of organics may influence the water-CO2 wetting behavior of quartz. We hope to supplement our MD findings with observations from microfluidic experiments.
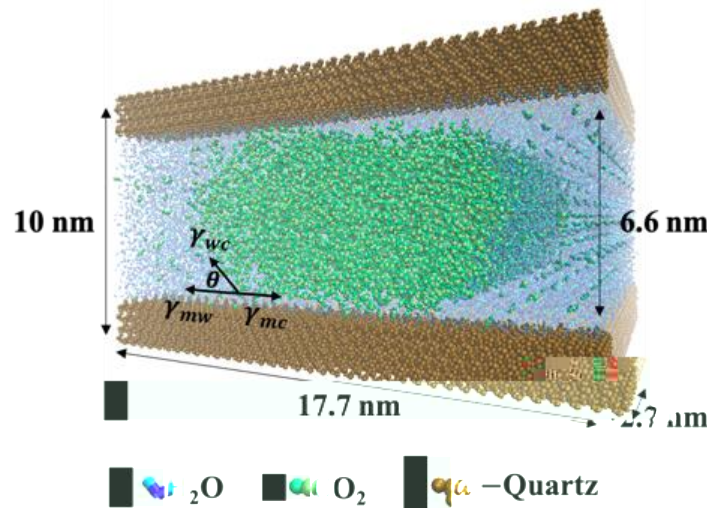
Figure 1: A snapshot of the MD simulation cell showing a CO₂ bubble in a water-filled quartz nanopore.
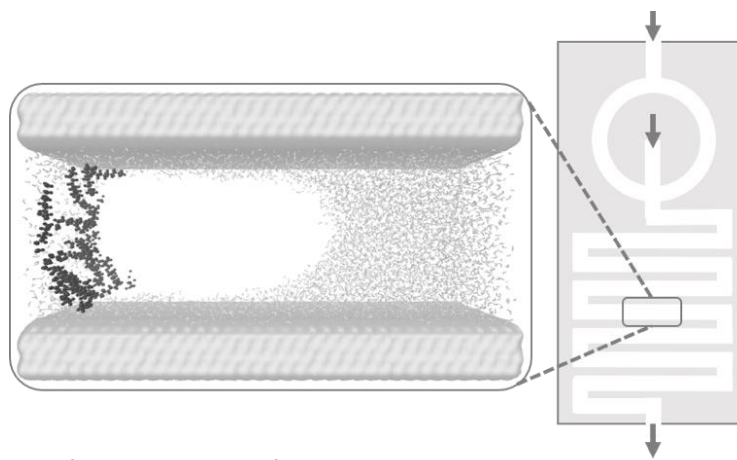
Figure 2: On the left is a snapshot of an MD simulation of water, air, and organic molecules in a mica nanopore, with force added in one direction to induce flow. On the right is a diagram of an idea for microfluidic experiments to probe the simulated multiphase flow phenomena at a micro-scale.

CITATIONS

➢ In Preparation: Sun, E. W.-H., Bourg, I. C. (2020).

Researcher: **Courtney DelPo**
Advisor: **Gregory D. Scholes (CHM)**
Sponsorship: **Gordon and Betty Moore Foundation**

A well-established place in scientific history exists for synthetic energetic modification, but cavity coupling is proving to be an effective and novel way to change the energy landscape of a molecular system. This project seeks to create a Fabry Perot cavity with a 4CzIPN host to modify the electronic properties of this molecular system. The thickness of the cavity will be designed to be resonant with the first singlet transition of 4CzIPN in an effort to split the singlet state into two polaritonic states with the lower polaritonic state moving below the energy level of the triplet state. This inversion of the spin states is the objective of this project, and will be detected using broadband pump-probe spectroscopy.
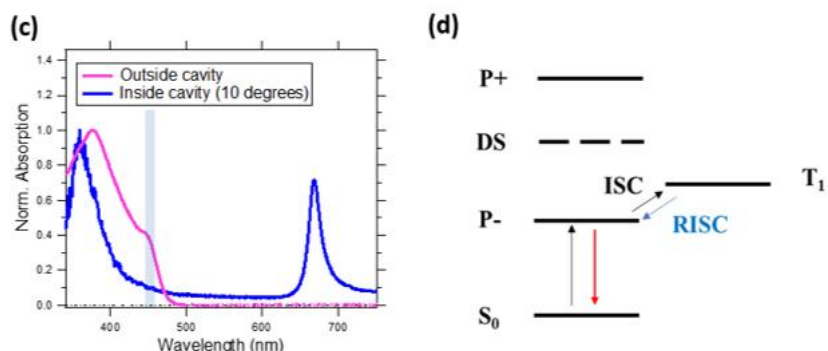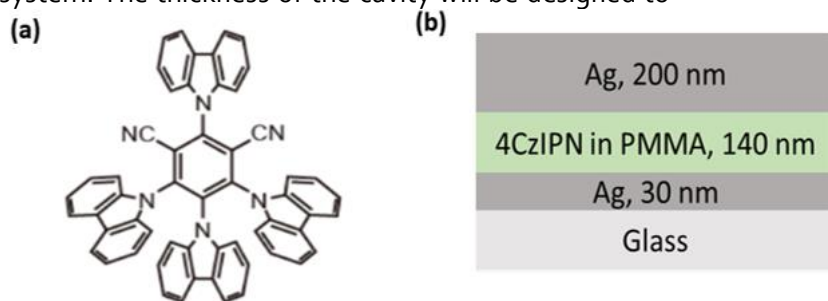
Figure 1: Cavity description. **(a)** 4CzIPN structure. **(b)** Cavity architecture. **(c)** Absorption spectrum inside and outside of the cavity coupled to 450 nm transition (highlighted in blue). **(d)** Energy level scheme inside the cavity.
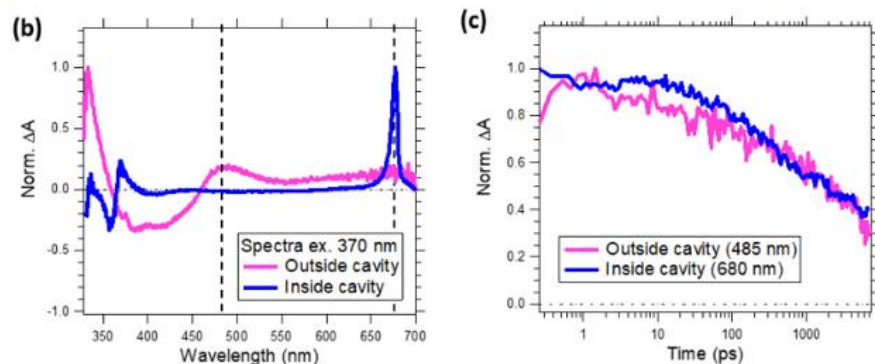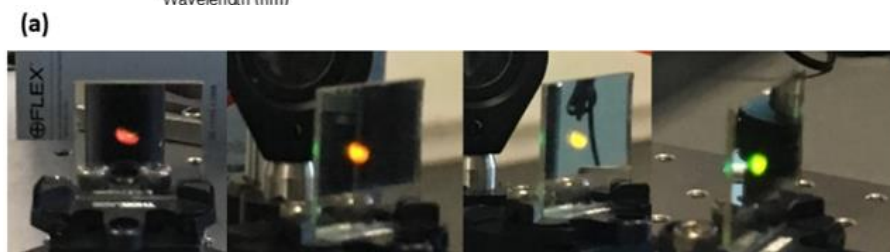
Figure 2: Experimental characterization. **(a)** Angle-dependent fluorescence. **(b), (c)** Transient absorption spectrum and selected kinetic traces inside and outside of the cavity.

CITATIONS

➢ None available at this time

Researcher: **Kyu Hyung Park**
Advisor: **Gregory D. Scholes (CHM)**
Sponsorship: **Gordon and Betty Moore Foundation**

While DNA has proven to be an efficient molecular wire capable of transporting charge up to a few tens of nanometers, their working principle is unintuitive. Unlike conjugated molecular wires, charge transport in DNA is accelerated with increasing temperature, which indicates that the process is facilitated by conformational fluctuation, a set of unelucidated vibrational motions. To study the role of molecular vibrations in charge transport, we take advantage of strong coupling between the cavity photon mode and the molecular vibration. Gold coated mirrors assembled into a solution containing cavity creates multiple photon modes, where one resonant to vibration transition of interest couples and alters the states. We aim to develop new experimental approaches to (a) address the cause and effect of vibrations on excited-state dynamics and (b) discover how cavity quantum electrodynamics can be used to change biological functions.
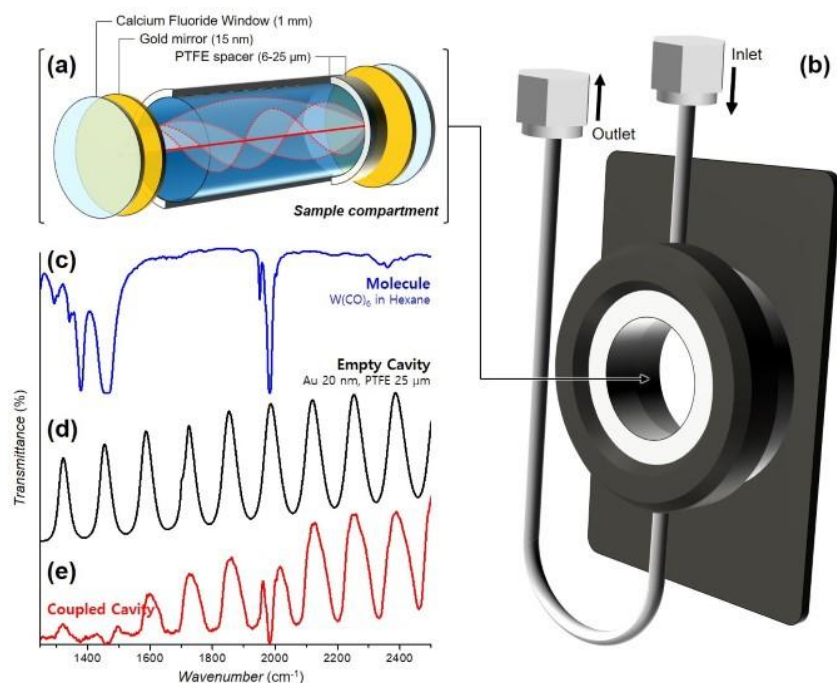
Figure 1: (a) Structure of the vibrational strong coupling cavity and (b) the flow cell. Example transmission spectra of (c) the molecule, (d) the empty cavity, and (e) the cavity coupled to the molecule.
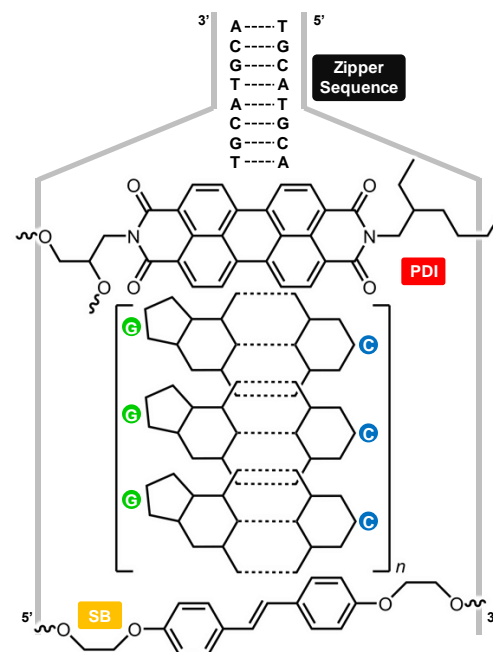
Figure 2: Schematic molecular structure of the DNA charge transporting system.

CITATIONS

➤ Zhang, Y.; Liu, C.; Balaeff, A.; Skourtis, S. S.; Beratan, D. N. Biological charge transfer via flickering resonance. *Proc. Natl Acad. Sci. USA* **2014**, 111, 10049-10054.
➤ George, J.; Shalabney, A.; Hutchinson, J.A.; Genet, C.; Ebbesen T. W. Liquid-phase vibrational strong coupling. *J. Phys. Chem. Lett.* **2015**, 6, 1027-1031.

Researcher: **Faheng Zang and Zhijuan Su**
Advisor: **Stephen Y. Chou (ELE)**
Sponsorship: **DTRA, NSF**

3D plasmonic nanoantenna sensor disk-coupled dots-on-pillar antenna array (D2PA) is developed as an on-chip bioassay platform for ultra-sensitive detection of biological antigens. The nanoantenna created from nanoimprint lithography and thin-film processes is tuned to exhibit extraordinary fluorescence signal enhancement in immunoassay, demonstrating over 10,000-fold fluorescence intensity enhancement compared to conventional glass substrate.
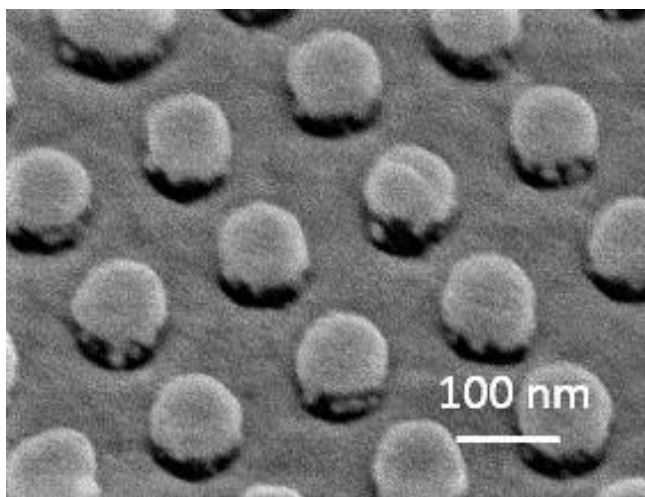
Figure 1: Scanning electron microscopy image of 3D nanoantenna biosensor enabled by nanoimprint lithography.
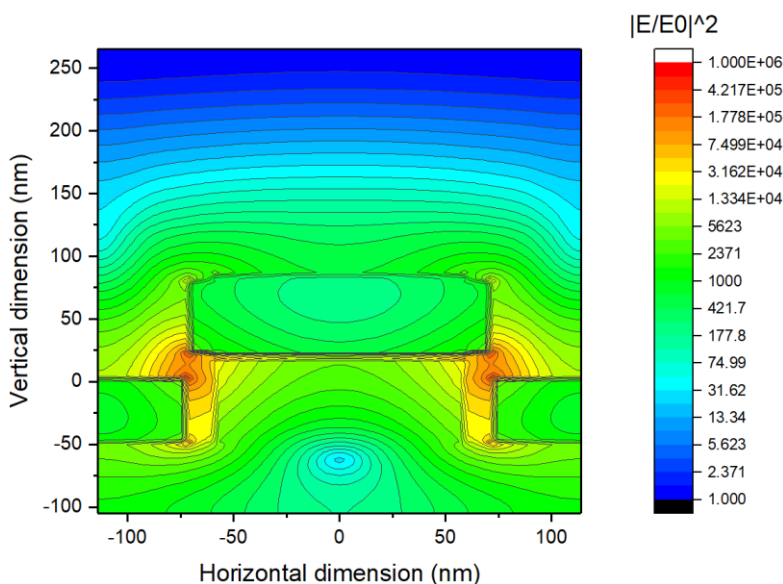
Figure 2: Simulation of electric field enhancement from nanoantenna.

CITATIONS

➤ L. Zhou, F. Ding, H. Chen, W. Ding, W. Zhang, and S. Y. Chou, "Enhancement of Immunoassay's Fluorescence and Detection Sensitivity Using Three-Dimensional Plasmonic Nano-Antenna-Dots Array," Anal. Chem. 84, 4489 4495 (2012).

➤ Zang, F., Su, Z., Zhou, L., Konduru, K., Kaplan, G. and Chou, S.Y., 2019. Ultrasensitive Ebola Virus Antigen Sensing via 3D Nanoantenna Arrays. Advanced Materials, p.1902331.

Researchers: **Alex Abulnaga, Aditya Cowsik, and Sacha Welinski**
Advisor: **Nathalie P. de Leon (ELE)**
Sponsorship: **NSF, PCCM, Air Force Office of Scientific Research**

Engineering coherent systems is a central goal of quantum science. Color centers in diamond are a promising approach, with the potential to combine the coherence of atoms with the scalability of a solid-state platform. We report a color center that shows a color center that shows insensitivity to environmental decoherence cause by phonons and electronic field noise: the neutral charge state of silicon vacancy (SiV^0). Through careful materials engineering, we achieved >80% conversion of implanted silicon to SiV^0. SiV^0 exhibits spin-lattice relaxation times approaching 1 minute and coherence times approaching 1 second. Its optical properties are very favorable, with ~90% of its emission into the zero-phonon line and near transform-limited optical linewidths. These combined properties make SiV^0 a promising defect for quantum network applications.
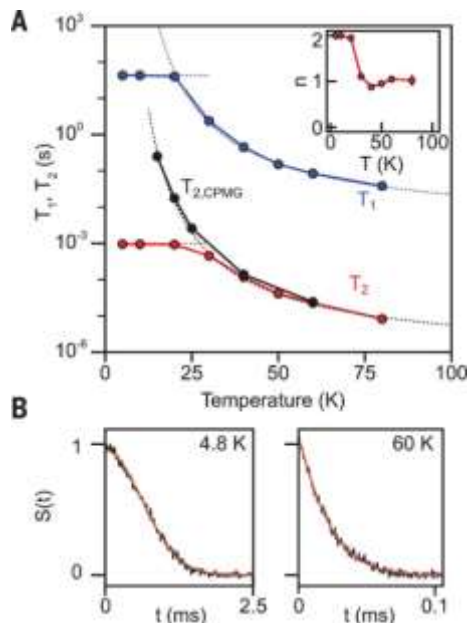
Figure 1: Spin relaxation time (T₁) and coherence time (T₂) measurements. (**A**) Temperature dependence of T₁ (blue symbols), T₂ (red symbols), and T₂,CPMG (black symbols) for SiV^0 measured on the $m_s = 0 \leftrightarrow +1$ transition of the orientation aligned with the magnetic field. Below 20 K, both T₁ and T₂ are independent of temperature, with T₁ = 43 ± 2 s and T₂ = 0.954 ± 0.025 ms. Above 20 K, both T₁ and T₂ show a temperature dependence consistent with an Orbach process with an activation energy of 16.8 meV (dashed blue and black lines are fits). Dynamical decoupling with CPMG (black symbols) extends the coherence time to T₂,CMPG =255 ± 20 ms at 15 K. (Inset) Temperature dependence of the exponential stretching factor, n, in the T₂ decay showing a step in the stretching factor at 20 K. (**B**) Selected Hahn echo decay curves illustrating n=2 in the low-temperature regime (4.8 K) and n=1 in the high-temperature regime (60 K).
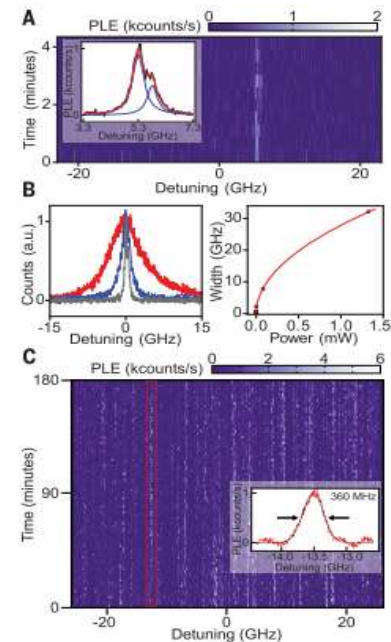
Figure 2: PLE spectroscopy. (**A**) PLE scan on a single center in the lightly implanted sample, showing a single line that is spectrally stable over ~4 min of interrogation. (Inset) PLE integrated over all scans (black), with the baseline subtracted (25). The fit (red) represents the sum of two overlapping Lorentzians (blue) with individual widths [full width at half maximum (FWHM)] of 450 and 499 MHz for the left and right peaks, respectively. (**B**) (Left) PLE scans of the line from (A) at different excitation powers: 150 nW (gray), 3.2μW (blue), and 81 μW (red), resulting in linewidths of 450 MHz, 2.2 GHz, and 7.8 GHz, respectively. (Right) The linewidth as a function of excitation power P, showing the power broadening in detail. The red line corresponds to $\Gamma(P) = G\sqrt{1+P/Po}$ where Γ is the FWHM of the optical transition, G= 0.255 GHz, and Po =78 nW. (**C**) Ensemble PLE in the heavily implanted sample. The scan reveals many lines that are stable across 80 iterations spanning a 3-hour period. (Inset) Gaussian fit to a single isolated peak, integrated over all of the scans, with the baseline subtracted, showing a FWHM of 360 MHz.

CITATIONS

➢ Rose, Brendon C., et al. "Observation of an environmentally insensitive solid-state spin defect in diamond." Science 361.6397 (2018): 60-63.

NANOPHOTONICS FOR TELECOM QUANTUM NETWORKS BASED ON NEUTRAL SILICON VACANCY CENTERS IN DIAMOND

DING HUANG

Researcher: **Ding Huang**
Advisor: **Nathalie P. de Leon (ELE)**
Sponsorship: **DARPA**

Quantum networks, which consist of distributed quantum nodes that are connected through entanglement, are promising for many quantum-enabled applications including secure communication, modular quantum computing and distributed sensing. A variety of experimental platforms have been pursued as possible candidates in realizations of quantum networks. Recent proof-of-principle demonstrations of key components for quantum networks include spin-photon entanglement, two photon interference, and entanglement of remote spins separated by more than 1 km. However, extending such demonstrations to beyond two nodes or to nodes separated by a longer distance will be challenging. This is because currently known platforms suffer from either short spin coherence time, the lack of an efficient, stable spin-photon interface or the attenuation of visible wavelengths in optical fiber.

Previous implementations of quantum network components using color centers in diamond have focused on the NV$^-$ center, which exhibits long spin coherence times even at room temperatures and has narrow, spin-conserving optical transitions. However, the NV$^-$ center suffers substantial spectral diffusion, and over 97% of emission is in an incoherent phonon side band. This severely limits its spin-photon entanglement generation rate. Alternatively, SiV$^-$ centers demonstrate more favorable optical properties, with 70% of its emission in the zero-phonon line and a narrow inhomogeneous linewidth. However, the SiV$^-$ electron spin coherence time is limited by the orbital relaxation to be 38 ns at liquid helium temperature, and requires dilution refrigerator temperatures to extend coherence to 13 us. We recently reported that the stabilization of the neutral charge state of silicon vacancy center, SiV^o, that exhibits spin-lattice relaxation times approaching 1 minute and coherence times approaching 1 second below 20 K. Additionally, the SiV^o center has efficient, stable optical transitions with ~90% of its emission into the zero-phonon line and near–transform-limited optical linewidths. The combination of its spin and optical properties makes SiV^o a promising defect for quantum network applications.

We aim to integrate this new defect into a nanophotonic platform in order to create an efficient spin-photon interface. Nanophotonic structures also allow us to manipulate the propagation and confinement of light at the wavelength-scale, leading to strong enhancement of light-matter interaction. In this talk, we will discuss our recent efforts to develop an integrated nanophotonic platform to efficiently collect photons from the neutral silicon vacancy color center (SiV^o) in diamond, and to subsequently convert their wavelength from their optical transition of 946 nm to the telecom band (i.e. ~1550 nm).
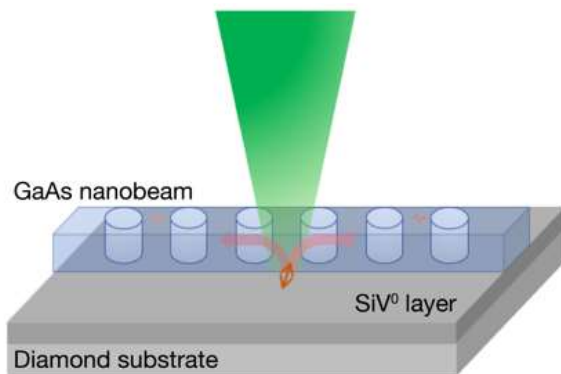
Figure 1: GaAs-on-diamond scheme, where GaAs nanobeam cavity evanescently couples to a SiVo center in diamond substrate.
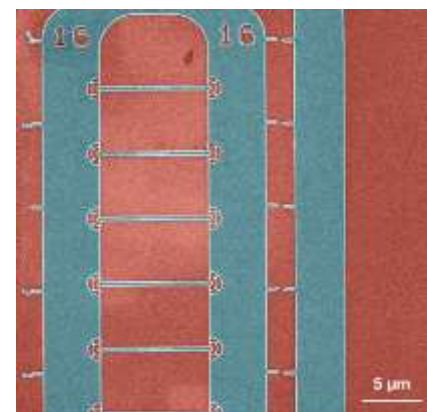
Figure 2: False color scanning electron microscope image of the GaAs nanobeam cavities (green) on top of diamond (red).

CITATIONS

➢ B. C. Rose, D. Huang, Z.-H. Zhang, P. Stevenson, A. M. Tyryshkin, S. Sangtawesin, S. Srinivasan, L. Loudin, M. L. Markham, A. M. Edmonds, D. J. Twitchen, S. A. Lyon, and N. P. de Leon, "Observation of an environmentally insensitive solid-state spin defect in diamond," Science **361**, 60-63 (2018).

Researcher: **Lila Rodgers**
Advisor: **Nathalie P. de Leon (ELE)**
Sponsorship: **NSF**

I am fabricating microwave striplines on a glass coverslip. We place our diamonds on top of these striplines to efficiently deliver microwaves to diamonds.

The microwaves allow us to manipulate the spin state of nitrogen-vacancy centers in diamond.
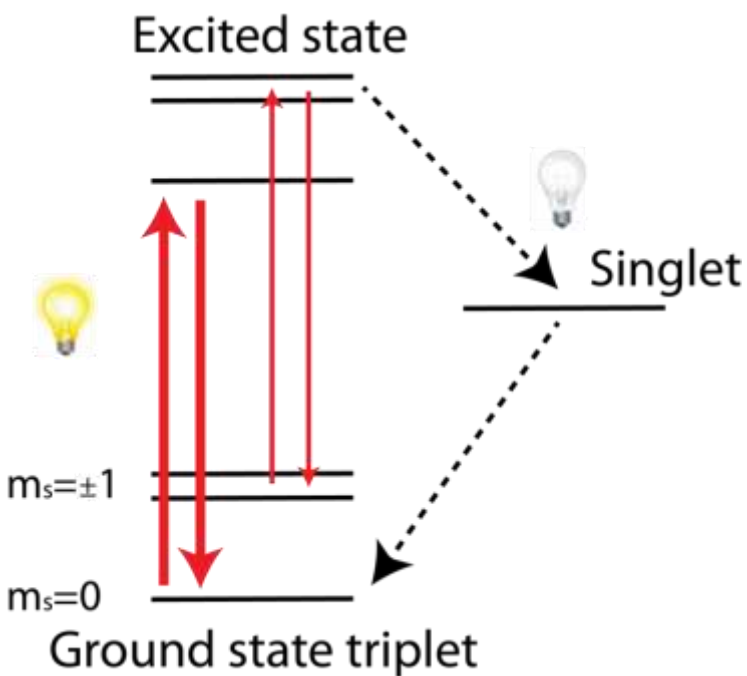
Figure 1: Energy structure of nitrogen vacancy centers in diamond. The ground state is a triplet with a zero field splitting of 2.87 GHz. This spin state can be manipulated by applying microwaves to the NV centers and can be read out optically through a spin-dependent fluorescence measurement.
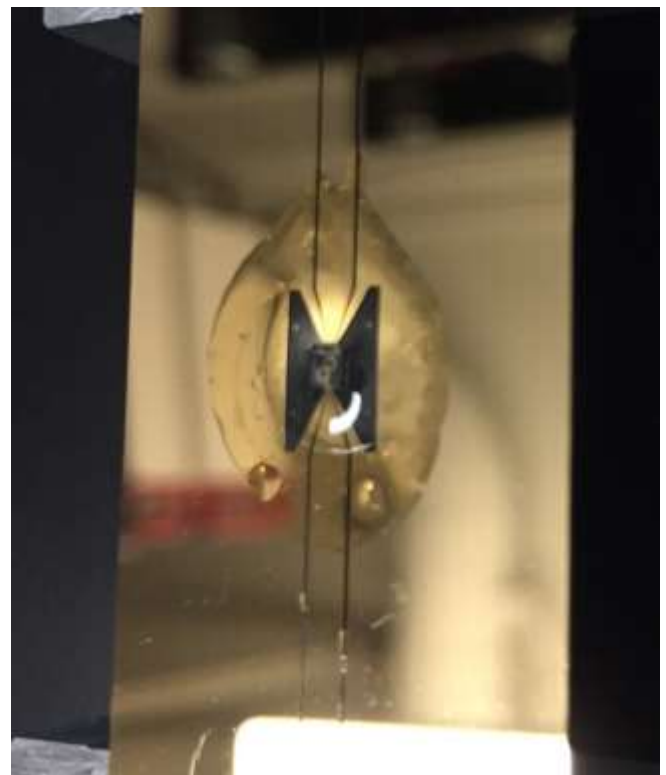
Figure 2: Diamond sample with shallow NV centers sits on top of a microwave stripline. These striplines are fabricated using the photolithography facilities at MNFL. Diamond is 2x2mm in size.

CITATIONS

➢ N/A

Researcher: **Zhiyang Yuan**
Advisor: **Nathalie P. de Leon (ELE)**
Sponsorship: **NSF**

The nitrogen vacancy (NV) center in diamond exhibits spin-dependent fluorescence and long spin coherence times under ambient conditions, enabling application in quantum information processing and sensing. NV centers near the surface can have strong interactions with external materials and spins, enabling new forms of nanoscale spectroscopy. However, NV spin coherence degrades within 100 nanometers of the surface, suggesting that diamond surfaces are plagued with ubiquitous defects. Prior work on characterizing near-surface noise has primarily relied on using NV centers themselves as probes; while this has the advantage of exquisite sensitivity, it provides only indirect information about the origin of the noise. Here we demonstrate that surface spectroscopy methods and single spin measurements can be used as complementary diagnostics to understand sources of noise. We find that surface morphology is crucial for realizing reproducible chemical termination, and use these insights to achieve a highly order, oxygen-terminated surface with suppressed noise. We observe NV centers within 10 nm of the surface with coherence times extended by an order of magnitude.
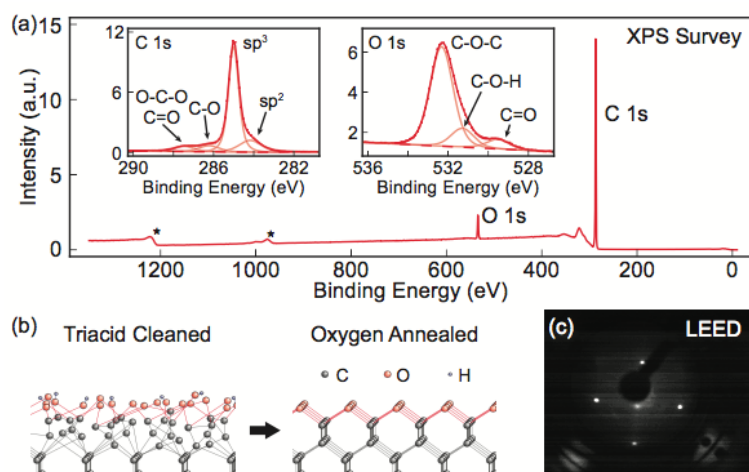
Figure 1 (left): Detailed characterization of the oxygen-annealed surface. (a) XPS survey scan showing dominant carbon and oxygen peaks. Peaks marked with * are Auger peaks associated with carbon and oxygen. Left-hand inset: High resolution XPS carbon 1s spectrum showing a dominant diamond sp3 peak with three side peaks assigned to sp2 carbon, and carbon singly and doubly bonded to oxygen. Right-hand inset: High resolution XPS oxygen 1s spectrum showing a dominant either (C—O—C) peak and two satellite peaks assigned to alcohol (C—O—H) and ketone (C=O). (b) Ball-and-stick diagrams illustrating the surface termination before and after oxygen annealing. The disordered, acid-cleaned surface hosts a mixture of groups, which transform into a highly ordered, predominantly either-terminated surface upon oxygen annealing. (c) LEED pattern showing a 1 x 1 reconstruction of the oxygen-annealed surface, consistent with ether termination.

Figure 2 (right): Creation of shallow NV centers with long coherence times. (a) Schematic showing an NV center near the diamond surface. The surface can host defects that produce electric and magnetic field noise. (b) Hahn echo coherence time T2, echo as a function of NV depth, measured across six samples with different surface conditions. Although the triacid-cleaned surfaces have different origins and processing histories, the relationship between T2, echo and depth is similar across all samples, and the high-temperature and oxygen-annealed sample exhibits significantly improved coherence times at the same depths. (c) Surface processing steps before implantation to remove surface polish damage and subsurface RIE damage, and after implantation to form NV centers and create a well-ordered oxygen surface termination. The high-temperature annealing step can be performed at 800 °C or 1200 °C. (d) AFM images of initial scaife-polished diamond (top) and the final surface after oxygen annealing (middle); scale bar is 100 nm. Confocal image (bottom) showing photoluminescence (PL) from individually resolvable NV centers; scale bar is 1 μm.
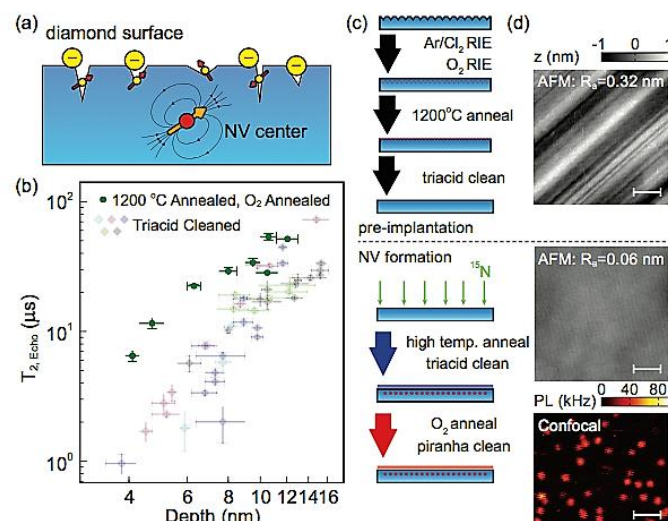
CITATIONS

➢ Sangtawesin, Sorawis, et al. "Origins of diamond surface noise probed by correlating single spin measurements with surface spectroscopy." arXiv preprint arXiv:1811.00144 (2018).

Researcher: **Ming Lyu**
Advisor: **Claire F. Gmachl (ELE)**
Sponsorship: **Internal Funding**

Long wavelength infrared light sources have been of great interest for a multitude of applications. For example, 16 µm laser beams have been widely used for selective multiphoton dissociation of UF6 [1]. In addition, this wavelength range contains absorption peaks for benzene (14.8 µm) and some of its derivatives, such as toluene (14.4 µm), aniline (19.8 µm) and phenol (14.5 µm). Detection of these chemicals is essential for both chemical engineering and environmental monitoring. However, commercially ready devices are not yet available.

Since its invention in 1994 [2], quantum cascade lasers (QCLs) have been a major source for mid-infrared light, but traditional InP-based QCLs have low performance at 16µm due to two-phonon absorption of InP in this region.

GaAs/AlGaAs heterostructure is widely used for semiconductor devices and in the THz QCLs but is not yet widely used for higher frequency like 16µm (19THz) [3]. We are exploring this material to achieve much-needed 16µm laser device.

Figure 1 is the microscope image of a mesa sample on GaAs/AlGaAs QC material. The bottom mesas are cleaved to semi-circles to create a facet for electro-luminescence light emission. Figure 2 shows the scanning electron microscope image of the cleaved facet of a mesa.

The QC material is grown by molecular beam epitaxy (MBE) in Prof. Loren Pfeiffer's group. We use the cleanroom primarily for photo-lithography, scanning electron microscope imaging, etching and metal deposition.
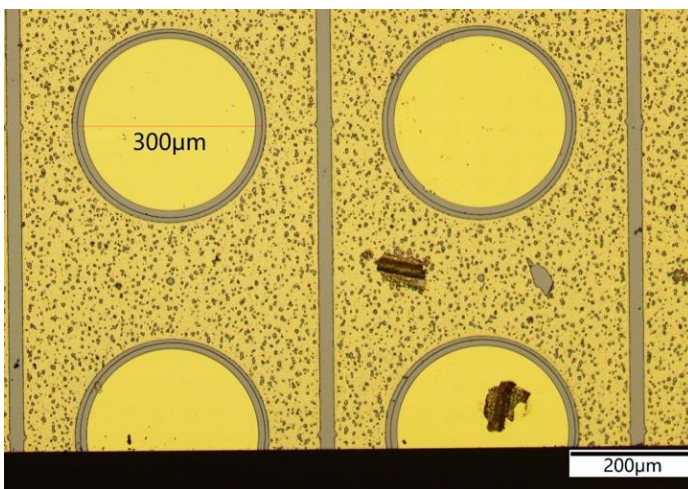
Figure 1: Microscope image of sample with fabricated mesas on quantum cascade material.
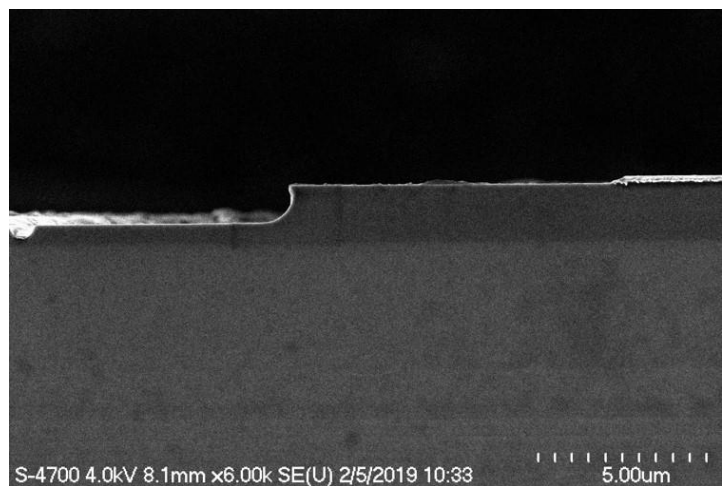
Figure 2: Scanning electron microscope image of the cross-section of a GaAs/AlGaAs mesa

CITATIONS

➢ [1] Y.Okada et al. Journal of Molecular Structure, 410 (Supplement C): 299 (1997). Poster on IR workshop 2017, "Design and Optimization of 14-20 m Wavelength GaAs/AlGaAs Quantum Cascade Lasers".
➢ [2] J. Faist et al. Science 264, 553 (1994).
➢ [3] Ulrich et al. Applied physics letters, 80(20), 3691-3693 (2002).

Researcher: **Michelle Zhang**
Advisor: **Claire F. Gmachl (ELE)**
Sponsorship: **NSF**

Multilayer plasmonic metamaterials exhibit anisotropic hyperbolic dispersion and enable non-magnetic negative refraction for potential applications such as superlensing and optical cloaking. However, since they mostly exhibit optical properties of metals, there is a trade-off between functionality and metallic loss, which is intrinsic to all plasmonic metamaterials. To provide optical loss compensation, one may integrate an active gain-medium into the plasmonic metamaterials; however, many schemes such as dye-doped metamaterials degrade easily or are not electronically tunable. Moreover, there is no active metamaterial with loss compensation in the mid-infrared (mid-IR) spectral region. In this work, we incorporate quantum cascade (QC) structures into plasmonic metamaterials and work towards the realization of active mid-IR metamaterials.
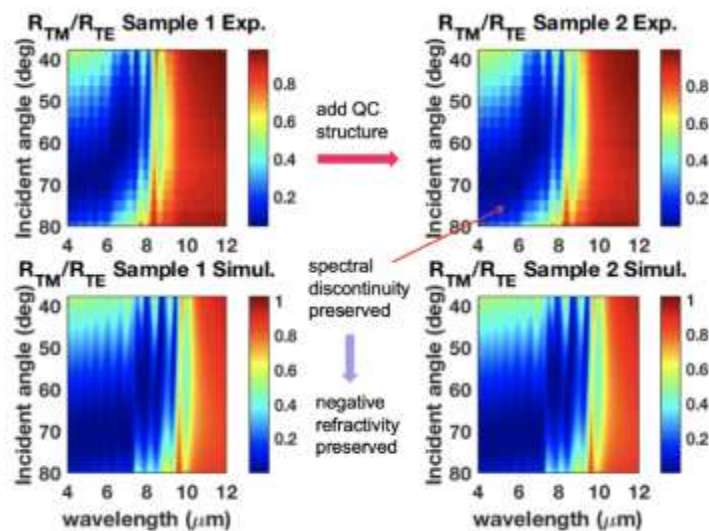
Figure 1: Experiment and transfer matrix simulation results of the reflectance for incoming TM/TE waves. The spectral discontinuity is preserved when quantum cascade structures are incorporated into the metamaterials.
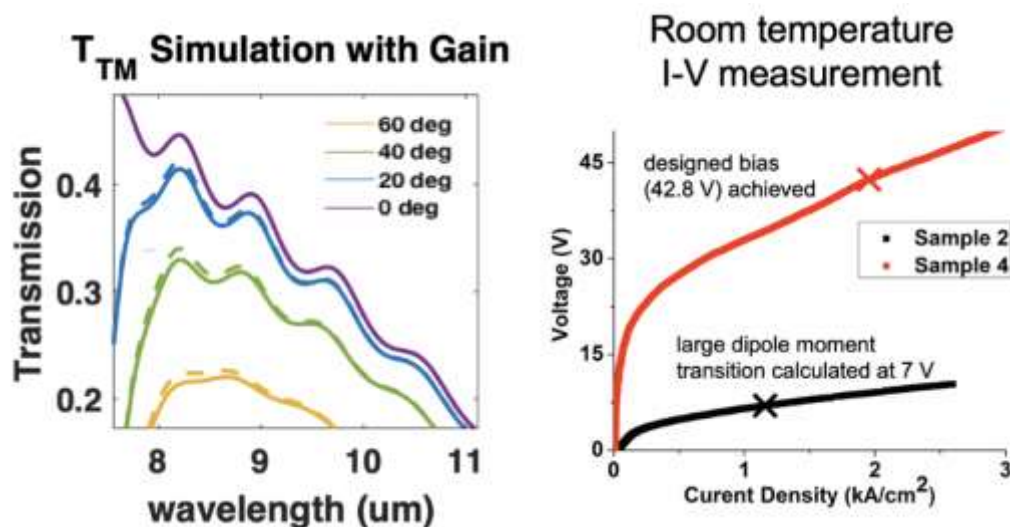
Figure 2: (Left) Transfer matrix simulation results of the transmission for incoming TM waves with gain. (Right) Room temperature current-voltage measurement.

CITATIONS

➢ Optoelectronic Plasmonic Metamaterials with a Quantum Cascade Structure Yezhezi Zhang, Wentao Fan, Alex Y. Song, Deborah L. Sivco, Claire F. Gmachl. CLEO 2018.

Researcher: **Harshvardhan Babla**
Advisor: **Andrew A. Houck (ELE)**
Sponsorship: **Internal Funding**

The transmon is a type of superconducting qubit formed by a Josephson junction in parallel with a capacitor. This setup closely resembles a conventional LC oscillator, whose Hamiltonian is a quadratic function of two non-commuting operators one corresponding to the charge accumulated on the capacitive pads and the other to the effective flux through the junction. However, the transmon fundamentally differs from the accumulated on the capacitive pads and the other to the effective flux through the junction. However, the transmon fundamentally differs from the LC oscillator in that the energy provided by the Josephson junction varies as an inverse cosine of the flux through it, instead of as a quadratic. This allows for an anharmonic spacing of the oscillator s energy levels. By fine-tuning the transmon s parameters, one can obtain a pair of low-lying energy levels that are sufficiently separated from the others, effectively creating a two-level system a qubit. The transmon suffers from dielectric loss from the sapphire substrate between the Josephson junction s capacitive pads. The unused bonds on the substrate s surface act as two-level systems that couple to the electric field between the two capacitive pads, causing unpredictable variation in the field. This loss specifically affects the qubit s T_1 the time constant that characterizes the qubit s relaxation into an equilibrium with the surroundings. This summer, I hope to counteract this loss by fabricating chips that have the capacitive pads much closer together, such that the field between them has a smaller surface area along which to interact with the substrate s dangling bonds. I expect that by optimizing the transmon qubit for dielectric loss, I can verify a method to improve T_1 for all qubits that use a large capacitance to manipulate anharmonic oscillators. I am truly enthusiastic to work in an emerging and exciting field in engineering.
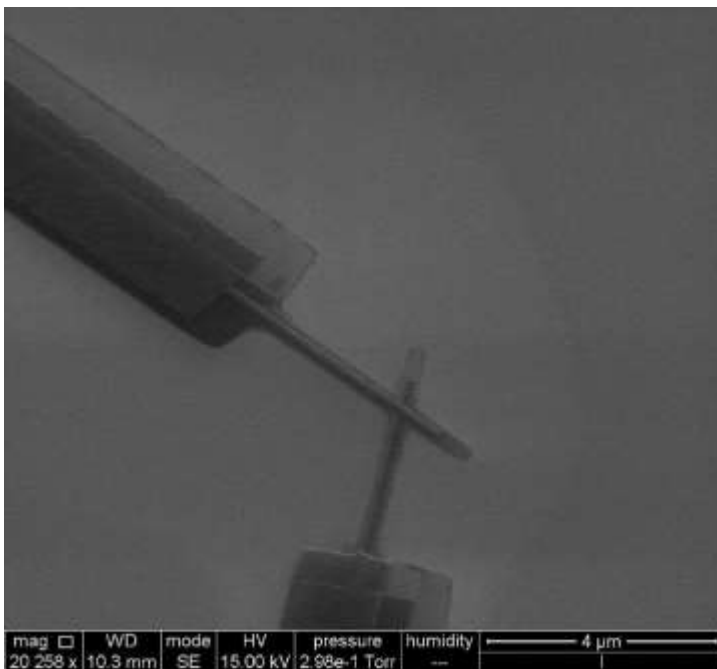
Figure 1: Manhattan Implementation of a Josephson Junction.
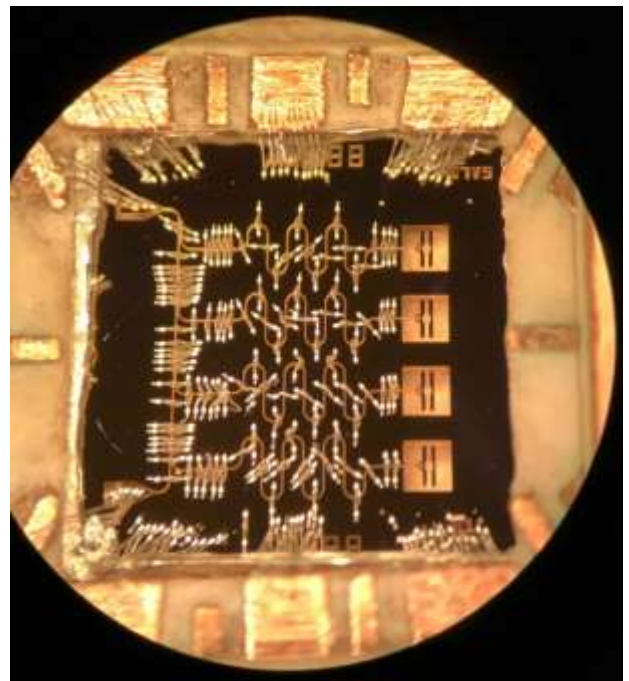
Figure 2: A Series of Transmon devices.

CITATIONS

➢ J. Koch et al., "Charge-insensitive qubit design derived from the Cooper pair box," Phys. Rev. A 76, 04319 (2007), doi:10.1103/PhysRevA.76.042319, arXiv:0703002.

Researcher: **Jacob Bryon**
Advisor: **Andrew A. Houck (ELE)**
Sponsorship: **NSF, DoD**

Microwave resonators on Nb and NbTiN.
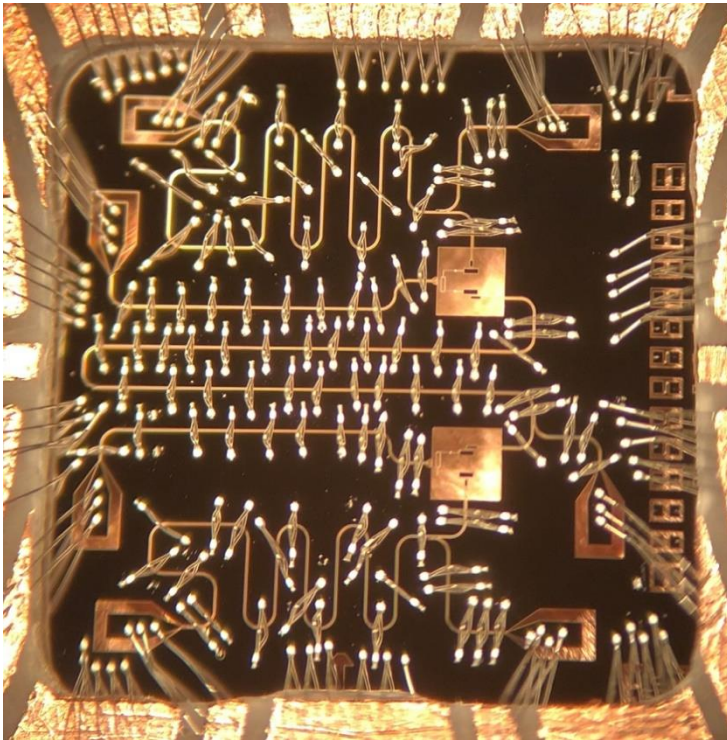
Figure 1: Image of device fabricated in the PRISM cleanroom for exploring new two qubit interactions for superconducting quantum computing and simulation.
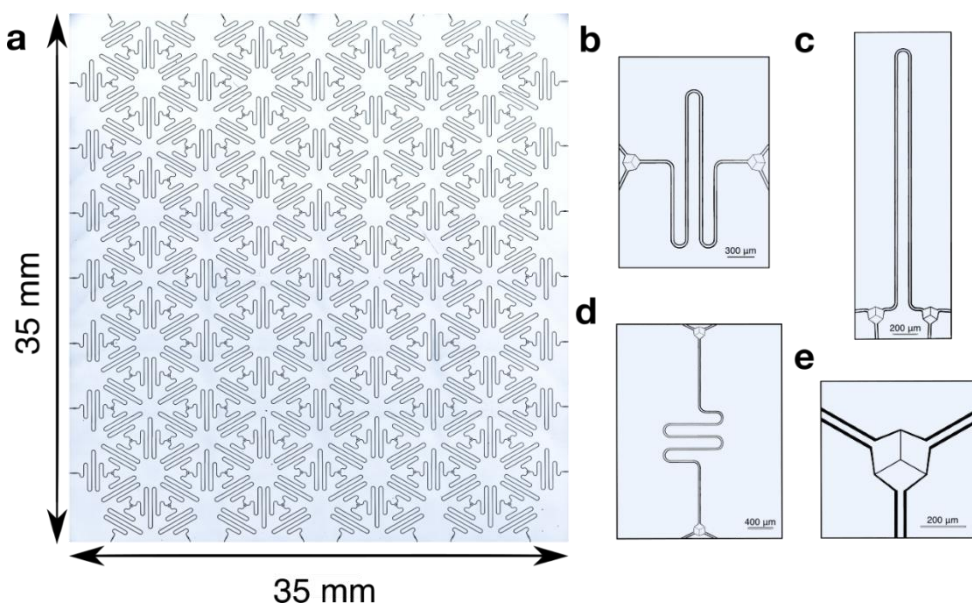
Figure 2: (a) Picture of a Euclidean lattice of CPW microwave resonators, modified from [15]. (b)-(d) Three mathematically identical resonators with different shapes but the same resonance frequencies and hopping rates. (e) Close-up of a capacitive coupler like the ones used in (a)-(d) to connect three resonators together. The effective hopping rate at this junction is set by the capacitance between the three arrow-shaped center pins.

CITATIONS

➤ Fitzpatrick, et al. Phys. Rev X 7 011016 (2017).

Researcher: **Andras Gyenis**
Advisor: **Andrew A. Houck (ELE)**
Sponsorship: **ARO**

Encoding a qubit in logical quantum states with wavefunctions characterized by disjoint support and robust energies can offer simultaneous protection against relaxation and pure dephasing. Using a circuit-quantum-electrodynamics architecture, we experimentally realize a superconducting 0-π qubit, which hosts protected states suitable for quantum-information processing. Our multi-tone spectroscopy measurements reveal the energy level structure of the system, which can be precisely described by a simple two-mode Hamiltonian. We find that the circuit realizes an effective one-dimensional crystal with two sub-lattices, where the geometrical phase difference between Wannier states localized at adjacent phase unit cells leads to interference effects associated with tunneling of pairs of Cooper pairs. The parity symmetry of the qubit results in charge-insensitive levels connecting the protected states, allowing for logical operations. The measured relaxation (1.6 ms) and dephasing (25 μs) demonstrate that our implementation of the 0-π circuit not only broadens the family of superconducting qubits, but also represents a promising candidate for the building block of a fault-tolerant quantum computer.
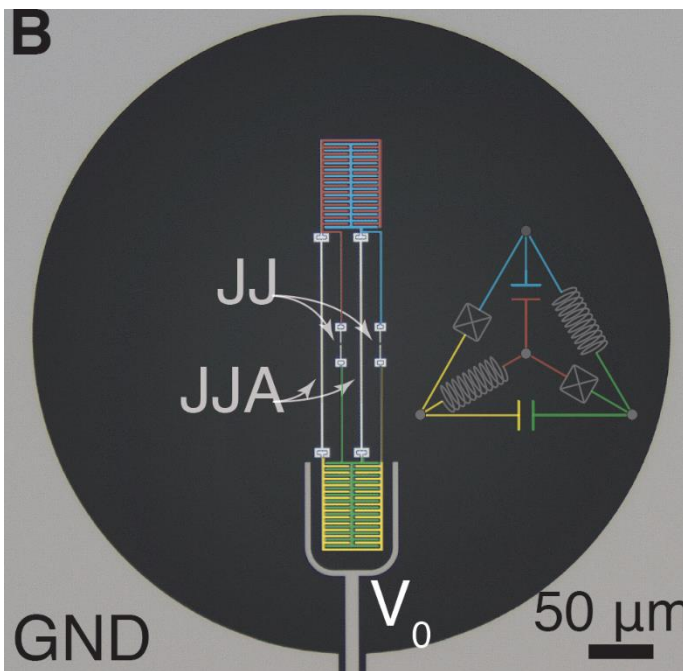
Figure 1: Optical image of the 0-π superconducting qubit.
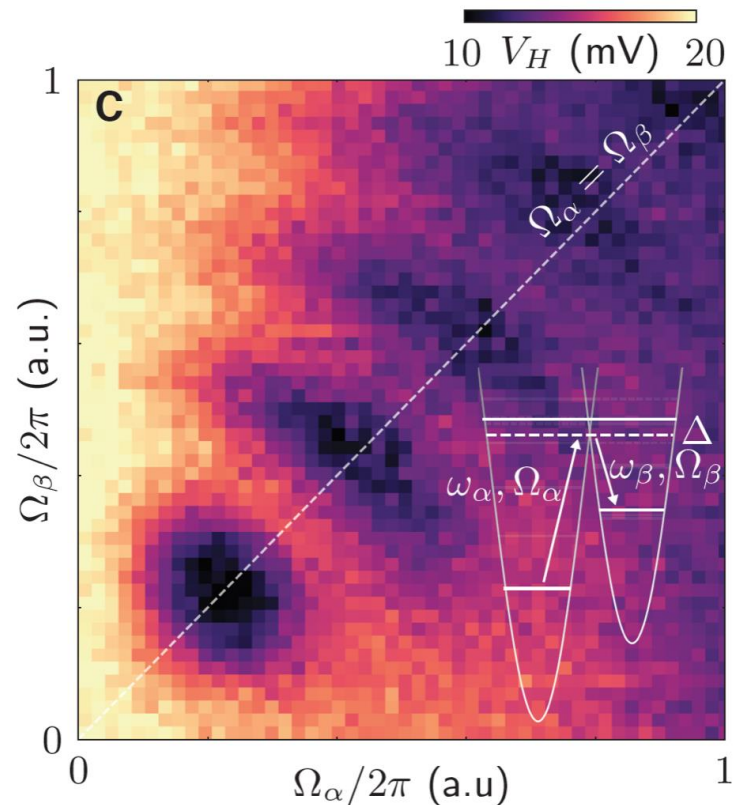
Figure 2: Rabi oscillation and coherent oscillation between the logical qubit states.

CITATIONS

➢   arXiv:1805.00938

Researcher: **Berthold Jack**
Advisor: **Andrew A. Houck (ELE)**
Sponsorship: **None**

The application of superconducting qubits for quantum information processing will require systematically reducing noise and dissipation in these systems. However, there is multiple dissipation channels existing in such systems and it requires a systematic study to identify the influence of fabrication process parameters on the qubit performance. The goal of this project is an end-to-end optimization of the manufacturing process of so-called transmon qubits that integrates multiple small improvements together by reducing fabrication-related loss channels. Unveiling and eliminating dissipation channels through such a systematic analysis will contribute towards higher performance qubits with uniform key parameters, a pre-requisite for solid-state quantum computing. In this regard, we investigated the influence of material properties on the performance of transmon qubits. We fabricated transmon qubits from superconducting niobium films, which were prepared using different thin film growth techniques. We experimentally determined the qubit relaxation time, T_1, of these devices as a quantitative measure of the qubit performance (Figure 1). Comparing the measured T_1 of these devices (Figure 2), we observe a systematic dependence of the qubit performance on the thin film growth technique. In the next step of this project we will apply spectroscopy and imaging techniques to shed light on the microscopic origin of this observed behavior.
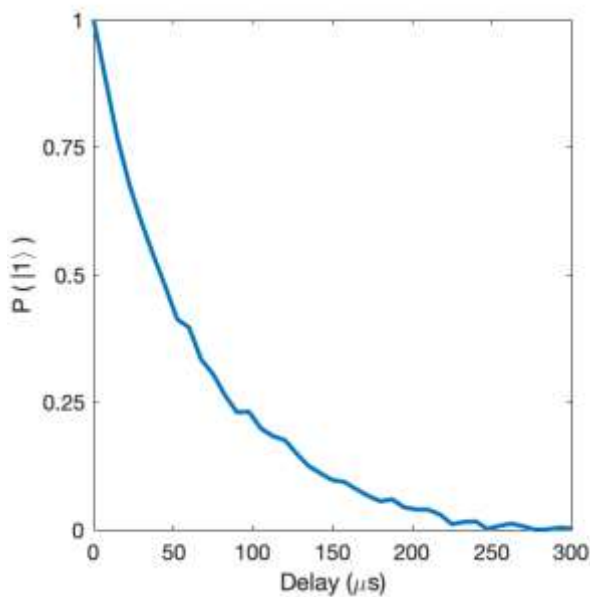
Figure 1: Measurement of the qubit relaxation time T_1. Shown is the measured probability to find the transmon qubit in the excited |1> state as a function of the time delay between the π-pulse and qubit the read-out using a microwave cavity.
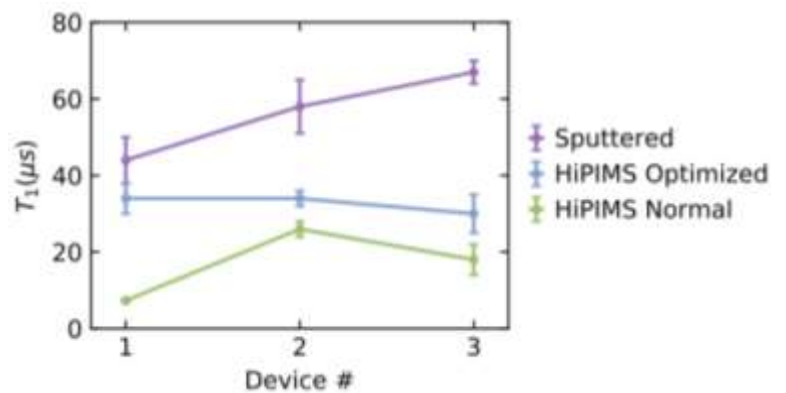
Figure 2: Comparison of qubit performance for different film preparation techniques. Shown are the T1 times for transmon qubits made from superconducting films prepared using different fabrication techniques ('Sputtering', 'HIPIMS Optimized', 'HIPIMS Normal'). The T_1 times were determined by an exponential fit to the decay characteristics shown in Figure 1.

CITATIONS

➢ A. Nersisyan et al., arXiv:1901.08042 [quant-ph]

Researcher: **Pranav Mundada**
Advisor: **Andrew A. Houck (ELE)**
Sponsorship: **ARO**

Quantum states with disjoint support are inherently protected against qubit relaxation. In the o–π architecture, first order insensitivity to dephasing can further be obtained by engineering a sweet spot for the external flux. Using a circuit-quantum-electrodynamics architecture, we experimentally realize this superconducting o–π qubit, which hosts protected states suitable for quantum-information processing. Multi-tone spectroscopy measurements reveal the energy level structure of the system, which can be precisely described by a simple two-mode Hamiltonian. We find that the parity symmetry of the qubit results in charge-insensitive levels connecting the protected states, allowing for logical operations. The measured relaxation (1.6 ms) and dephasing times (25 μ s) demonstrate that our implementation of the o–π circuit not only broadens the family of superconducting qubits, but also represents a promising candidate for the building block of a fault-tolerant quantum processor.
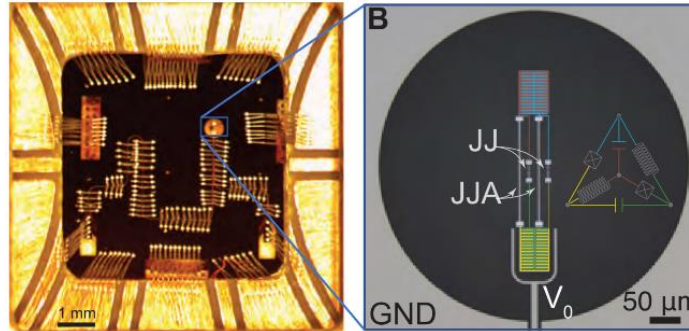

Figure 1: Optical image of a wire-bonded 0 – π device mounted into the sample holder. (B) False-color optical image of the 0 – π device with colors referring to the four nodes of the circuit. GND: ground plane of the resonator; V0: centerpin of the resonator; JJ: Josephson junction; JJA: Josephson junction array.
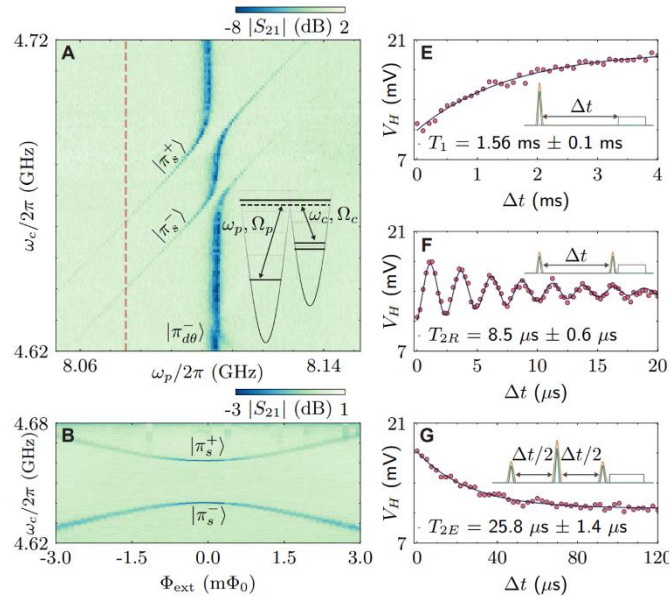
Figure 2: (A) Autler-Townes spectroscopy (background subtracted) between the ground states of the 0 – π qubit using the ancillary |π$^-_{d\theta}$> level. Inset shows the continuous drive scheme. (B) Raman spectroscopy at the detuning of Δ/2π = -30 MHz from the ancillary level [red dashed line in (A)] as a function of external magnetic field, which demonstrates a magnetic sweet spot for the disjoint ground states. (E to G) Relaxation, Ramsey and spin-echo measurements of the protected |π^+_s> state, with insets showing the pulse scheme (Δ/2π = -4 MHz and σ = 200 ns). All data were taken at n$^\theta_q$ = 0.25 charge bias point.

CITATIONS

➢   https://arxiv.org/abs/1910.07542

Researcher: **Anjali Premkumar**
Advisor: **Andrew A. Houck (ELE)**
Sponsorship: **ARO**

Researchers across academia and industry are exploring superconducting qubits as a promising implementation of quantum computing. This work explores the fluxonium qubit, which is made from a Josephson junction, a capacitor, and an inductor, usually made from a Josephson junction array. Fluxonium qubits in a particular parameter regime are intrinsically protected against relaxation from the excited state (logical 1) to the ground state (logical 0). We aim to show that this intrinsic protection allows for multi-layer chips where device layers are separated by dielectric material. This approach would be much faster, stable, and less resource-intensive than current implementations of 3D integration for superconducting quantum devices.
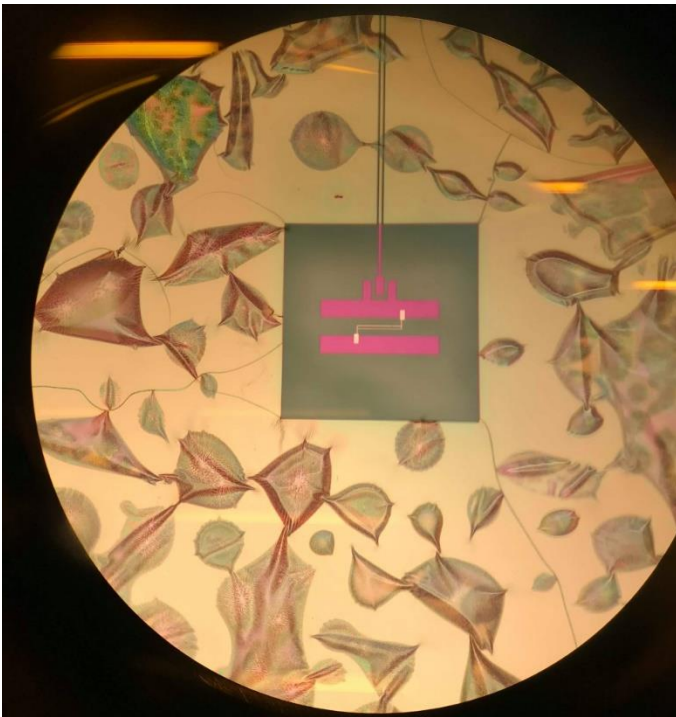
Figure 1: Fluxonium qubit after plasma-enhanced chemical vapor deposition (PECVD) of SiN. Photoresist was patterned such that only the qubit (purple) would be covered in SiN after a liftoff process.
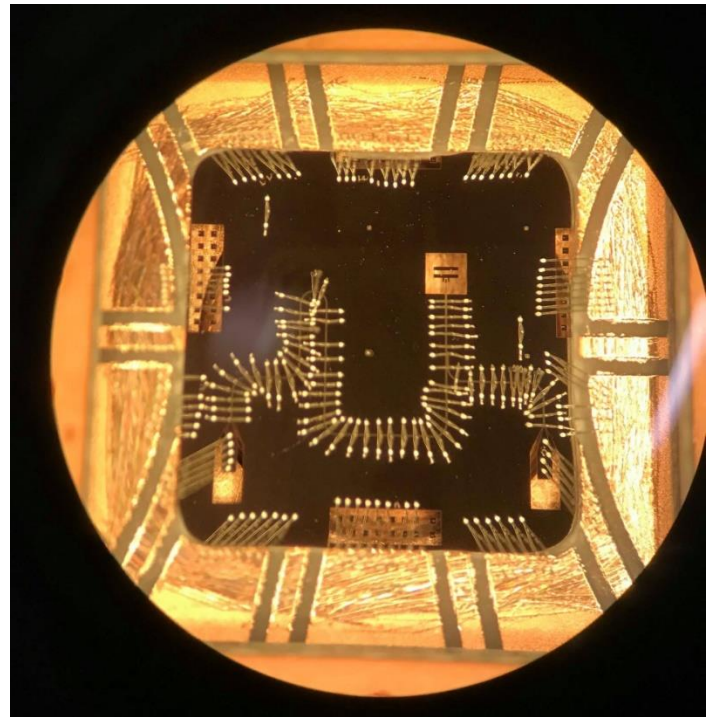
Figure 2: Completed fluxonium qubit device. The qubit is controlled and measured through a coplanar waveguide resonator. Wirebonds connect input/output lines and the ground plane to a copper PCB.

CITATIONS

- None

Researcher: **Basil Smitham**
Advisor: **Andrew A. Houck (ELE)**
Sponsorship: **NSF**

In response to external drive, a nonlinear system can exhibit in addition to the standard linear response limit cycle and chaotic behavior. This project studies limit cycles and chaos in driven-dissipative, nonlinear microwave cavity lattices. The lattices are formed from coupling coplanar waveguide microwave cavities together using either two- or three-way capacitive junctions, and the nonlinearity is introduced through current dependent kinetic inductance. Limit cycles and chaos are characterized through a variety of methods (such as computing Lyapunov exponents) used to analyze time-domain and frequency-domain data.
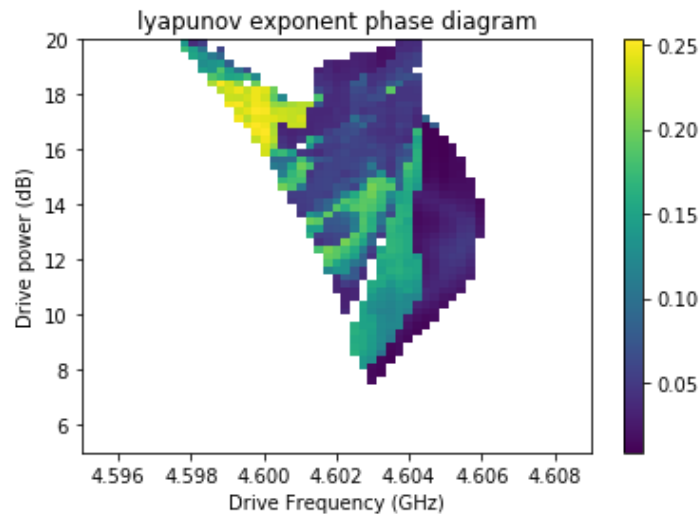
Figure 1: Lyapunov exponent phase diagram. Cavity array is driven by microwave tone at specified power and frequency, and a single trace of the corresponding output signal is taken in the IQ plane. The Rosenstein algorithm is then used to calculate the largest Lyapunov exponent of this IQ trace.
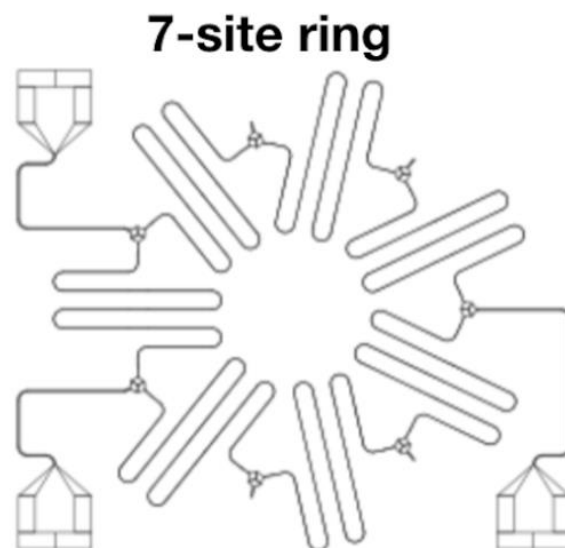
Figure 2: Device design: chain of 7 kinetic-inductance nonlinear resonators, which are capacitively inter-coupled. The resonators are designed to have their fundamental frequencies at around 2.3 GHz. Three input/output lines allow for microwave drive and readout.

CITATIONS

➤ N/A

Researcher: **Sara Sussman**
Advisor: **Andrew A. Houck (ELE)**
Sponsorship: **ARO**

Superconducting qubit stability can be substantially improved by minimizing sources of dissipation at all device interfaces. Many of the steps involved in fabricating a superconducting qubit aim to minimize dissipation. Before beginning fabrication in the MNFL cleanroom, we design the resonator and qubit patterns in AutoCAD and then use simulation tools ANSYS Maxwell and ANSYS HFSS to verify the capacitances between various components of the pattern and back out the qubit parameters. These patterns will be etched into a thin layer of a superconducting metal (e.g. niobium) that is sputtered on top of a substrate (e.g. sapphire, silicon). Once our design is finished, we fabricate the superconducting chip, wirebond and package the chip, and mount it in the fridge, connecting it to the resonator transmission line. Then we close up

the fridge, cool it down to 10 mK and begin making measurements.

For example, I recently worked on the design for a transmon qubit with an unconventionally low characteristic frequency (Figure 1). Although this low frequency qubit is more readily excited by thermal noise, it is also inherently more stable if you use a control scheme with "active reset", like the FPGA-based fast initialization control scheme that I am developing. This qubit was fabricated in MNFL and QDNL and it was packaged in the MNFL packaging lab. My measurements of the resulting device showed proof-of-principle data that we had created a qubit (Figure 2). I am currently working on creating a 3D second-generation qubit which should be more stable.
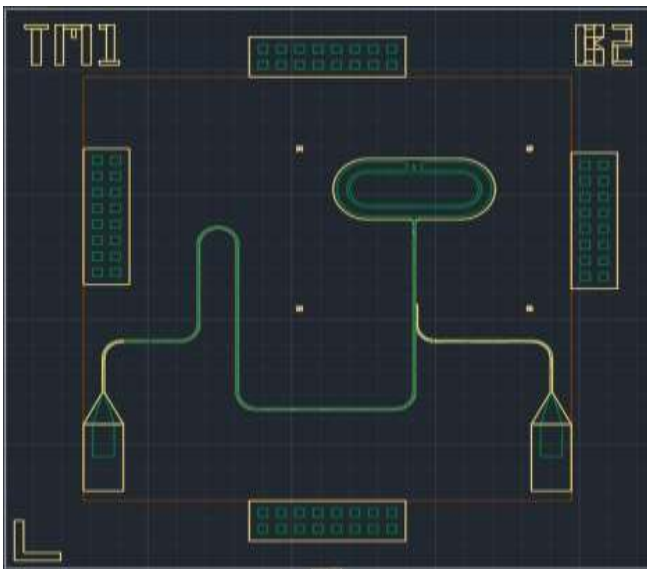
Figure 1: A superconducting qubit chip design (actual size is 7 mm x 7 mm). The microwave tone enters through the left input pad and goes up the coplanar waveguide resonator to capacitively couple with the qubit nonlinear LC circuit in the middle of the chip (the oval cutout is the top plate of the capacitor). The tone exits through the right output pad, its transmission profile altered by the qubit state. In this design, regions surrounded in green indicate a thin layer of superconductor (e.g. niobium), regions between green and yellow indicate exposed substrate (e.g. sapphire), and regions outside the yellow region indicate grounded superconductor.
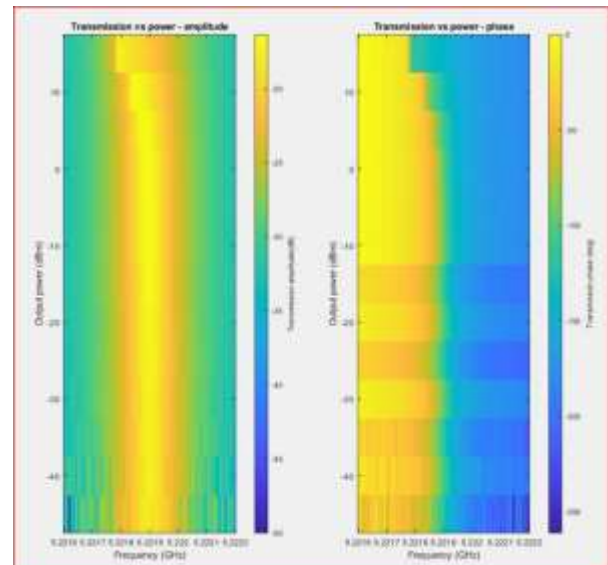
Figure 2: Transmission as a function of cavity power for the low frequency qubit I helped design. The nonlinearity at high power indicates the presence of a qubit. The cavity frequency spread is about 0.4 MHz and the frequency shift is about 0.1 MHz. In my next design I hope to increase the qubit-cavity coupling so I can better control the qubit's logical states.

CITATIONS

➤ N/A

Researcher: **Marius Andrei Vrajitoarea**
Advisor: **Andrew A. Houck (ELE)**
Sponsorship: **NSF**

Superconducting circuits have emerged as a rich platform for emulating synthetic materials composed of artificial atoms and photonic lattices. Here, we apply this toolbox for exploring the physics of a quantum impurity coupled to a photonic crystal. In previous experiments, strongly coupling a transmon qubit to the band structure of a stepped impedance waveguide filter has led to the first observation of atom-photon dressed bound states. In this work we push the coupling strength even further to go beyond the single-photon limit. Our platform consists of a photonic crystal implemented as a linear array of 26 coupled microwave resonators, and a fluxonium qubit galvanically coupled to one resonator site. Tuning the coupling strength, we can reach a regime where counterrotating terms become relevant and multiphoton bound states participate in the single-photon scattering dynamics. Additionally, by probing the transmission response for each discrete bath mode subject to a qubit drive, we can extract the spin-bath susceptibilities that capture correlations between the impurity and the harmonic degrees of freedom in the photonic crystal.
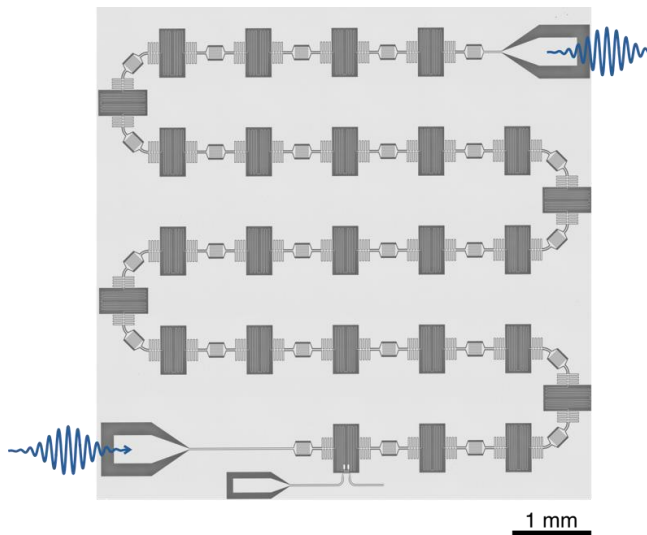
Figure 1: Optical image of photonic crystal implemented as a 1D array of capacitively coupled microwave resonators. A fluxonium artificial atom, consisting of many Josephson junctions, is galvanically coupled to the one of the edge resonators.
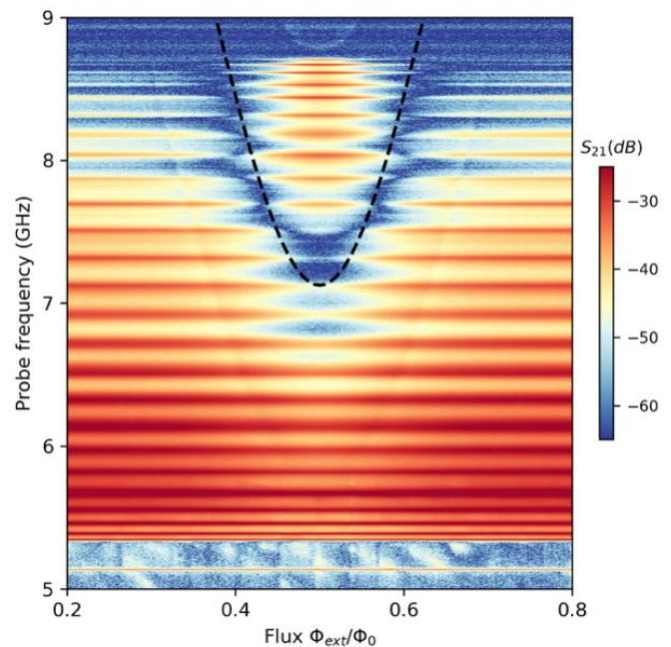
Figure 2: Microwave transmission through the photonic crystal as a function of magnetic flux applied to the qubit. Extinction in transmitted power corresponds to destructive interference between the incoming probe field and the field reflected by the qubit. Dashed lines: flux dispersion of the qubit transition energy.

CITATIONS

- None at this time

Researcher: **Kyle Castoria**
Advisor: **Stephen A. Lyon (ELE)**
Sponsorship: **NSF**

This research focuses on studying electrons bound to the surface of superfluid helium. This system provides a very clean surface for the electrons with which we can study interesting 2DEG phenomena like the quantum melting of a Wigner crystal. Due to the isolation of the electrons from their environment, this system is also a

candidate physical implementation of a memory qubit for quantum computers. For our research, we must control the electrons via gates submerged below the liquid helium surface. The fabrication of these gates requires the use of the MFNL.
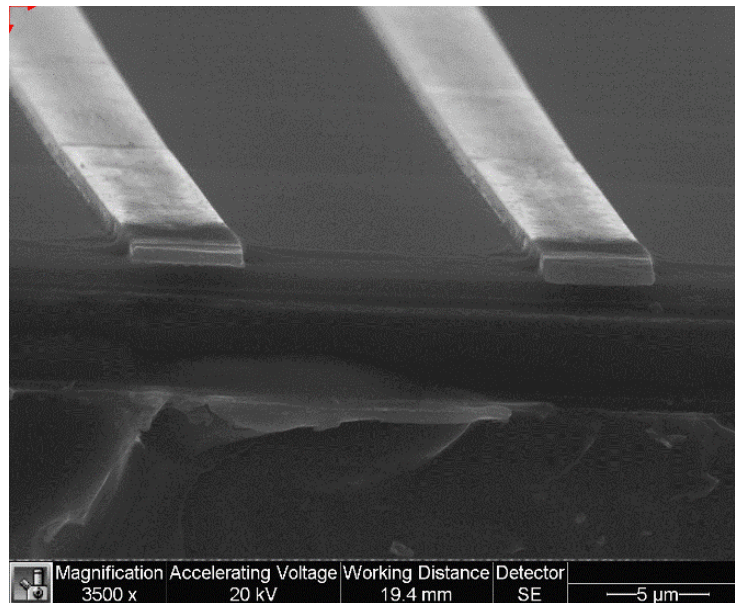
Figure 1
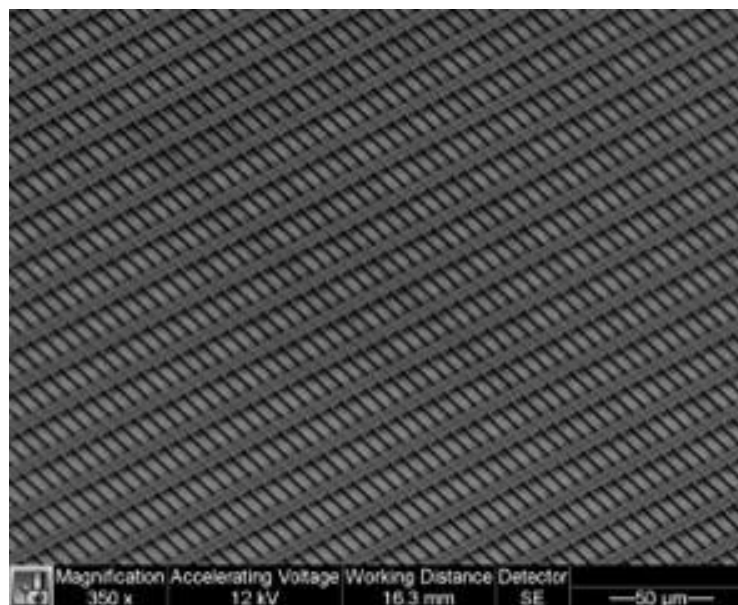
Figure 2

CITATIONS

➢   S. A. Lyon, Phys. Rev. A: At., Mol., Opt. Phys., 2006, 74, 052338.

Researcher: **Simon Bilodeau**
Advisor: **Paul R. Prucnal (ELE)**
Sponsorship: **No Sponsor**

Post-processing of foundry chips and miscellaneous microfabrication and packaging tasks for the Lightwave Lab's integrated photonics efforts, including RF photonics, ultrafast signal processing, and optical neural networks.
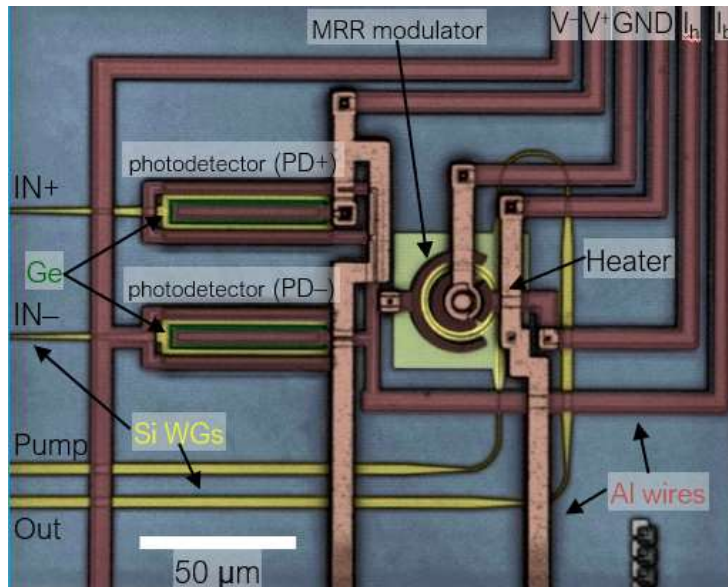
Figure 1: Silicon photonic modulator-class activation unit. This performs the nonlinear activation function of an artificial neuron, but at optical modulator speeds (up to tens of GHz). Figure from Tait et al.
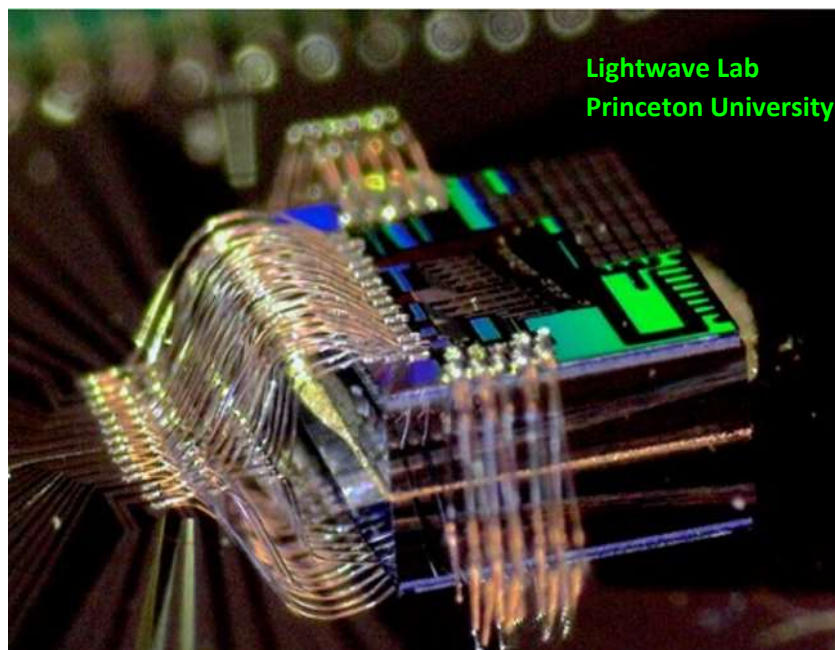
Figure 2: Photonic integrated neural network wirebonded to interposer (previous silicon version). Picture from Lightwave Lab.

CITATIONS

➤ Tait, A. N., Ferreira de Lima, T., Nahmias, M. A., Miller, H. B., Peng, H.-T., Shastri, B. J., & Prucnal, P. R. (2019). Silicon Photonic Modulator Neuron. Physical Review Applied, 11(6), 064043. https://doi.org/10.1103/PhysRevApplied.11.064043.

Researcher: **Thomas Ferreira de Lima**
Advisor: **Paul R. Prucnal (ELE)**
Sponsorship: **NSF**

The proposed program represents a vertically integrated approach to creating extremely high-performance processors based on photonics. We propose to investigate new devices, architectures, and evaluation standards, all of which must work in concert for the success of the program. Device research will push the limits of the electro-optic modulators that are central to the performance of the proposed approach.

Using existing silicon photonic manufacturing platforms, we will perform the first experimental demonstrations of scalable neuromorphic photonic architectures. With hardware-validated models of such devices and architectures, we can begin to establish evaluation standards that will frame the proposed technology within the broader context of future computing.
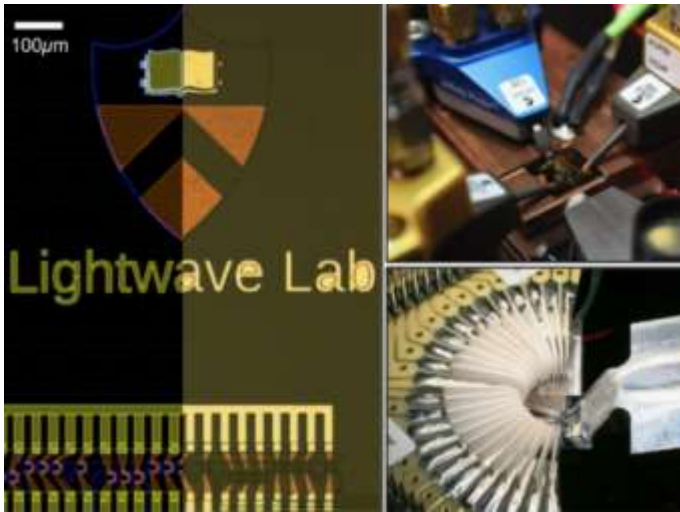
Figure 1: (Left) Side-by-side comparison of a computer design and a microscope picture of the fabricated photonic chip. (Right) Integrated photonics test and measurement platforms at the Lightwave Lab.
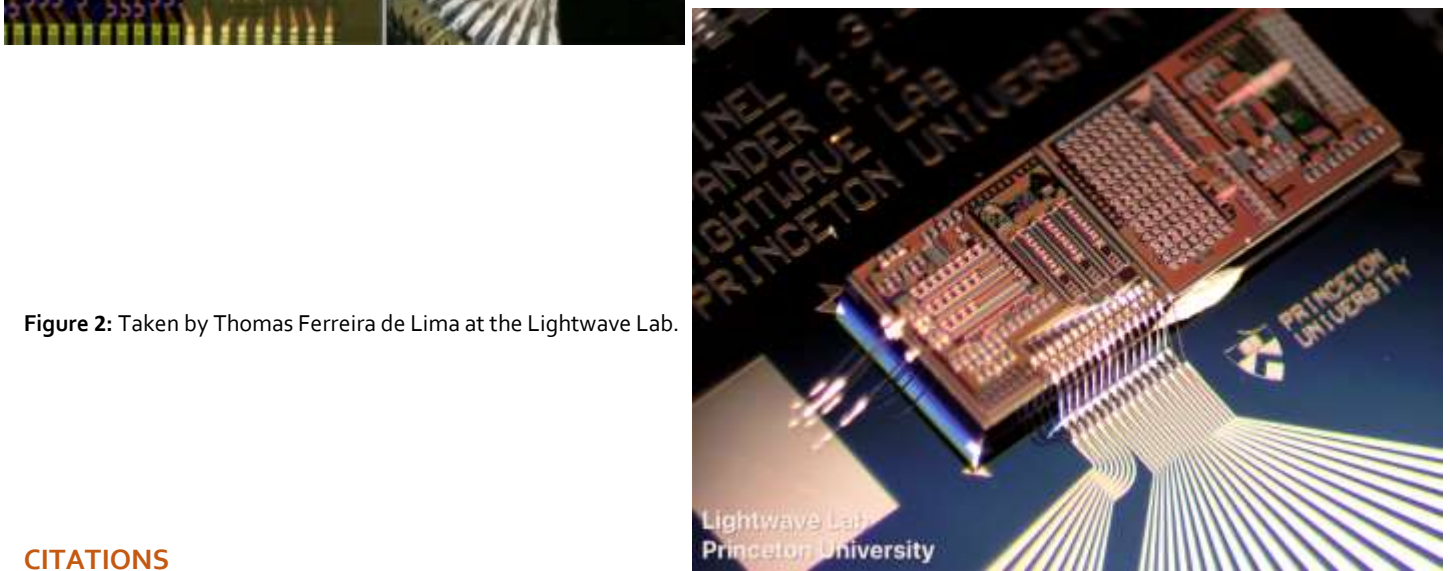
Figure 2: Taken by Thomas Ferreira de Lima at the Lightwave Lab.

CITATIONS

➢ Tait, Alexander N; Jayatilleka, Hasitha; Ferreira de Lima, Thomas; Ma, Philip Y; Nahmias, Mitchell A; Shastri, Bhavin J; Shekhar, Sudip; Chrostowski, Lukas; Prucnal, Paul R; Feedback control for microring weight banks Optics express 26 20 26422-26443 2018.

➢ Tait, Alexander N; Ferreira de Lima, Thomas; Zhou, Ellen; Wu, Allie X; Nahmias, Mitchell A; Shastri, Bhavin J; Prucnal, Paul R; Neuromorphic photonic networks using silicon photonic weight banks Scientific reports 7 1 7430 2017.

➢ Shastri, BJ; de Lima, T Ferreira; Tait, AN; Nahmias, MA; Prucnal, PR; Emergence of Neuromorphic Photonics Photonics in Switching PTu3C. 4 2017.

➢ Tait, Alexander N; Wu, Allie X; Ferreira de Lima, Thomas; Zhou, Ellen; Shastri, Bhavin J; Nahmias, Mitchell A; Prucnal, Paul R; Microring weight banks IEEE Journal of Selected Topics in Quantum Electronics 22 6 312-325 2016.

➢ Ferreira de Lima, Thomas; Peng, Hsuan-Tung; Tait, Alexander; Nahmias, Mitchell A; Miller, Heidi; Shastri, Bhavin J; Prucnal, Paul; Machine Learning with Neuromorphic Photonics Journal of Lightwave Technology 2019.

Researcher: **Kwangdong Roh**
Advisor: **Barry P. Rand (ELE)**
Sponsorship: **AFOSR**

Extensive research has established organic-inorganic hybrid perovskites as a promising material for optoelectronic device applications. Especially for lasers, many optically driven amplified spontaneous emission and lasing reports have been demonstrated across the near infrared to the green in various configurations (distributed feedback (DFB), distributed Bragg reflectors, photonic crystals, etc.) and pumping regimes (from pulsed to continuous-wave excitation) at low threshold, allowed by the tunable bandgap energy by controlling halide stoichiometry or material dimensionality. However, most reports lack red-emitting lasing action at room temperature due to undesirable halide phase separation that produce iodide-rich and bromide-rich domains in mixed-halide perovskites under intense illumination, resulting in a red gap problem where bandgap becomes pinned to the lower iodide-rich phase. Here we demonstrate a red-emitting 2nd-order DFB laser operating at room temperature from solution-processed organic-inorganic hybrid perovskite thin films for the first time. Ultra-flat mixed-halide perovskite layers were prepared on a quartz grating to achieve single-mode surface-emitting laser emission for at least a few tens of minutes (~106 pulses) with a threshold of 85 J/cm2 and full-width-half-maximum of less than 1.5 nm under picosecond-pulsed optical excitation. We effectively suppress phase separation by properly choosing self-assembled long-chain organic ammonium halide additives to enable stable lasing action over a wide range of wavelengths near the red. Our results provide a significant step towards full-color visible laser device applications from cost-effective halide perovskite material systems.
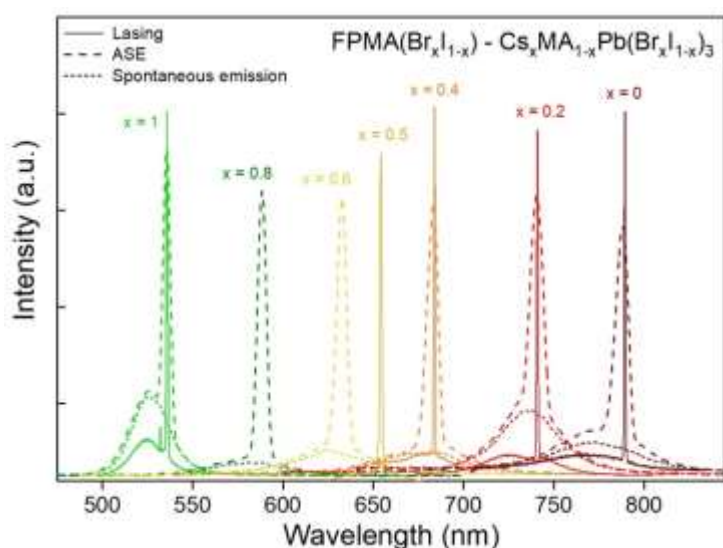
Figure 1: Room temperature single-mode surface-emitting DFB lasing in a wide spectral range from mixed-halide perovskite thin films.
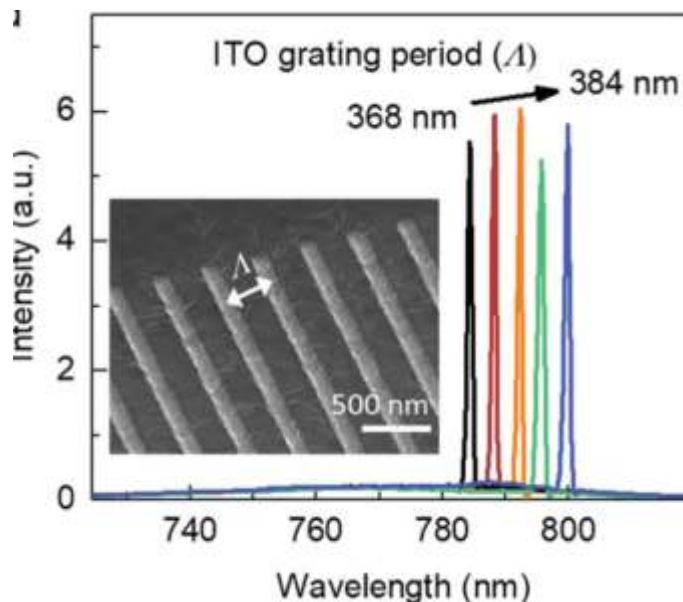
Figure 2: Tunable single-mode lasing emissions controlled by the periodicity of grating.

CITATIONS

➢ Roh, Kwangdong, et al. "Widely tunable, room temperature, single-mode lasing operation from mixed-halide perovskite thin films." ACS Photonics 6.12 (2019): 3331-3337.
➢ Kim, Hoyeon, et al. "Optically Pumped Lasing from Hybrid Perovskite Light-Emitting Diodes." Advanced Optical Materials 8.1 (2020): 1901297.

Researcher: **Jesus Manuel Maldonado Vazquez**
Advisor: **Kaushik Sengupta (ELE)**
Sponsorship: **MURI**

Ingestible sensors have revolutionized the standard of care for a variety of health conditions. The main objective of this project is to develop a capsule, with electrochemical sensing technique, which can travel through the GI tract. The ingestible sensor would be used to measure several toxins secretion from the gut microbiome with an accuracy analysis. This ingestible electronic sensor could potentially be a new opportunity for early detection and monitoring of microbiome biomarkers associated with several diseases.
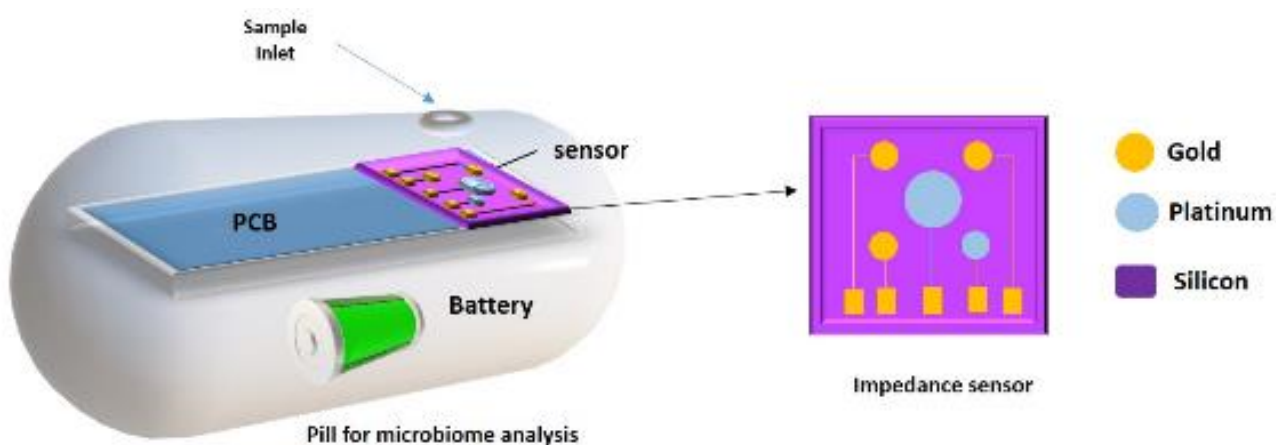
Figure 1: Scheme of the ingestible electronic pill for microbiome analysis and the impedance biosensor.
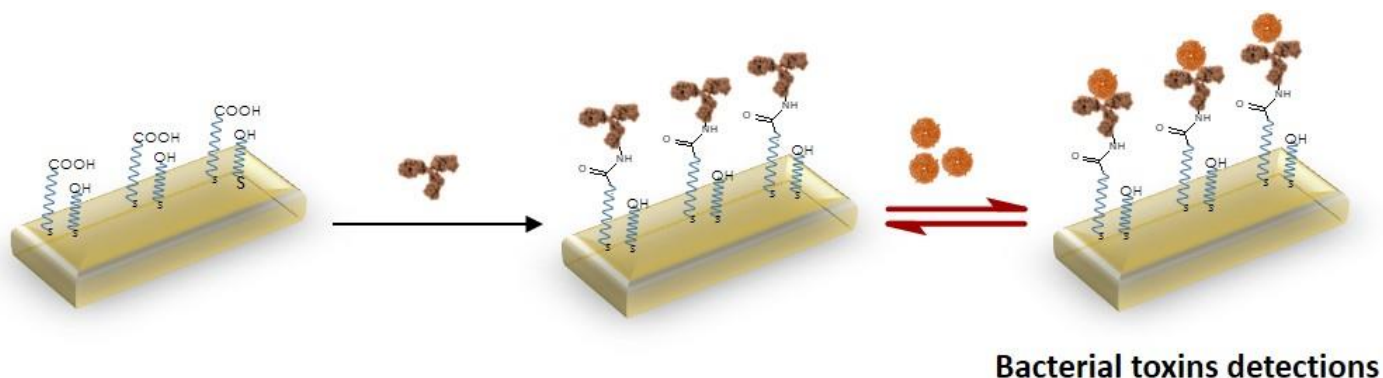
Figure 2: Schematic representation of the biofunctionalization strategy for multiplexed biomolecules immobilization.

CITATIONS

➢ New project

Researcher: **Hao Tang**
Advisor: **Kaushik Sengupta (ELE)**
Sponsorship: **NSF**

The magnetic particle passing through the top surface of surface inductors will influence the oscillating current inside the inductor. This current change is equivalent to the value change of inductors, which will influence the oscillator frequency. This variation of oscillator frequency will be a powerful sensing tool. We hope it can be used to the potential rare cell sensing.
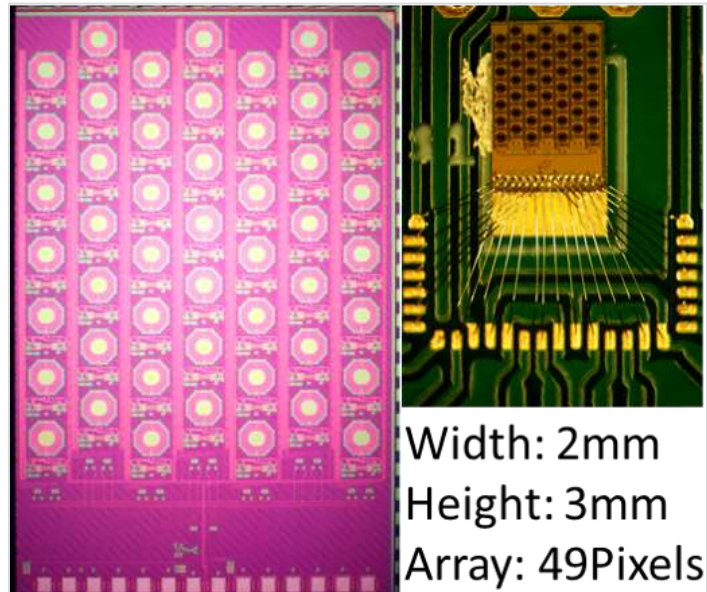
Figure 1
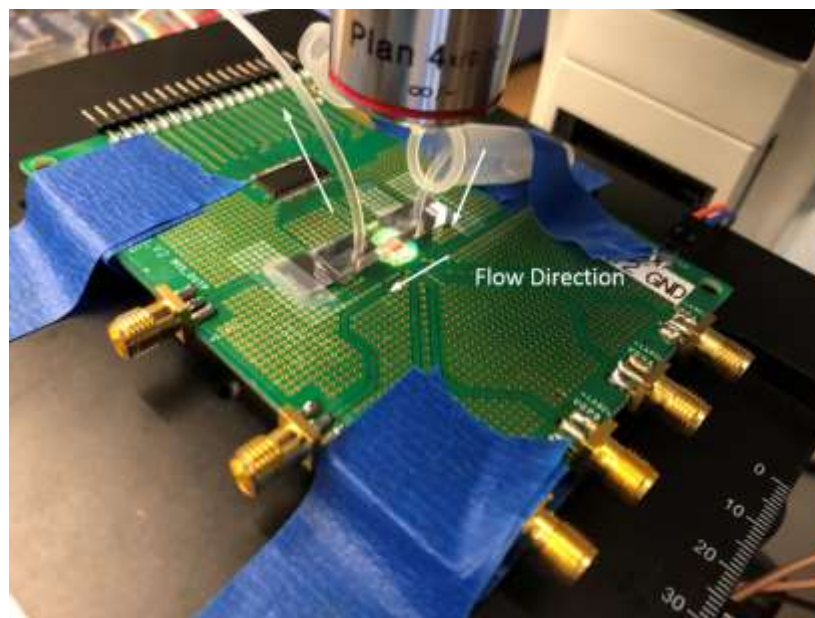
Figure 2

CITATIONS

➤ Princeton University

Researcher: **Suresh Venkatesh and Xuyang Lu**
Advisor: **Kaushik Sengupta (ELE)**
Sponsorship: **Multi-University Research Initiative, AFOSR**

Spatio-temporal modulation of transmitter chains for secure communication and beam steering.

The idea of a secure directional wireless link between a TX/RX pair is to preserve the signal information within a secure cone where the intended receiver is located while scrambling signals everywhere else to prevent eavesdropping. In a phased array, the same temporal digital information is fed to all the TX elements, transmitting the same information to all directions albeit at different power levels. This information can be recovered (especially at the side lobes) with a sensitive enough receiver. Spatial modulation with I, Q radiated out through separate antennas, and modulation of parasitic elements can distort the constellation in other directions. However, this one to-one (bijective) mapping allows potential decoding by the eavesdropper, particularly using various signal processing and machine-learning-based classification techniques. Time modulation in an antenna array can incorporate such physical layer security through careful mapping of symbols to antennas in a time-modulated fashion.

We present a spatio-temporal modulated mm-wave TX array architecture across 71 to 76GHz and demonstrate 1) preservation of signal fidelity at the intended direction in a secure cone, scrambling of the constellation and one-to-many mapping in a 2-element array, 2) narrowing of the secure cone in a 4-element array, 3) reconfiguration of the secure angular zone depending on the intended RX and eavesdropper location, and 4) a chirping modulation scheme that creates a time-varying constellation at the eavesdropper to overcome machine learning and compressive-sensing-based attacks. The paper importantly demonstrates the feasibility of realizing Time-Modulated Arrays (TMAs) in silicon.
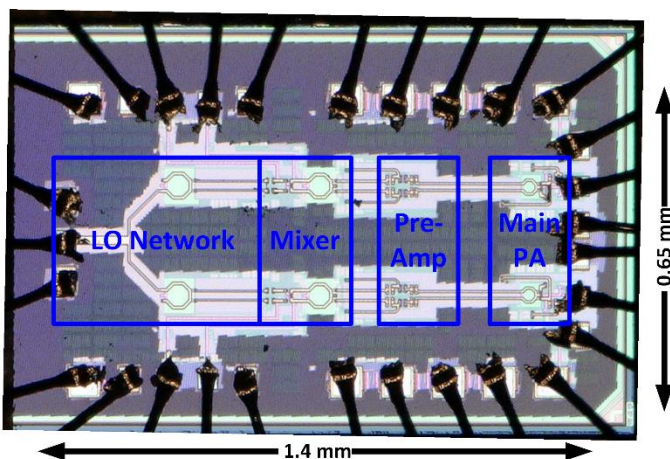
Figure 1: Shows the die micrograph of the time modulated phased array.
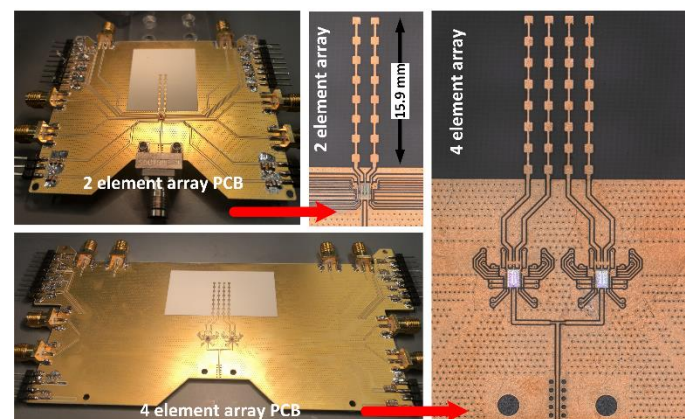
Figure 2: Shows the two element and four element time modulated array along with the integrated CMOS chips and printed circuit boards.

CITATIONS

➢ Space-Time Modulated 71-to-76GHz mm-Wave Transmitter Array for Physically Secure Directional Wireless Links, ISSCC 2020.

Researcher: **Chengjie Zhu**
Advisor: **Kaushik Sengupta (ELE)**
Sponsorship: **NSF**

Ingestible electronics capable of laboratory quality bio-molecular analysis occupying pill-sized volume, operating at sub-mW with a robust wireless interface can transform medical diagnostics and personalized healthcare. Miniaturization of complex bio-molecular systems in such a volume is extremely challenging, notwithstanding a wireless interface that is capable of robust communication through inches of tissue. The paper presents a fully packaged biosensor array with on-chip nanoplasmonic optical filters. The IC, operating across multiple ISM/MICS bands, employs pulse-pause-encoded ASK/OOK modulation and achieves reception energy efficiency of 28 pJ/bit at 7 Mbps and -58 dBm of sensitivity with 196 W of DC power. The entire bio-compatible package is miniaturized to a size of 1.2- 2.5 cm^2. To the best of the authors knowledge, this work demonstrates for the first time a CMOS ICs with pM sensitivity in protein/DNA assays with wireless transmission capability through inches of tissue at state-of-the-art energy efficiency.
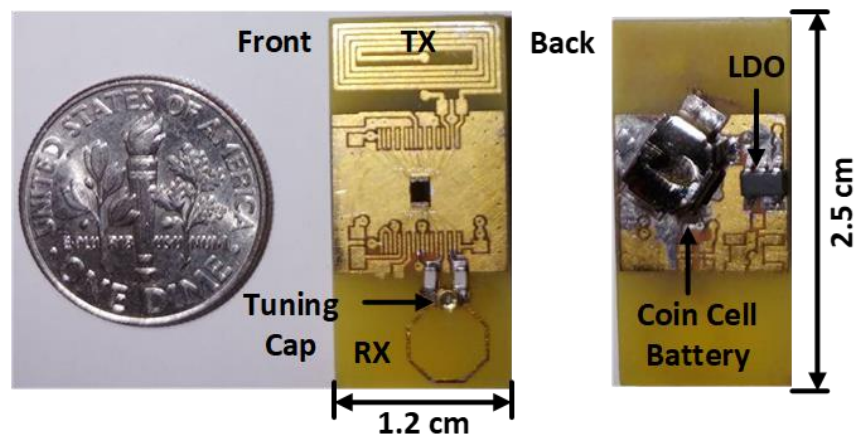
Figure 1: Packaged pill-sized wireless bio-sensing pill with on-chip fluorescence bio-sensor array and wireless transceiver.
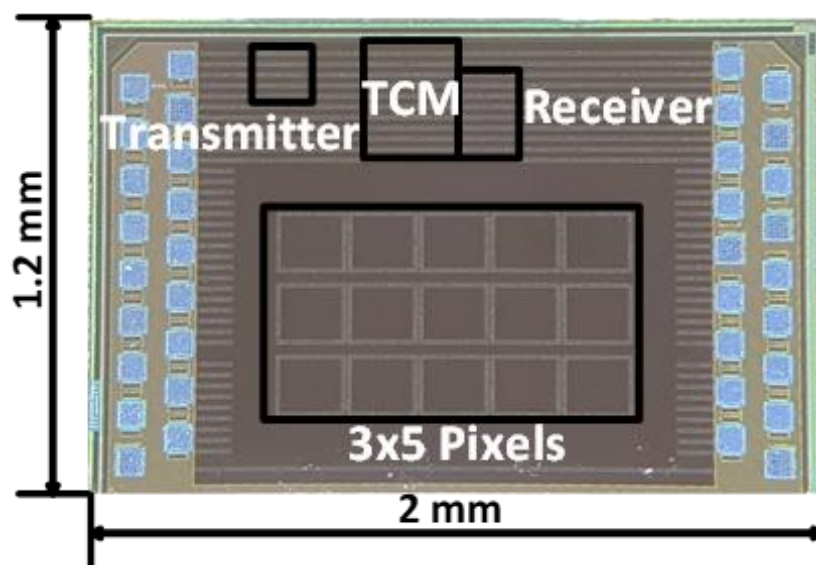
Figure 2: Chip die micrograph showing fluorescence sensing array, transceiver and on-chip digital control block (TCM).

CITATIONS

➢   IMS 2019: Ingestible Bioelectronics: A Packaged, Bio-Molecular, Fluorescence-Based Sensor Array with Ultra- Low-Power Wireless Interface.

Researcher: **Shafayat Hossain**
Advisor: **Mansour Shayegan (ELE)**
Sponsorship: **NSF DMR, DOE, and MRSEC**

Two-dimensional electron systems exposed to high magnetic fields generate emergent quasiparticles, the so-called composite fermions (CFs), whose physics is fundamentally different from electrons. They provide intuitive explanations for different many-body phases such as the fractional quantum Hall effect. One very intriguing CF phase is the metallic phase that occurs in the half- or quarter-filled Landau levels (LLs), the theory of which is still being debated, particularly in the context of particle-hole symmetry and a new Dirac particle theory.

Even though there are numerous experimental studies of the CFs in the half-filled LLs, very few experiments have been performed on CFs near the quarter-filled LL where an electron binds with 4 flux quanta, instead of 2 as in half-filled LLs. Hence, many important questions have remained unanswered: Do 4-flux CFs have properties similar to 2-flux CFs? Do they show a similar asymmetry in the field positions of the GR minima? What happens to the 4-flux CF Fermi sea when the Fermi

sea of the zero-field electrons is highly anisotropic? In our latest work [1], we address all these questions regarding the quarter-filled LL via geometric resonance (GR) measurements which directly probe the Fermi sea and wavevector of CFs. We fabricate a one-dimensional surface superlattice on the sample surface (Fig. 1) that exerts a periodic perturbation to the 2DES, if the CFs can complete a cyclotron orbit ballistically, then they exhibit a GR when their orbit diameter equals the period of the perturbation. Such a resonance provides a direct and quantitative way to explore some of the fundamental properties of CFs. Here, we find that 4-flux CFs are very different from their 2-flux counterparts. They show no asymmetry in the field positions of the GR minima, and their Fermi sea is less affected by the anisotropy in the electron Fermi sea. Most surprisingly, the CFs on the two sides of the quarter-filled LL respond differently (Fig.2) in the presence of Fermi sea anisotropy induced by a parallel magnetic field, and they suggest very different effective masses in the LL filling factor ranges $\nu > \frac{1}{4}$ and $\nu < \frac{1}{4}$.
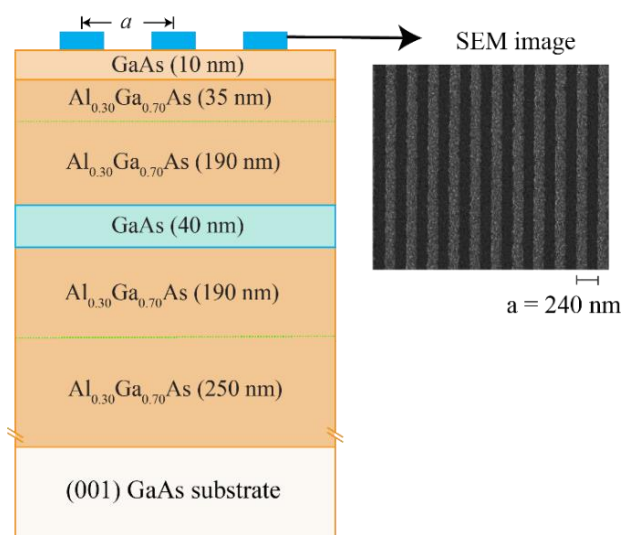
Figure 1: The structure of the studied high quality GaAs quantum well sample that hosts a good quality 2DES which supports the ballistic transport of composite fermions. The scanning electron microscope micrograph of a 240-nm-patterned section attests to the uniformity of the stripes in the superlattice.
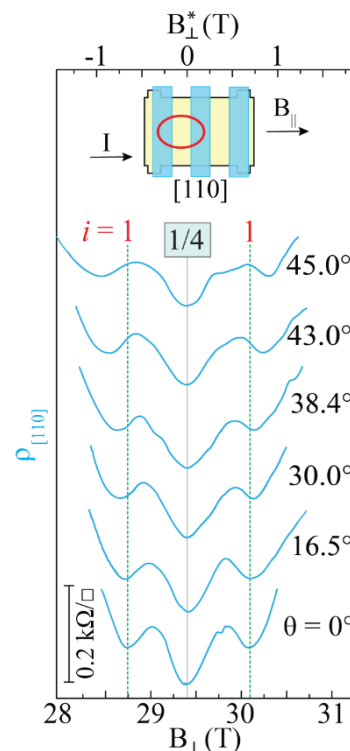
Figure 2: Tilt evolution of the 4-flux CF GR features near $\nu = \frac{1}{4}$. The expected positions for the primary CF GR features are marked with vertical dotted lines.

CITATIONS

1.   **Md. S. Hossain**, M. K. Ma, M. A. Mueed, D. Kamburov, L. N. Pfeiffer, K. W. West, K. W. Baldwin, R. Winkler, and M. Shayegan, Geometric resonance of four-flux composite fermions, *Phys. Rev. B* **100**, 041112(R) (2019).

Researcher: **Meng Ma**
Advisor: **Mansour Shayegan (ELE)**
Sponsorship: **DOE, NSF & MRSEC**

Electrons confined to GaAs quantum wells grown by Molecular Beam epitaxy are known to have very high quality and mobility. At very low temperature the electron mean free path can be of the order of micrometers. Because of such high quality and long mean free path, electrons can be described as classical free electrons and we are able to study its ballistic motion under magnetic field.

In this experiment, we put permalloy (Py) stripes across the Hall bar mesa with different periods. These Py strips give magnetic modulation to the electrons in the quantum well and in the <100> direction the electrostatic modulation is supposed to be minimized. Under magnetic field, the electrons move ballistically in a cyclotron motion. When the cyclotron diameter becomes commensurate with the Py modulation period, the magnetoresistance trace shows a local minimum. Figure 2 below shows a typical magnetoresistance trace which matches the magnetic commensurability modulation behavior.

Figure 1: Microscope image of a GaAs quantum well sample etched to a Hall bar mesa geometry. The Hall bar mesas are along the <100> and <010> directions which is 45 degrees with respect to the cleave direction. In this direction, the electrostatic modulation of the stripes is supposed to be minimized compared to the cleave direction (i.e. <110> and <010> direction) and the magnetic modulation is supposed to be unaffected.

Figure 2: The longitudinal magnetoresistance of the sample (R_{xx}) vs. magnetic field (B) trace measured at 300 mK. The Py stripe modulation period is 800 nm. The green mark indicates the expected positions of the commensurability oscillation minima positions as a result of electrostatic modulation and the black mark indicated the expected minima positions for magnetic modulation. It is clear that the oscillations are consistent with the magnetic modulation.

CITATIONS

➢ Study in progress

Researcher: **Pranav Thekke Madathil and Siddharth Singh**
Advisor: **Mansour Shayegan (ELE)**
Sponsorship: **Gordon and Betty Moore Foundation**

In selectively-doped semiconductor structures, the electrons are spatially separated from the dopant atoms to reduce scattering by the ionized impurities. Thanks to the reduced disorder and scattering, such clean structures provide nearly ideal systems for studies of electron- electron interaction phenomena, especially at low temperatures and high magnetic fields where the thermal and kinetic energies of the electrons are quenched. The dominant electron interaction leads to various fascinating and exotic ground states that are often unexpected. Studies of such states are at the forefront of condensed matter research. They could lead to a better fundamental understanding of interaction phenomena, and they might help advance new concepts such as topological quantum computing. We experimentally investigate electron interaction physics in high-quality, quantum-confined semiconductor structures. The program will include studies of the electronic transport properties at low temperatures and high magnetic fields where electron correlation phenomena dominate. The emphasis of the work will be on several systems, including high-quality two-dimensional electron systems (2DESs) confined to selectively-doped AlAs quantum wells (QWs), and electron and hole systems confined to wide or to double QWs of GaAs. The 2DESs in AlAs have parameters that are very different from those of the standard 2DESs in GaAs: they have a much larger and anisotropic effective mass, a much larger effective g-factor, and they occupy multiple conduction band valleys. The electron or hole systems in wide or double GaAs QWs, on the other hand, possess an additional subband or layer degree of freedom. Both AlAs and bilayer systems provide crucial and important test-beds for new many-body physics. Several exotic phases of these systems will be studied during the course of this project, including the fractional quantum Hall effect (FQHE), composite fermions, Wigner crystal, and stripe phases.
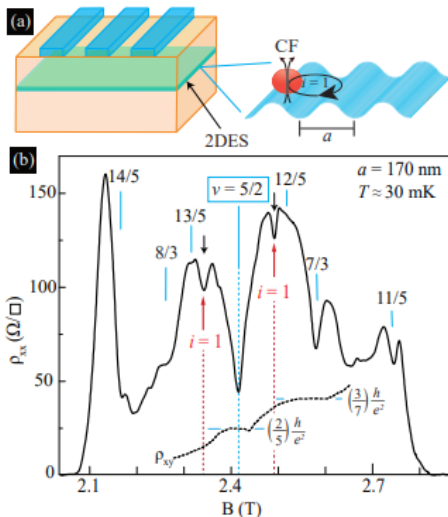
Figure 1: Commensurability oscillations at $\nu = \frac{5}{2}$ proving the existence of a spin polarized fermi sea at $\frac{5}{2}$.
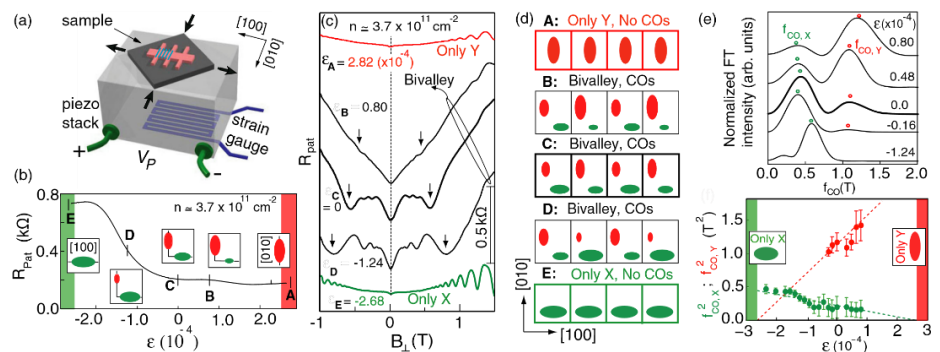
Figure 2: A Valley superlattice realized by selectively changing the valley occupancy through patterned negative e-beam resist stripes

CITATIONS

➢ Md. Shafayat Hossain, Meng K. Ma, M. A. Mueed, L. N. Pfeiffer, K. W. West, K. W. Baldwin, and M. Shayegan, Direct Observation of Composite Fermions and Their Fully-Spin-Polarized Fermi Sea near =5/2, Phys. Rev. Lett. 120, 256601 (2018).

➢ M. A. Mueed, Md. Shafayat Hossain, I. Jo, L. N. Pfeiffer, K. W. West, K. W. Baldwin, and M. Shayegan, Realization of a Valley Superlattice, Phys. Rev. Lett. 121, 036802 (2018).

Researcher: **Kevin Villegas Rosales**
Advisor: **Mansour Shayegan (ELE)**
Sponsorship: **NSF**

Very recently, our research group obtained new high-quality Aluminum Arsenide (AlAs) two-dimensional electron gases. When these samples are immersed in very strong magnetic fields, Coulomb interaction develops new phases of matter such as electron liquids (quantum Hall effect) and electron solids (Wigner crystal). We aim to study the Wigner crystal in these new generation of AlAs samples. Below we show magneto-transport and -capacitance measurement of an AlAs sample of density equal to 3.35×10^{10} cm^{-2}. In Figure 1 we experimentally show two very high resistive peaks in the flanks of the Landau level filling factor 1/3. The fact that the state at 1/3 exists in between two high resistive values experimentally shows that correlations are responsible for this observation. In Figure 2 we corroborate the existence of an insulating phase at the arrow position related to the point "A" in Figure 1.
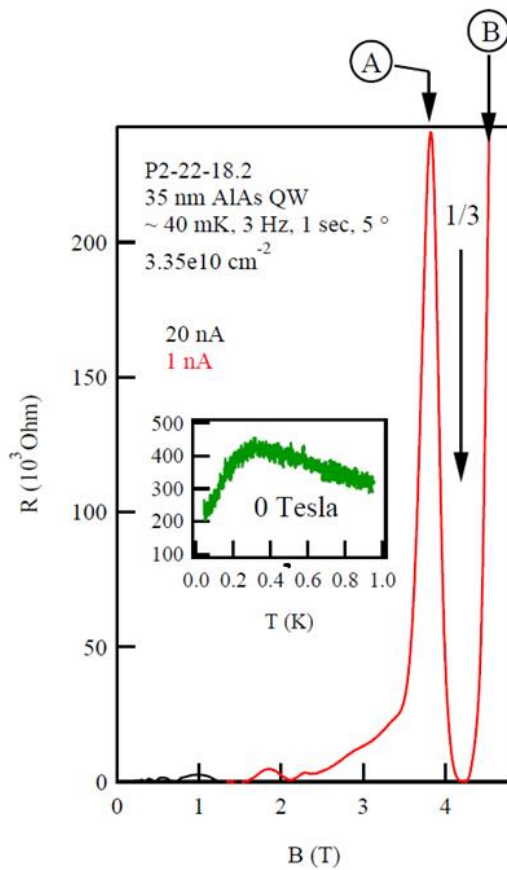
Figure 1: Magneto-transport of our new generation of AlAs samples that shows high resistance values at positions A and B. These positions are commonly related to electron solids.
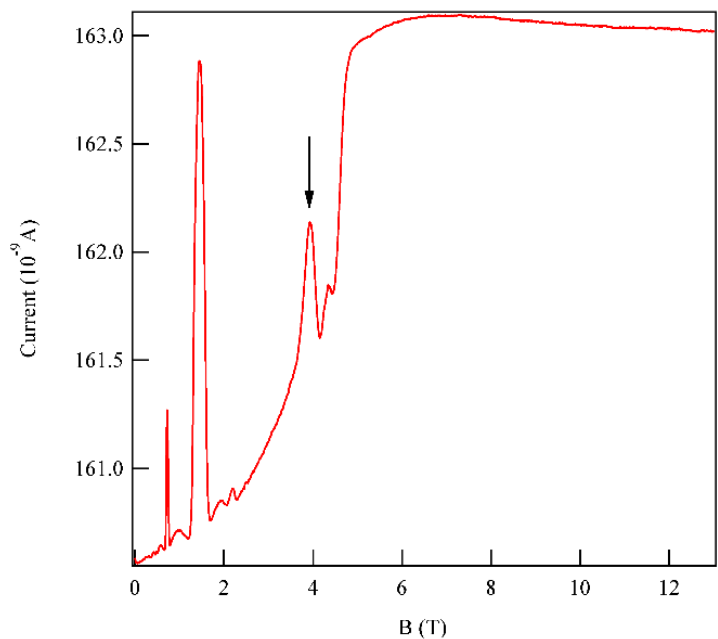
Figure 2: Magneto-capacitance measurements of the same device that shows a peak in current at the electron solid "A" from Figure 1.

CITATIONS

➢ No publications yet

Researcher: **Levent Erdal Aygun**
Advisor: **James C. Sturm (ELE)**
Sponsorship: **James C. Sturm Unrestricted Fund**

Tactile sensing requires form-fitting and dense sensor arrays over large-areas. Hybrid systems, combining Large Area Electronics (LAE) and silicon-CMOS Ics to respectively provide diverse sensing and high-performance computation/control, enable a platform for such sensing. A key challenge is that hybrid systems require a large number of interfaces between the LAE and CMOS domains, particularly as the number of sensors scales. This paper presents an architecture that exploits the attribute of signal sparsity, commonly exhibited in large-scale tactile-sensing applications, to reduce the interfacing complexity to a level set by the sparsity rather than the number of sensors. This enhances scalability compared to sequential-scanning and active-matrix approaches. The architecture implements compressed sensing via thin-film-transistor (TFT) switches, and is demonstrated in a force-sensing system with 20 force sensors, a TFT die (with 161 ZnO TFTs) per sensor, and a custom CMOS IC for system readout and control. Acquisition error of 0.7 k RMS is achieved over a 100k -15k sensing range, at energy and rate of 1.2J/frame and 31 fps.
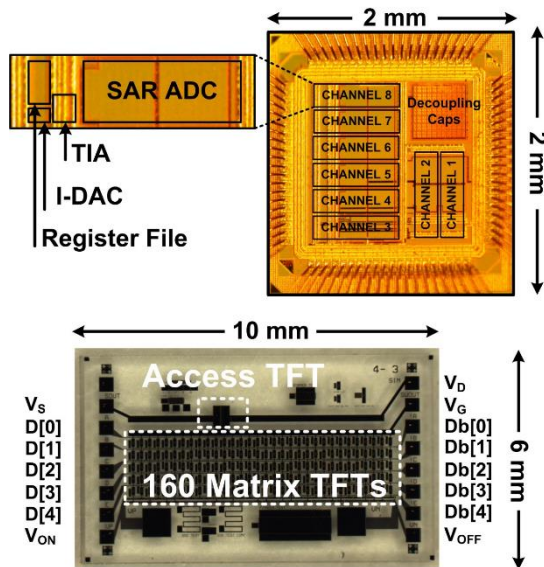
Figure 1: (Top) CMOS die photograph with 8 parallel readout channels with TIA, ADC and I-DAC (Global Foundries 130nm). (Bottom) LAE die photograph implementing sensor signal compression using 161 ZnO based TFTs (PRISM Cleanroom).
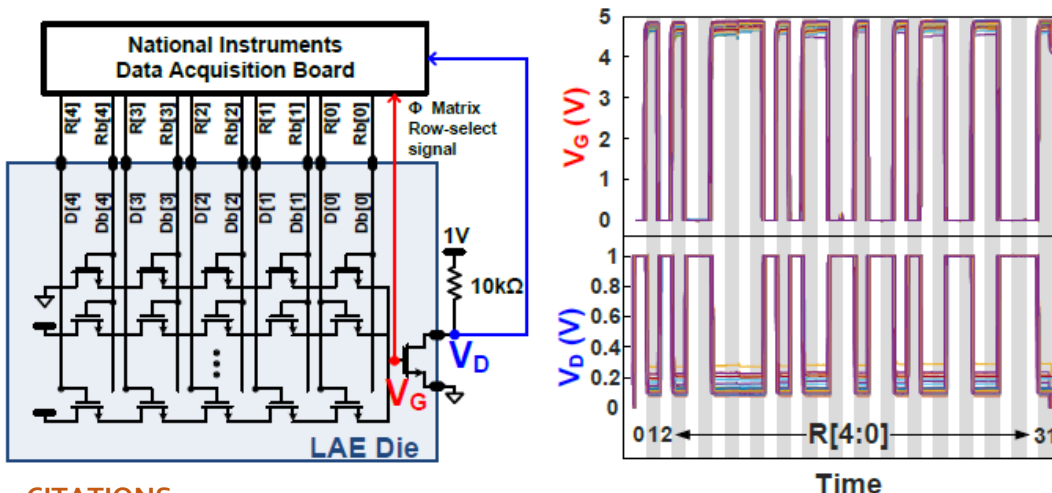
Figure 2: (Left) LAE die test setup where 10kΩ represents thin-film piezoresistive force sensor and 5-bits R codes are applied while access TFT VG and VD monitored. (Right) Measurements from 32 LAE dice show they follow the desired switching pattern with R control codes.

CITATIONS

➢   L. E. Aygun, P. Kumar, Z. Zheng, T.-S. Chen, S. Wagner, J. C. Sturm, and N. Verma, 17.3 Hybrid system for efficient LAE-CMOS interfacing in large-scale tactile-sensing skins via TFT-based compressed sensing, in 2019 IEEE International Solid-State Circuits Conference (ISSCC), IEEE, 2019, pp. 280 282.

Researcher: **Mayalen Brock**
Advisor: **James C. Sturm (ELE)**
Sponsorship: **James C. Sturm Unrestricted Fund**

James Sturm's main goal is to engineer a 3D neural probe. Existing neural probes both damage the brain tissue with their hard metal surfaces and can only be found in 2D (which goes against the nature of actual neurons). To fix this problem, Sturm's lab is trying to engineer a neural probe that is 3D and is flexible and stress free to tissue.
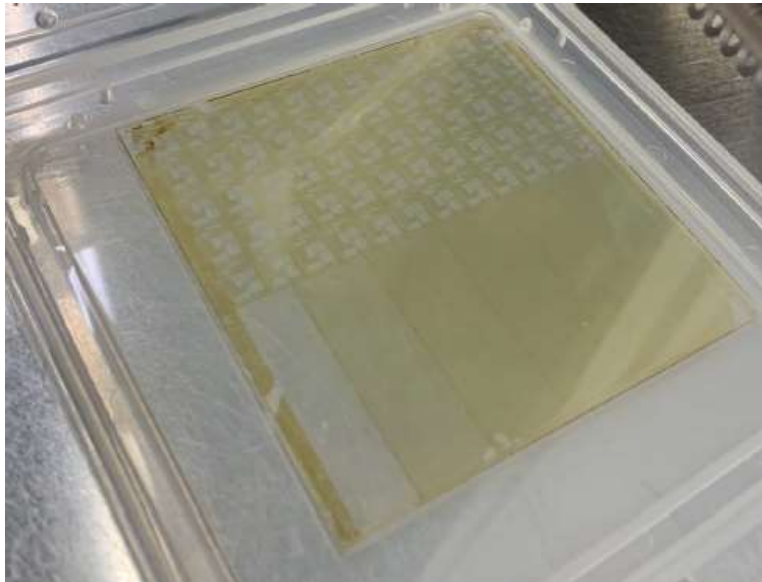
Figure 1: A glass slide with Easybond and cured PI 2611 with different sized etched holes and lines using the PlasmaTherm machine.
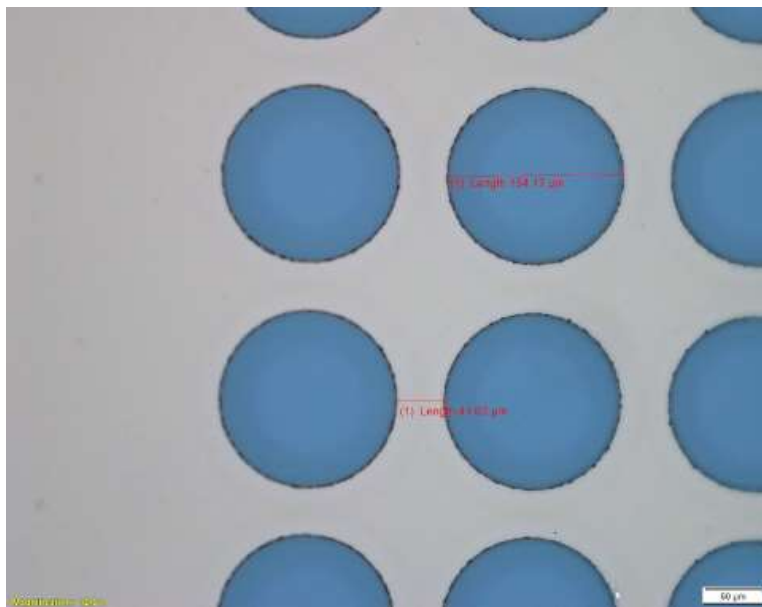
Figure 2: A microscopic view of the holes etched into the cured polyimide.

CITATIONS

➤   Recent work on this project can be found in the senior thesis of Andrew Ge '19 and Matt Wang '19

Researcher: **Michaela Hennebury**
Advisor: **James C. Sturm (ELE)**
Sponsorship: **ELE Department**

My project will focus on developing a process for fabricating TFTs on flexible substrates (polyimide). Previously used methods include fabrication directly onto a polyimide film and fabrication onto a film that is spun onto a wafer. Because the free-standing film expands and contracts during processing, the second method produces TFTs with better performance. However, the removal of the polyimide from the wafer (peeling off) can damage the transistors. I will begin by exploring ways to improve the delamination process, perhaps by using an antiadhesive between the polyimide and the wafer.
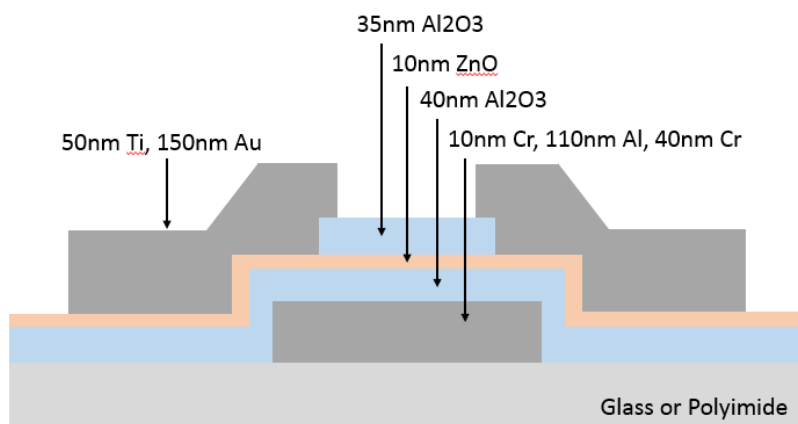
Figure 1: (Left) Schematic of a completed ZnO TFT on a glass or polyimide substrate.
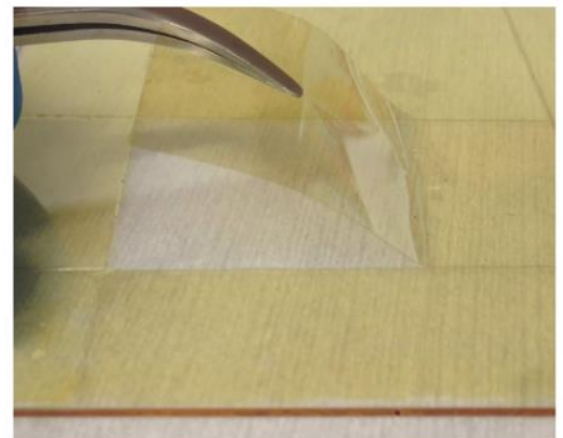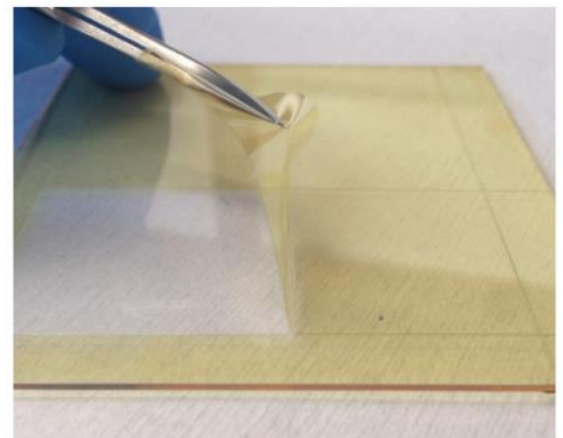
Figure 2: (Right) Delamination peeling angle on untreated glass (top) and glass that has been treated with a self-assembled monolayer antiadhesive.

CITATIONS

  ➢ N/A

Researcher: **Weiguang Huo**
Advisor: **James C. Sturm (ELE)**
Sponsorship: **NSF**

Two-dimensional electron gases (2DEGs) in Si/SiGe heterostructures have been considered as a potential platform to fabricate single electron quantum dots for spin manipulations because silicon has an inherently longer coherence time. The efforts to improve mobility of 2DEGs are the main focus of this project.
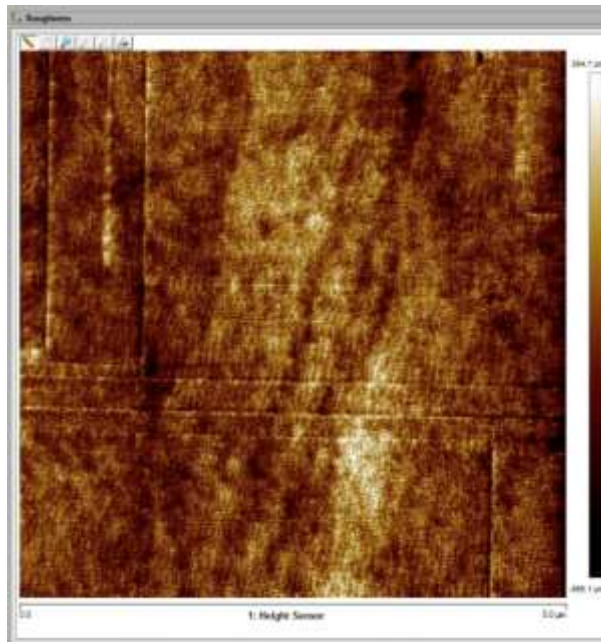
Figure 1: AFM image of 15 nm strained Si layer grown on SiGe virtual substrate. The roughness of Si layer is about 0.15 nm.
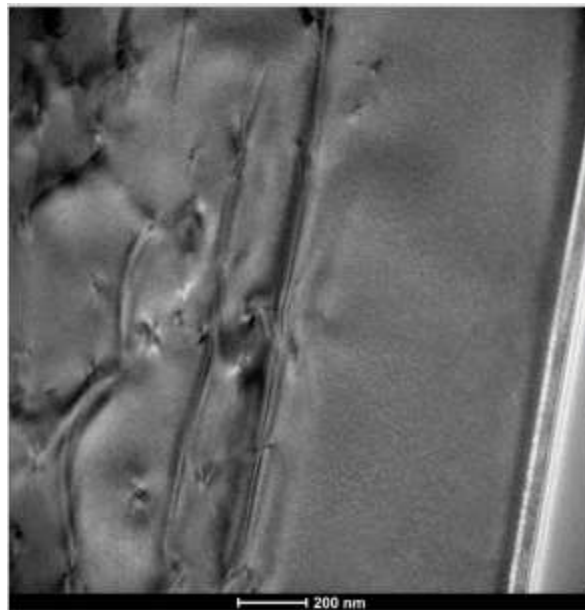
Figure 2: TEM image of SiGe virtual substrate and Si/SiGe heterostructure grown by UHV-CVD.

CITATIONS

➢ Li J Y, Huang C T, Rokhinson L P, et al. Extremely high electron mobility in isotopically-enriched 28Si two-dimensional electron gases grown by chemical vapor deposition[J]. Applied Physics Letters, 2013, 103(16): 162105.
➢ Huang C T, Li J Y, Chou K S, et al. Screening of remote charge scattering sites from the oxide/silicon interface of strained Si two-dimensional electron gases by an intermediate tunable shielding electron layer[J]. Applied Physics Letters, 2014, 104(24): 243510.

Researcher: **Weibin Liang**
Advisor: **James C. Sturm (ELE)**
Sponsorship: **NIH/ GPB STTR**

Etching Si to make molds for PDMS and to directly use to confine fluids which contain cells.

RESULTS
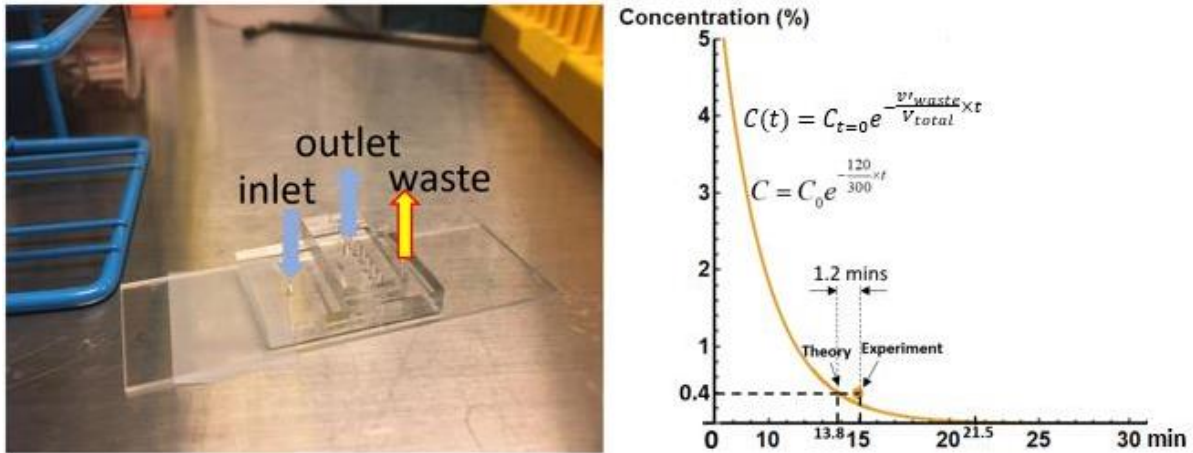
Figure 1: (Left) The PDMS chip integrates 8 individual processing lanes. (Right) Remaining labels (SYTO13) concentration (before process, concentration is 100%) vs processing time.

METHODOLOGY AND EXPERIMENTAL SETUP
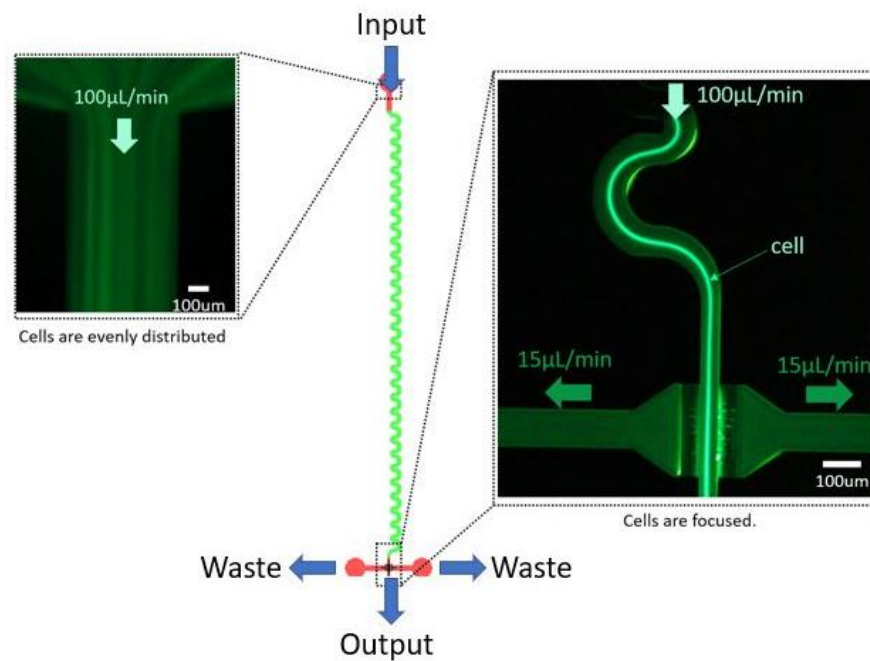
Figure 2: Design of a chip.

CITATIONS

- Microfluidic chemical processing with on-chip washing by deterministic lateral displacement arrays with separator walls. Chen Y, D'Silva J, Austin RH, Sturm JC. Biomicrofluidics. 2015 Sep 9;9(5):054105.
- On-chip cell labelling and washing by capture and release using microfluidic trap arrays. Chen Y, Austin RH, Sturm JC. Biomicrofluidics. 2017 Sep 27;11(5):054107.

Researcher: **Yue Ma**
Advisor: **James C. Sturm (ELE)**
Sponsorship: **NSF**

The tremendous value artificial intelligence (AI) is showing across a broad range of applications is driving it from cyber-systems to systems pervading every aspect of our lives. But real-world data challenges the efficiency and robustness with which AI systems of today can perform, due to the highly dynamic and noisy scenarios they face. While algorithmic solutions are required, this paper also explores technological solutions based on large-scale sensing. Specifically, Large-Area Electronics (LAE) is a technology that can make large-scale, form-fitting sensors possible for broad deployment in our lives. System-design principles, architectural approaches, supporting circuits, and underlying technological concerns surrounding LAE and its use in emerging systems for intelligent sensing are explored.
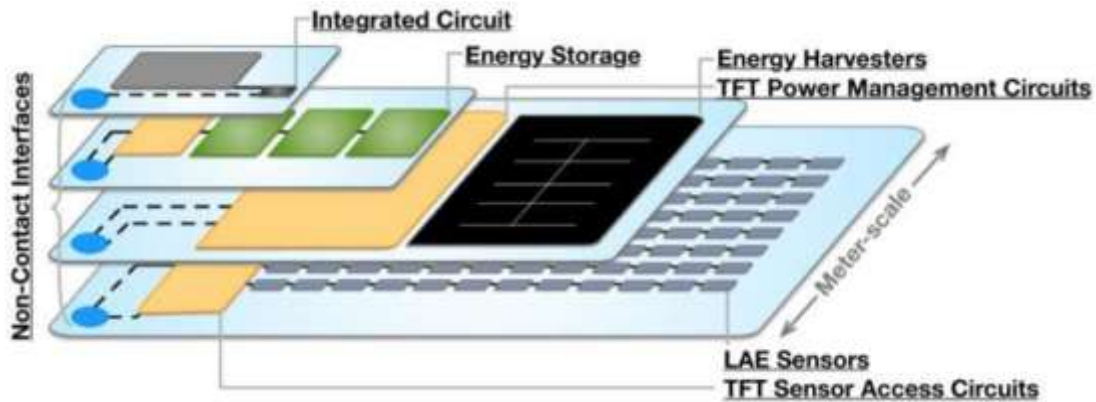
Figure 1: A schematic for hybrid electronic systems based on TFT technology and CMOS technology to utilize the advantages of both.
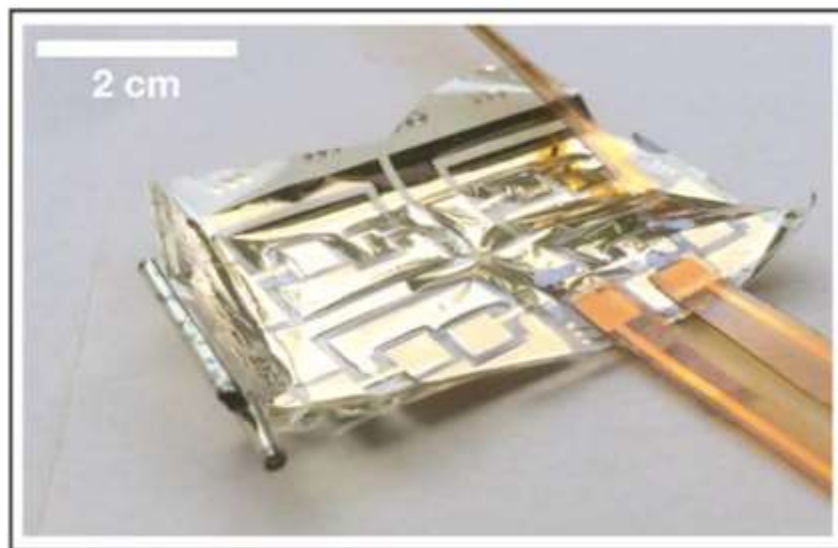
Figure 2: Circuit demonstration with TFTs fabricated on flexible substrates.

CITATIONS

➤ Ozatay M, Aygun L, Jia H, et al. Artificial intelligence meets large-scale sensing: Using Large-Area Electronics (LAE) to enable intelligent spaces[C]//2018 IEEE Custom Integrated Circuits Conference (CICC). IEEE, 2018: 1-8.

Researcher: **Yoni Mehlman**
Advisor: **James C. Sturm (ELE)**
Sponsorship: **PPST**

Large area hybrid electronic systems are a powerful platform for enabling interactions between the microelectronic and meter-scale domains by combining the strengths of large area electronics for sensing and conventional integrated circuits for computation. In such systems, thin-film transistors (TFTs) are needed for instrumentation and communication circuitry integrated with thin-film sensors patterned over large surfaces on the scale of people or large equipment. When integrating transistors with sensors patterned on glass or especially flexible plastic sheets, low process temperatures are required for compatibility with the substrate. Low-temperature processing makes fabrication of high performance devices difficult, so that realizing large sensor systems presents a considerable design challenge. Plasma-enhanced deposition techniques are typically used to improve material and device quality at low process temperatures. My research over the past year has focused on bringing significant improvements to the performance of metal oxide (ZnO) TFTs by scaling of transistor dimensions. This has enabled the highest frequency circuits utilizing metal-oxide TFTs reported in literature.
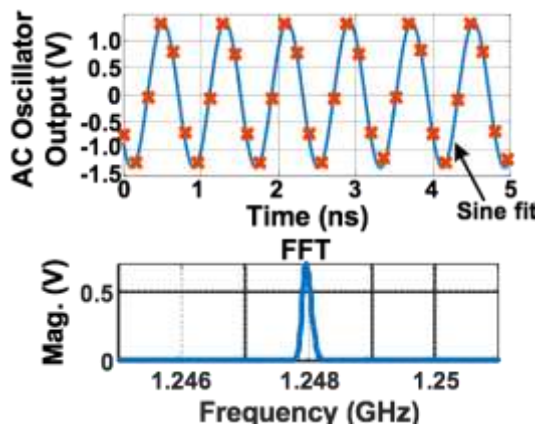
Figure 1: Waveform and corresponding FFT of first-ever gigahertz TFT oscillator.
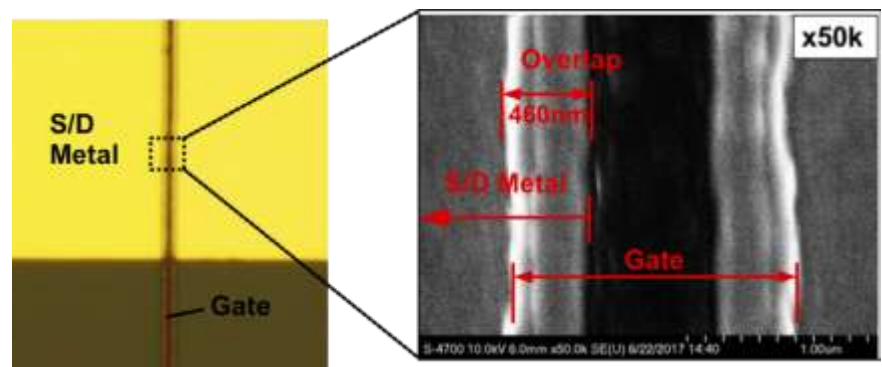
Figure 2: Micrograph and SEM of scaled ZnO TFTs with submicron channel length and source/drain to gate overlaps.

CITATIONS

➢ C. Wu, Y. Mehlman, A. Pierre, T. Moy, A. Arias, and N. Verma, A Large-area Image Sensing and Compression System Based on Variation Tolerant Random Projections, presented at the SONIC Annual Meeting, Champaign, IL, 2015.

➢ Y. Mehlman, Y. Afsar, T. Moy, S. Wagner, J. C. Sturm, and N. Verma, High-Speed Scanning Circuit Based on Metal-Oxide Thin-Film-Transistors for Reduction of Large-Area to CMOS IC Connections, presented at the International Thin Film Transistor Conference, Austin, TX, 2017.

➢ Y. Mehlman, Y. Afsar, T. Moy, S. Wagner, J. C. Sturm, and N. Verma, Self-Aligned ZnO Thin-Film Transistors with 860 MHz ft and 2 GHz fmax for Large-Area Applications, presented at the Device Research Conference, Notre Dame, IN, 2017.

➢ M. Ozatay, L. Aygun, H. Jia, P. Kumar, Y. Mehlman, C. Wu, S. Wagner, J. C. Sturm, and N. Verma, "Artificial Intelligence Meets Large-scale Sensing: using Large-Area- Electronics (LAE) to enable intelligent spaces," presented at IEEE Custom Integrated Circuits Conference, San Diege, CA, 2018. (invited)

➢ 5. Y. Mehlman, P. Kumar, M. Ozatay, S. Wagner, J. C. Sturm, and N. Verma, Large-Area Electronics HF RFID Reader Array for Object-Detecting Smart Surfaces, IEEE Solid-State Circuits Letters, vol. 1, no. 8, p. 182, August, 2018.

➢ 6. Y. Mehlman, C. Wu, S. Wagner, J. C. Sturm, and N. Verma, Gigahertz Zinc-Oxide TFT-Based Oscillators IEEE Device Research Conference, June 2019. (Best Student Paper Award)

Researcher: **Kumar Mritunjay**
Advisor: **James C. Sturm (ELE)**
Sponsorship: **James C. Sturm Unrestricted Fund**

We now can do continuous observations of different cancer cell lines and carry out downstream analysis of cell phenotype as a function of position on the stress landscape. We use this technology to probe adaption and evolution dynamics in prostate cancer cell metapopulations under a stress landscape of a chemotherapeutic drug (docetaxel).
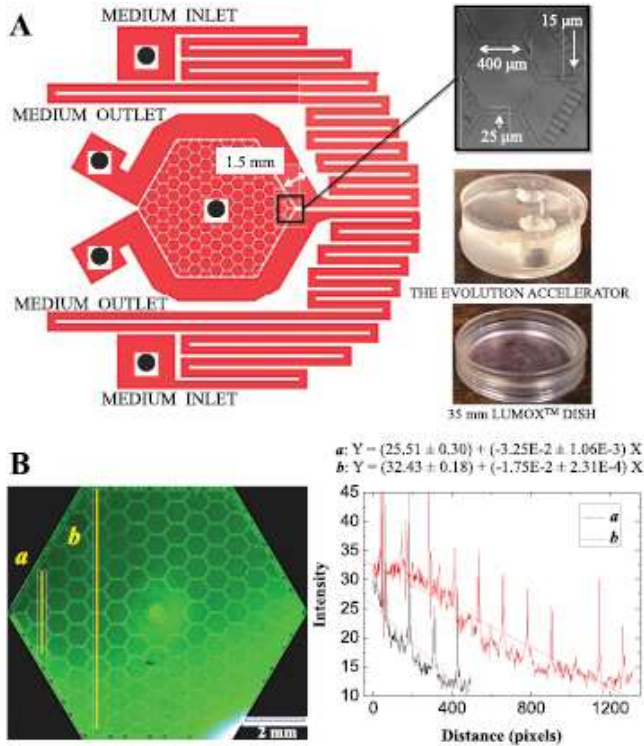
Figure 1: (Left) (A) The microfluidic device has two separate medium inlets, two outlets, and one central port for cell seeding or extraction of excessive medium. (B) The generation of gradient is presented. The syringes pump the medium with ~0.1mM of fluorescein and no fluorescein, respectively, into the chip through the two medium inlets on the right, extracted out from the chip at the two medium outlets on the left. The concentration of fluorescein is proportional to the intensity of fluorescence signal, and is profiled near the medium inlets/outlets a and

Figure 2: (Right) The experimental setup. (A) The PDMS device. From left to right: the patterned layer, the reservoir layer, the capping layer, and the assembled device. (B) The gas supply system. (C) The components of the customized 3 well sample plate. (D) The setup of the experiment, including the gas supply system, gas channels connection, the medium supply connection and the imaging system.
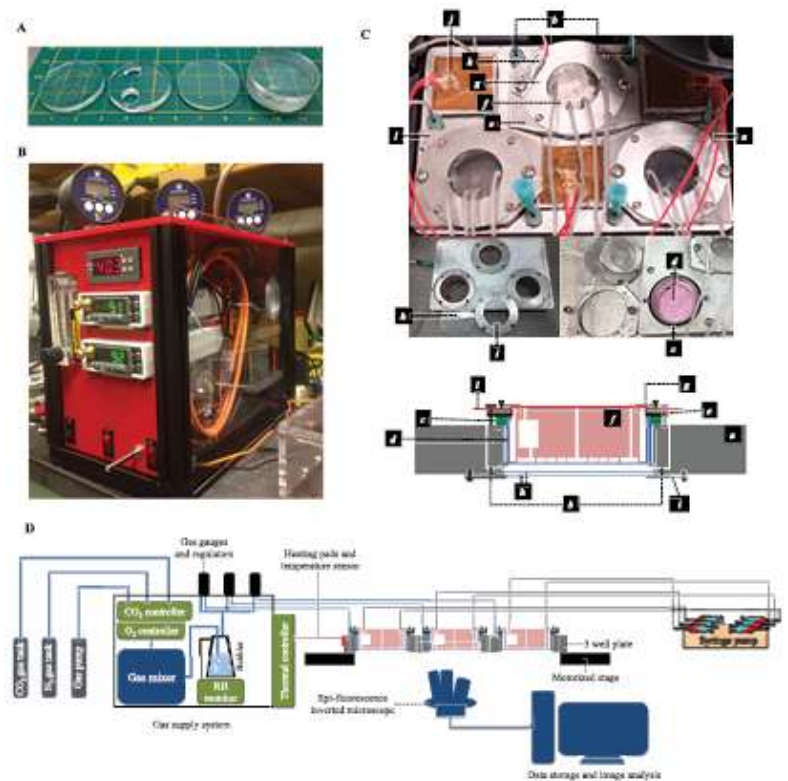
CITATIONS

➢ Epithelial and mesenchymal prostate cancer cell population dynamics on a complex drug landscape.

Researcher: **Can Wu**
Advisor: **James C. Sturm (ELE)**
Sponsorship: **CBRIC**

Encouraged by recent research on GHz Large-Area Electronics (LAE) thin-film transistors (TFTs), we now explore LAE's application in wireless communication at microwave frequency. We have demonstrated two systems: an electromagnetic (EM) phased array and a reconfigurable antenna. The phased-array system takes advantage of large dimension over wavelength offered by LAE technology, which is an important parameter in a radiative aperture as it critically sets the spatial resolution of the radiation pattern. The reconfigurable antenna provides reconfigurability in polarization, frequency and directivity, which optimizes the performance of the antenna for application in different systems. This research represents a forerunner of communication systems with wallpaper form factor, which could be rolled up for transportation and applied to arbitrarily-shaped surfaces.
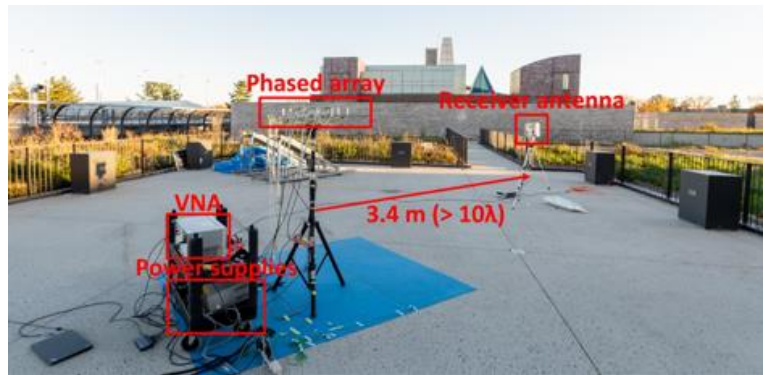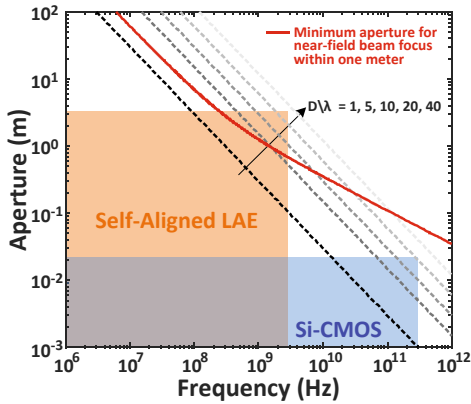
Figure 1: Left: the dimension (aperture) and frequency achievable by LAE and Si-CMOS technology, with labels of different far-field and near-field operation regions. Right: demonstrated LAE-based phased array system.
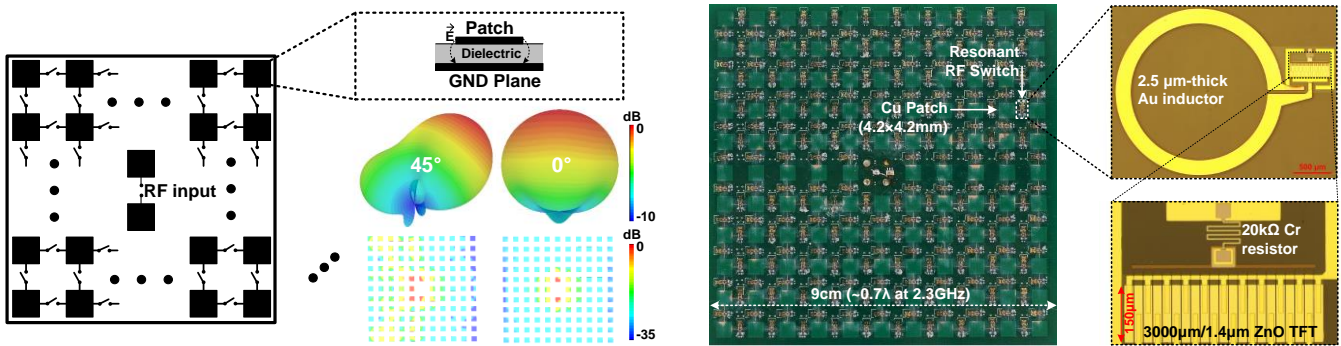
Figure 2: Left: the working principle of the reconfigurable antenna. Right: demonstrated LAE-based reconfigurable antenna system.

CITATIONS

➢ N/A

Researcher: **Zhiwu Zheng**
Advisor: **James C. Sturm (ELE) and Naveen Verma (ELE)**
Sponsorship: **Princeton Program in PLASMA Science and Technology (PPST), SRC and DARPA**

Tactile sensing has wide-ranging applications, from intelligent surfaces to advanced robotics. Large-area Electronics (LAE), based on low-temp. fabrication (<200 ˚C) on thin films, presents distinct capabilities, due to compatibility with a broad range of materials (enabling diverse transducers), as well as large and flexible substrates and materials-deposition methods (enabling expansive and formfitting sensing arrays). Hybrid systems, combining Large-Area Electronics (LAE) and silicon-CMOS ICs to respectively provide diverse sensing and high-performance computation/control.

A key challenge is that hybrid systems require a large number of interfaces between the LAE and CMOS domains, particularly as the number of sensors scales. This project presents an architecture that exploits the attribute of signal sparsity, to reduce the interfacing complexity to a level set by the sparsity rather than the number of sensors. This enhances scalability compared to sequential-scanning and active-matrix approaches. The architecture implements compressed sensing via thin-film transistor (TFT) switches, and is demonstrated in a force-sensing system that 20 force sensors, a TFT die (with 161 ZnO TFTs) per sensor, and a custom CMOS IC for system readout and control.

In this system, however, the combination of insulating substrates (e.g., glass, plastics), long metal traces for distributed sensors and circuits over large areas, plasma processing and packaging/assembly for hybrid systems makes anomalous breakdown in TFT gate dielectrics a prominent limiter of yield in complex systems. In this work, we identified plasma charging damage and ESD during dicing as process steps severely impairing yield, and showed how to prevent such damage using layout modifications and temporary shorting of connections on key components, to enable high-yield processing and assembly of distributed sensor-acquisition circuits.
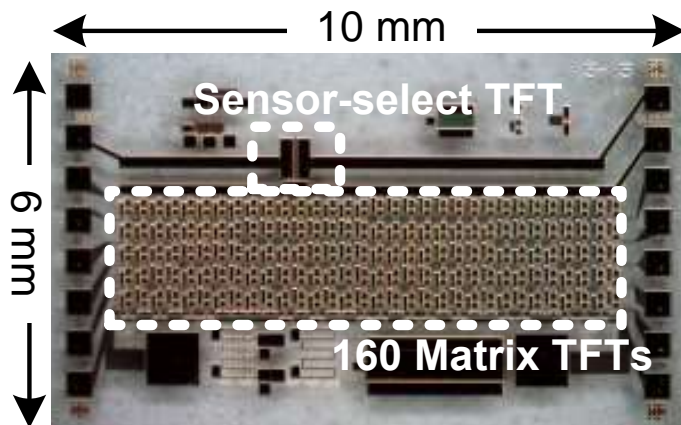
Figure 1: (Left) Die, on glass, of control logic block for selecting sensors and superposing their currents for compressed-sensing acquisition in tactile sensing.

Figure 2: (Right) In-house fabricated evaporated-Cr bottom-gate TFT, with dielectric (Al2O3), channel (ZnO), and passivation layer (Al2O3) deposited by PEALD, followed by evaporated source/drain (S/D) metal. Final interconnect not shown.
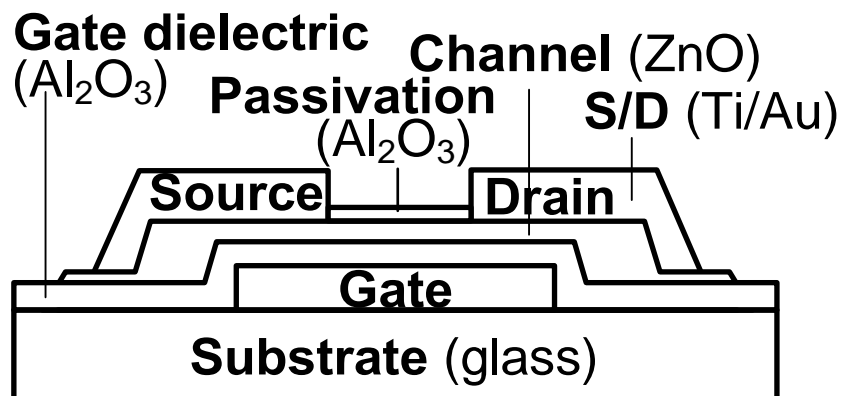
CITATIONS

> L. Aygun*, P. Kumar*, Z. Zheng*, et al. *Proc. ISSCC.,* p. 280 (2019)
> Z. Zheng, *et al. Device Research Conference* (2019).

Researcher: **Songtao Chen and Salim Ourari**
Advisor: **Jeffrey D. Thompson (ELE)**
Sponsorship: **AFOSR**

Single atoms and atom-like defects in solids are ideal quantum light sources and memories for quantum networks. However, most atomic transitions are in the ultraviolet-visible portion of the electromagnetic spectrum, where propagation losses in optical fibers are prohibitively large. We observed for the first time the emission of single photons from a single Er^{3+} ion in a solid-state host, whose optical transition at 1.5 um is in the telecom band, allowing for low-loss propagation in optical fiber. This is enabled by integrating Er^{3+} ions with silicon nanophotonic structures, which results in an enhancement of the photon emission rate by a factor of more than 650 [1]. Recently we have also demonstrated

that modifying the electromagnetic environment using an optical cavity can induce a cycling transition in a solid-state atomic defect, which enables single-shot quantum nondemolition readout of single Er^{3+} ion's electronic spin with 94.6% fidelity [2]. More recently in the PRISM cleanroom, we have developed grating coupler devices (shown in Figure 1 below) for constructing our spin-photon interface. Combined with an angle-polished fiber, the grating coupler devices enable us to realize fiber coupling to single Er^{3+} ions across the whole substrate surface [3]. These results represent a significant step towards long-distance quantum networks and deterministic quantum logic for photons based on a scalable silicon nanophotonics architecture.
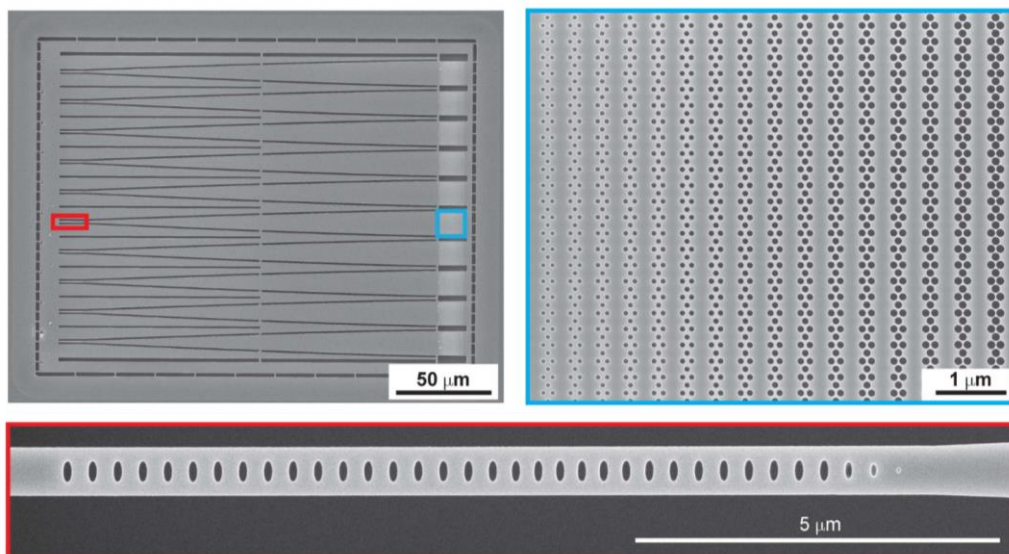
Figure 1: Scanning electron microscope image of the photonic structure on a silicon-on-insulator chip before transferring to the surface of the host crystal with single Er^{3+} ions inside. The in-plane coupling to the 1D nanobeam photonic crystal (red rectangle) is realized by the adiabatic waveguide taper (185 um in length) and the 2D sub-wavelength grating coupler (blue rectangle). The diffracted light from the grating coupler is coupled into an angle-polished single mode fiber hovering on top of the grating coupler. Refractive index modulation of the 2D sub-wavelength grating coupler is realized by tuning hole sizes of the photonic crystal pattern, while the periodicity of the grating is correspondingly apodized to minimize the phase error during the light propagation and diffraction. The profile of index and periodicity apodization is obtained from the FDTD numerical simulation to maximize the diffraction efficiency of light propagating up to the air and mode overlapping with the single mode fiber.

CITATIONS

➤ [1] Dibos, A. M., et al. "Atomic Source of Single Photons in the Telecom Band." Physical Review Letters 120.24 (2018): 243601.
➤ [2] Mouktik, R., et al. "Optical Quantum Nondemolition Measurement of a Solid-State Spin without A Cycling Transition." arXiv:1907.09992 (2019).
➤ [3] Chen, S., et al. "Microwave-Optical Hybrid Scanning Probe for Quantum Information Processing." *in preparation*, (2019).

Researcher: **Christopher Phenicie**
Advisor: **Jeffrey D. Thompson (ELE)**
Sponsorship: **Eric and Wendy Schmidt Transformative Technology Fund**

This project is aimed at identifying new materials as hosts of defects applicable to quantum information. The most widely used defects for quantum information are currently quantum dots and color centers in diamond. The materials used in both of these systems have serious limitations to the wavelength of light used to address the system as well as the coherence properties (and, thus applicability to quantum information) of the spins. One promising candidate to add to this list is the spin associated with erbium defects in solids. These spins in general show excellent coherence and are addressable in the technologically relevant telecommunication wavelength. In the initial stages of this project, I am implanting erbium into various promising host materials, and screening their spin properties with electron spin resonance (ESR) and optical spectroscopy. Using this technique, I should be able to quickly screen the properties of many materials and determine their promise in future quantum information applications.
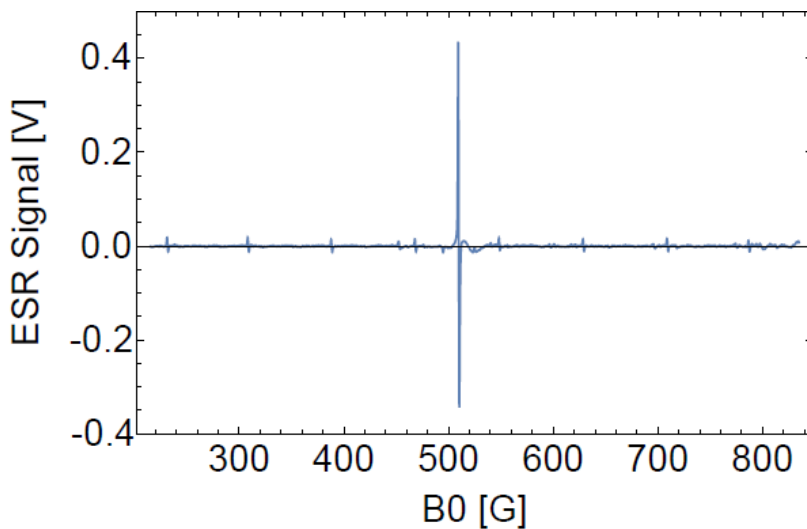
Figure 1: Example electron spin resonance (ESR) spectrum of erbium doped into TiO_2, one of the host materials studied for this project. While the spectrum of a pristine TiO_2 sample show no features at these magnetic fields, this erbium doped sample shows narrow spectral lines. This serves as confirmation of both the incorporation of erbium into the sample as well as the homogeneity with erbium sits in the sample.
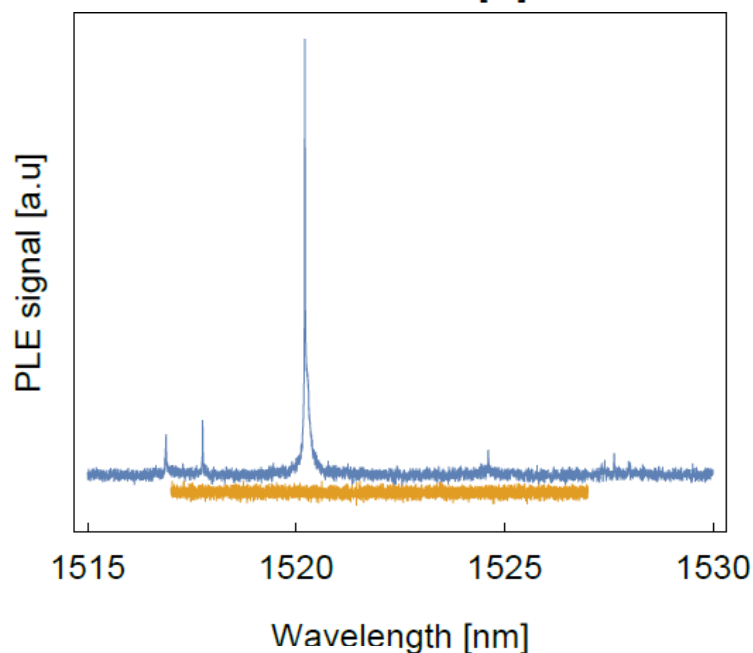
Figure 2: Example photoluminescence excitation (PLE) spectrum of erbium doped into TiO_2. Similar to the ESR data, this spectrum shows no features in a pristine sample. Some lines within the spectrum have linewidth <1GHz, making them some of the narrowest lines ever observed for an optical transition of a defect implanted in a solid.

CITATIONS

➢   C.Phenicie et al, Nano Lett., 19, 12. 8928-8933 (2019).

Researcher: **Jason Liu**
Advisor: **Craig B. Arnold (MAE)**
Sponsorship: **NSF**

Semi-crystalline polymers confined to nanoscale dimensions often crystallize in unexpected ways vastly different from that of bulk crystallization. The crystallization of ultrathin (< 100 nm) films atop solid surfaces is one example, in which the interaction of polymer chains with the underlying substrate is vital in determining the crystallization kinetics and film morphology. Additionally, geometric matching at the molecular scale between the polymer and substrate may induce epitaxial growth. In this work, we deposit ultrathin films of polyethylene oxide atop muscovite mica by aerosol, matrix-assisted pulsed laser evaporation, and other deposition methods. We demonstrate an epitaxial relationship between needle-like polymer crystals and the substrate. Mechanism of nucleation and growth of the epitaxial crystals are discussed.
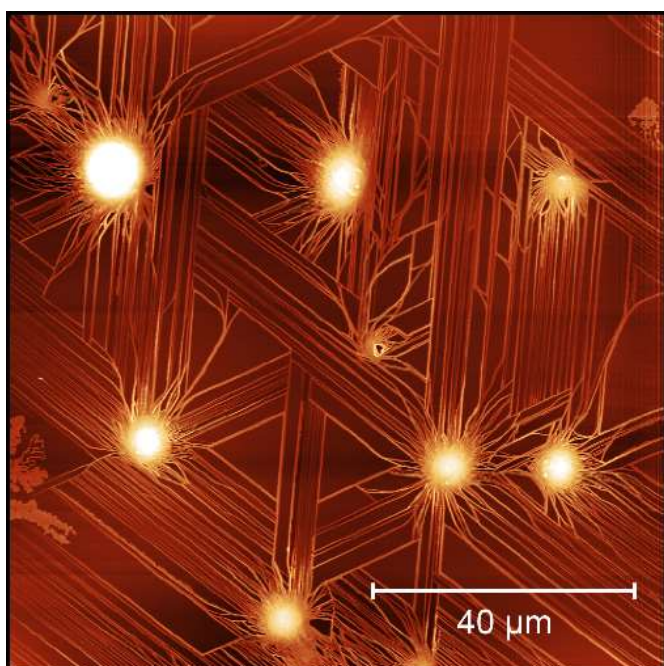
Figure 1: AFM image of PEO needles, 5-10 nm in height, grown epitaxially atop mica by MAPLE.

Figure 2: SEM image of epitaxial PEO crystals aligned over several hundred micrometers.
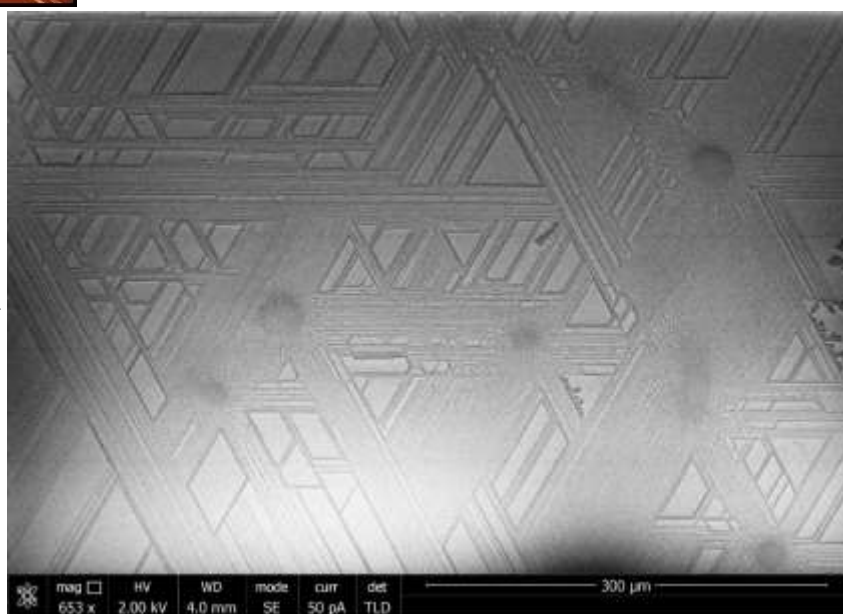
CITATIONS

➤ N/A

Researcher: **Thomas Metke**
Advisor: **Craig B. Arnold (MAE)**
Sponsorship: **NSF**

Printing batteries onto an interdigitated substrate and then applying stress can generate larger voltage and current generation than currently used systems. Thus, larger quantities of energy can be harvested.
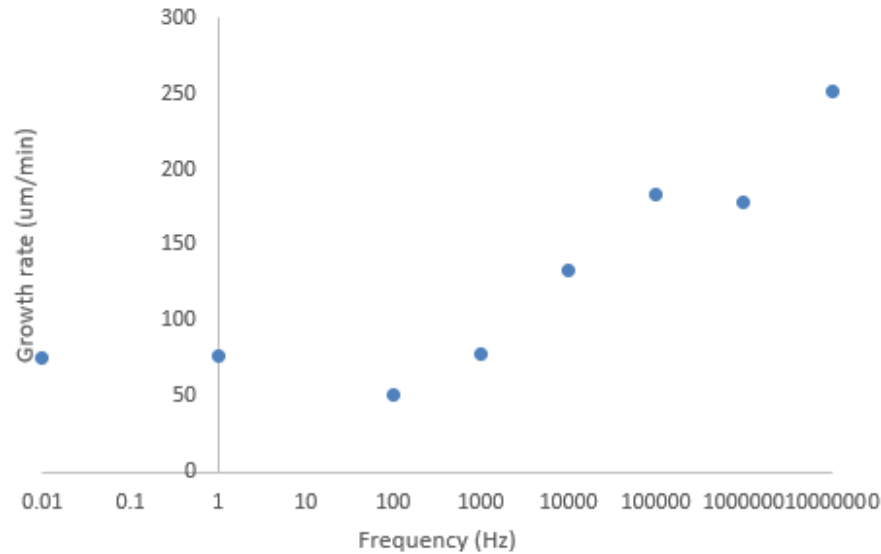
Figure 1
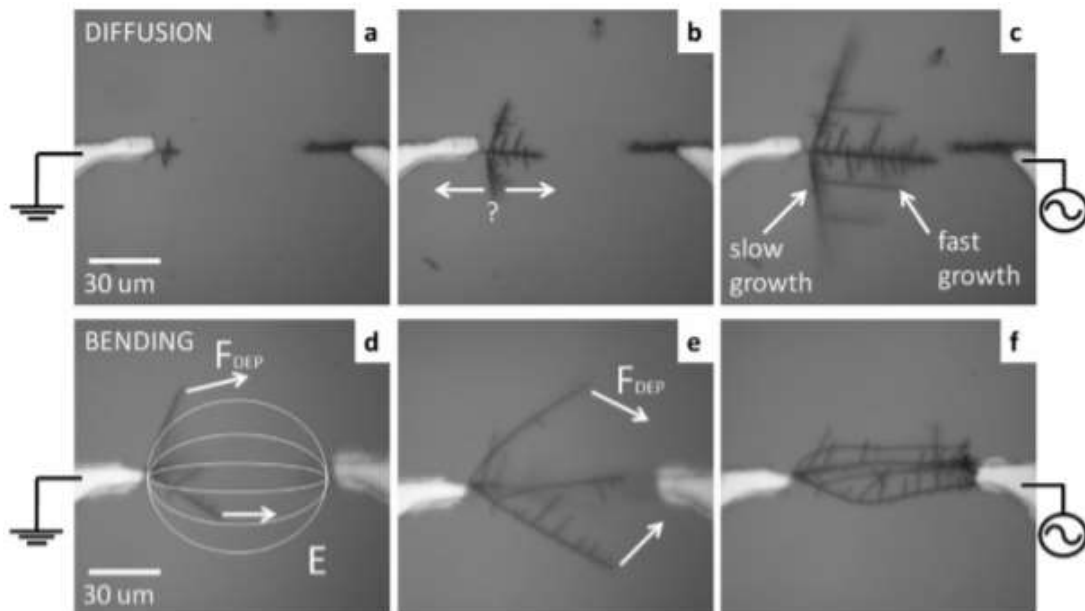
Figure 2: Two mechanisms for directed growth, shown in time lapse images from left to right taken under an optical microscope. (a-c) Anisotropic diffusion growth (12 Vpp at 2 MHz). Side branches emanating from the vertical dendrites grow faster toward the right (toward the electrode gap) than toward the left (away from the electrode gap). (d-f) DEP bending (12 Vpp at 4 MHz). Dielectrophoresis aligns the nanowires with the electric field, thus bending the growing nanowires toward the opposing electrode. The DEP force is more noticeable on the bottom panels than on the top panels because the thinner wires on the bottom (200 nm diameter) are more easily bent than the thicker wires on the top (700 nm diameter).

CITATIONS

➢ N/A

Researcher: **Wenxuan Zhang**
Advisor: **Craig B. Arnold (MAE)**
Sponsorship: **Eric and Wendy Schmidt Transformative Technology Fund**

We propose to develop and construct a novel additive manufacturing platform capable of producing metal objects with verified properties and controlled defects. One of the approaches is to explore the benefits of using reconstructed beam profiles instead of a single Gaussian beam.

Figure 1: Diffractive Element Optics (DOE) on a glass wafer fabricated inside of clean room.
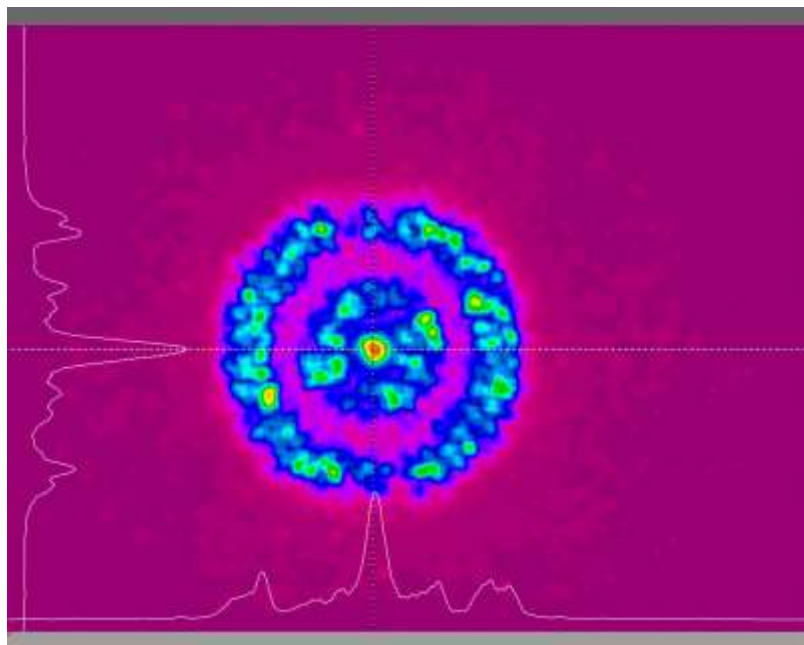
Figure 2: Reconstructed beam energy distribution by DOE, measured by a beam profiler.

CITATIONS

➢   N/A

Researcher: **Yuyang Fan**
Advisor: **Marcus N. Hultmark (MAE)**
Sponsorship: **Princeton IP Accelerator Fund**

We introduce a novel, strain-based sensor for both gaseous and liquid flows, named the Elastic Filament Velocimetry probe. The sensor consists of a free-standing, electrically conductive, nanoscale ribbon suspended between silicon supports. Due to its size, the nanoribbon deflects in flow under viscously dominated fluid forcing, which induces axial strain and a resistance change in the sensing element. The change in resistance can then be measured by a Wheatstone bridge, resulting in straightforward design and operation of the sensor. Since its operating principle is based on viscous fluid forcing, the sensor has high sensitivity especially in liquid or other highly viscous flows.
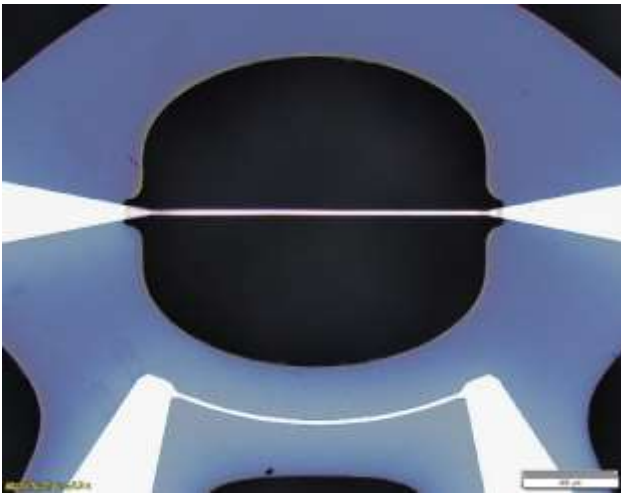
Figure 1: Microscopic image of the platinum freestanding sensing element (center), non-freestanding element (bottom), and plasma-etched flow path hole.
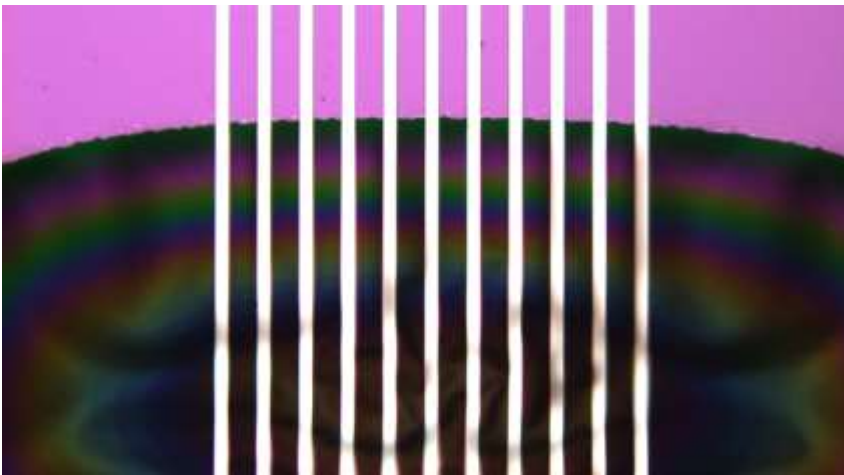
Figure 2: Microscopic image of multiple platinum freestanding sensing elements over the flow path hole.

CITATIONS

➢ Hultmark M, Fan Y, Byers CP, Fu MK, System and Method for Monitoring Injection Site Pressure 2018 International Patent Application PCT/US2018/19142, February 22, 2018.
➢ Hultmark M, Fan Y, Byers CP, Fu MK, Multi-component Fast-response Velocity Sensor 2018 International Patent Application PCT/US2018/18147, February 14, 2018.
➢ Hultmark M, Byers CP, Fu MK, Fan Y, Elastic Filament Velocimetry Sensor 2016 International Patent Application PCT/US2016/40975, July 5, 2016.
➢ Byers CP, Fu MK, Fan Y, Hultmark M (2018) Development of Instrumentation for Measurements of Two Components of Velocity with A Single Sensing Element, Measurement Science and Technology, 29(2), 025304.
➢ Fu MK, Fan Y, Byers CP, Chen T-H, Arnolds CB, Hultmark M (2016) Elastic Filament Velocimetry, Measurement Science and Technology, 28(2), 025301.

Researcher: **Kelly Huang**
Advisor: **Marcus N. Hultmark (MAE)**
Sponsorship: **NSF**

My current project aims to characterize local, near-surface, fluxes at different temporal and spatial scales and relate them to flow and surface associated variables. The Nano-Scale Thermal Anemometer Probes (NSTAPs) will be used to measure turbulence variables of velocity, temperature and humidity at unprecedented temporal and spatial resolutions.
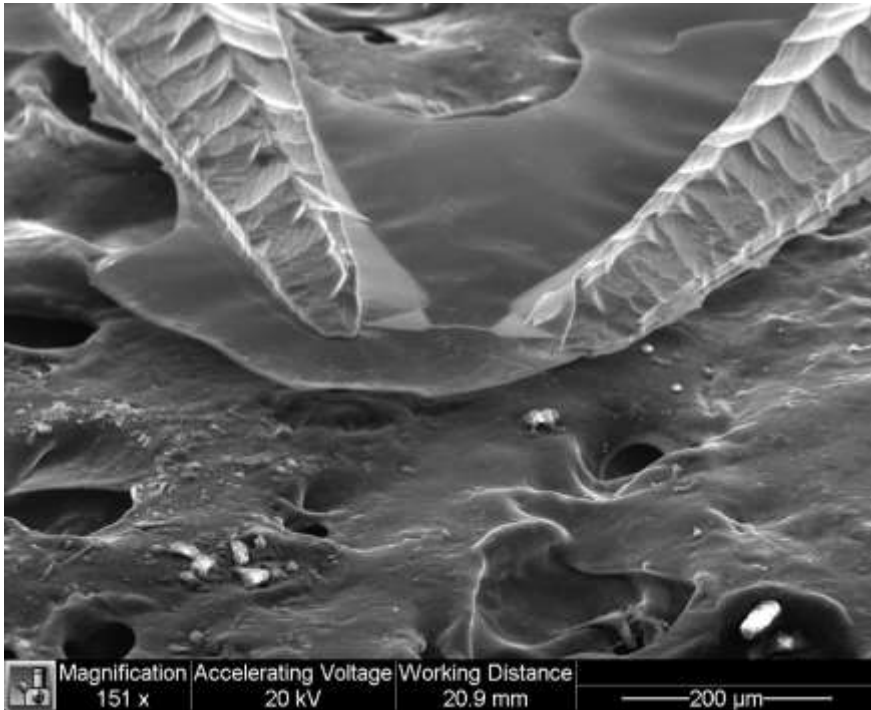
Figure 1: The tip of the NSTAP. The wire (suspended at the tip of the silicon structures) has dimensions of 60 microns x 6 microns x 120nm.

Figure 2: One station of the set-up deployed at Utah's SLTEST facility. An NSTAP, a TNSTAP, a pitot tube, and a thermocouple are mounted.

CITATIONS

➢ N/A

Researcher: **Jovana Kondic**
Advisor: **Marcus N. Hultmark (MAE)**
Sponsorship: **Princeton ELE Department**

The aim of this sophomore independent work is to explore a novel method of determining fluid viscosity through signal analysis by building up on the previous summer research program that involved understanding the principles of Elastic Filament Velocimetry. The understanding and measurement of viscosity plays an important role in modern medicine. Strict measure and control of viscosity is a necessity in the development of various pharmaceuticals and plays a critical role in proper delivery of the drug to the target. Furthermore, viscosity of blood is influenced by changes in vascular architecture and the ability to measure it helps in the diagnosis of anemia, stickle cell disease, and a number of acute cardiovascular events. Due to scarcity of newly proposed techniques, whole blood viscosity is conventionally measured using a Brookfield viscometer, an old technology primarily designed for measuring the viscosity of house paint or engine oil. Elastic Filament Velocimetry (EFV) technology was developed in the Fundamental and Applied Studies in turbulence Laboratory and relies on a freestanding electrically conductive nano-ribbon that is fixed at both ends. When the passing fluid flow elongates the wire, the forces exerted on the wire due to strain can be measured as a resistance change via a strain gauge effect. Therefore, for a given wire and fluid, the flow velocity can be directly correlated to the resistance of the wire. If the aspect ratio of the nano-ribbon is kept high (as in its current design where the ratio of length to thickness is 7000), the nano-ribbon can have large deflections compared to its thickness yet maintain very small angles, which allows flow rates as low as 0.5 ml/hour to be detected with very high precision. Moreover, since the cross-section of the nano-ribbon is very small, the forces acting on it are dominated by viscosity. This means that the output signal representing the change in voltage due to the change in resistance of the wire is in fact a function of flow velocity and dynamic viscosity. The goals of this independent work are twofold: first, I will perform signal analysis in order to determine how the output signal relates to the time it takes for the flow to become steady. This will be achieved by varying both the viscosity and the pipe radius and reading the change in resistance of the output signal. Once that is accomplished, I will then attempt to determine the fluid's velocity without knowing its viscosity by making use of the previously acquired results. Moreover, different geometries of nano-ribbons will be designed in Princeton's Micro/Nano Fabrication Laboratory and tested in the experimental setup in order to optimize the aspect ratio of the sensor for viscosity measurements. As with most silicon-based technologies, small size implies low cost. As the sensor is fabricated using semiconductor manufacturing techniques, not only does miniaturization of the product promise increased sensitivity, as it was shown in the primary EFV development, but it would also imply significant cost savings, in hopes of providing a novel technology for viscosity measurement that has both high clinical utility and scalability.
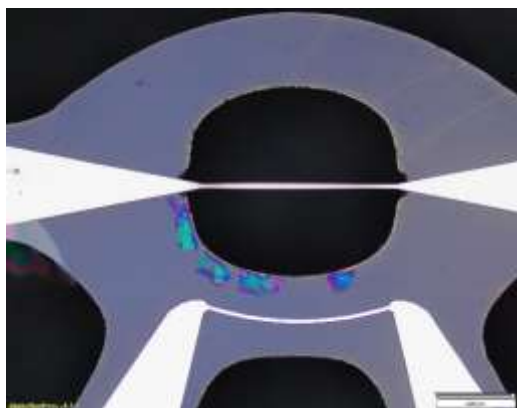

Figure 1: Close-up of the MEMS-based Elastic Filament Velocimetry sensor.
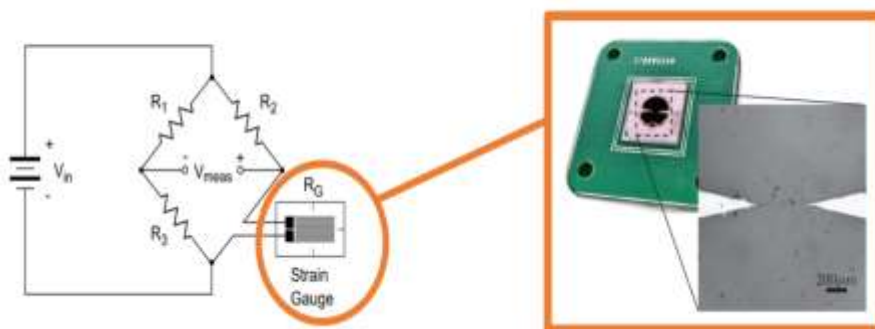

Figure 2: Experimental setup of the EFV as a part of the Wheatstone bridge circuit.

CITATIONS

➢ Fu M., Fan Y., Byers C., Chen T., Arnold C. and Hultmark M., "Elastic Filament Velocimetry", Meas. Sci. Tech, Vol. 28, 025301, 2016.

Researcher: **Alexander Piqué**
Advisor: **Marcus N. Hultmark (MAE)**
Sponsorship: **NSF**

Hot-wire anemometry (HWA) is a common method used for obtaining turbulent flow measurements. However, with increasing Reynolds-number, the temporal and spatial resolution required begins to exceed conventional HWA capabilities. In order to overcome these limitations, the novel Nanoscale Temperature Anemometry Probe (NSTAP) designed by the Hultmark Lab, has been utilized to achieve the temporal and spatial resolutions required. NSTAP fabrication consists of depositions of different materials, photolithography of custom photoresist masks, DRIE combined with RIE lag effect, and BOE etching. These procedures will ensure that the NSTAP is able to have an aerodynamic body shape and support the fragile sensing element. Preliminary wake studies using the NSTAP have been conducted on a model wind turbine exposed to laminar inflow conditions. These studies were conducted for downstream positions of $0.77<x/D<5.52$ and $3e6<Re_D<8e6$ and a tip speed ratio (λ) of 5. In future experiments, the NSTAP will be used in measuring the turbulent flow statistics of wind turbine wakes to provide information for wind farm planning and computational fluid mechanics studies.
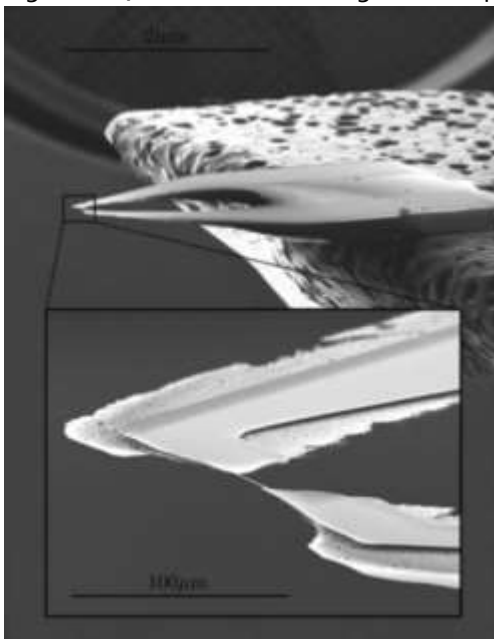
Figure 1: SEM image of the NSTAP before soldering onto a Dantec probe holder (Vallikivi et al., 2011).
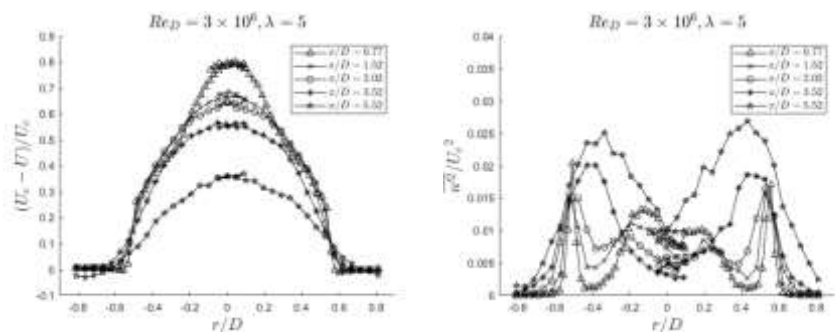
Figure 2: Velocity (left) and turbulent kinetic energy (right) profiles taken at multiple downstream positions of a 3 bladed horizontal axis wind turbine model. These profiles were recorded using an NSTAP probe sampling at 200kHz. The NSTAP's high temporal resolution allows for the resolution of the smallest length scales in the flow.

CITATIONS

➢ Bailey, S. C., Kunkel, G. J., Hultmark, M., Hill, J., Meyer, K., Arnold, C. B. and Smits, A. J., Turbulence measurements using a nanoscale thermal anemometry probe, Journal of Fluid Mechanics. Vol. 663, pp160 179, 2010.

➢ Vallikivi M., Hultmark M., Bailey S.C.C., and Smits A. J., Turbulence measurements in pipe flow using a nano- scale thermal anemometry probe, Experiments in Fluids, Vol. 51, pp. 1521 1527, 2011.

➢ Fan Y., Arwatz G., Van Buren T. W., Hoffman D. E., and Hultmark M., Nanoscale sensing devices for turbulent measurements, Experiments in Fluids, Vol. 56:138, 2015.

➢ Vallikivi M., Hultmark M., and Smits A.J., Turbulent boundary layer statistics at very high Reynolds number, Journal of Fluid Mechanics, Vol. 779, pp. 371-389, 2015.

➢ Arwatz G., Fan Y., Bahri C. and Hultmark M., Development and characterization of a nano-scale temperature probe (T-NSTAP) for turbulent temperature measurement , Meas. Sci. Tech, Vol. 26, 035103, 2015.

➢ Byers C. P., Fu M. K., Fan Y. and Hultmark M., Development of instrumentation for measurements of two components of velocity with a single sensing element , Measurement Science and Technology, Vol. 29, pp. 025304, 2018.

Researcher: **Konstantinos Steiros**
Advisor: **Marcus N. Hultmark (MAE)**
Sponsorship: **NSF, Schmidt Fund**

The SuperTank facility will enable controlled investigations of aerodynamics, forces, power, and wake dynamics on wind turbines and wind farms. Such studies have been referred to as impossible due to the enormous length scales associated with wind turbines, and the challenges of achieving dynamics similarity in laboratory tests. Full dynamic similarity will be achieved by adjusting the density of the fluid by almost two orders of magnitude. The Supertank uses air as working fluid with pressures up to 80 bar, and comprises of an outer tank measuring 2m in inner diameter and 12.7m long, an open return wind tunnel that is contained within the tank, and ancillary diagnostics instrumentation. Large size compressors will pressurize the vessel. In addition to allowing unique studies of wind turbines, the facility will open up unique opportunities to perform fundamental studies of hydro-kinetic turbines, propellers, fans, pumps, and other rotating systems, as well as building and environmental flows, all under full similarity conditions. The SuperTank will be designed to be multipurpose and flexible in its implementation, and will allow NSTAP (see figure 2) and Particle Image Velocimetry measurements. A long list of Princeton faculty members have shown interest in the possibilities of this unique facility.

Compressed-air wind chamber

- Gauge pressures up to 80 bar
  - ρ up to 95 kg/m^3
- Optical access ports for PIV, PTV, LDV...
- $Re_L = 6 \times 10^7 \, m^{-1}$

2.0 m

12.70 m
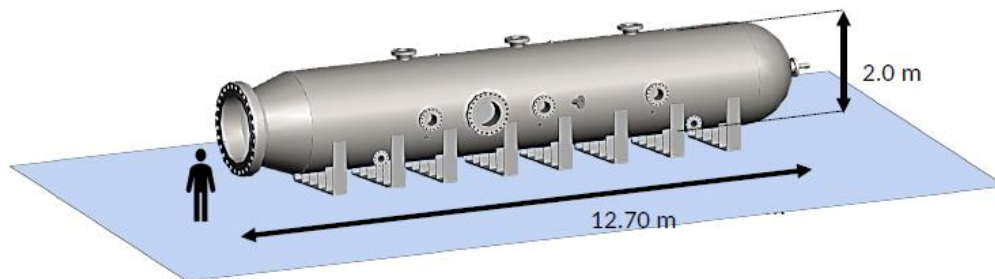
Figure 1: Princeton's Super-Tank Facility.
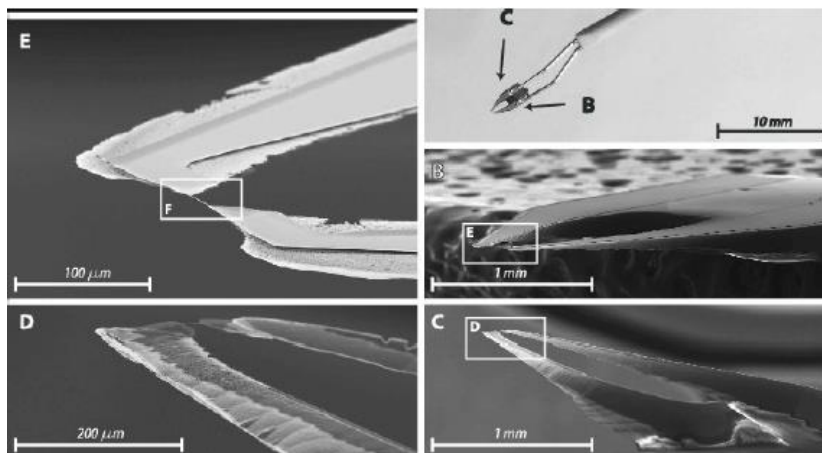
Figure 2: A NanoScale Thermal Anemometry Probe (NSTAP).

CITATIONS

- None

Researcher: **Anthony Harness**
Advisor: **N. Jeremy Kasdin (MAE)**
Sponsorship: **NASA, Jet Propulsion Laboratory (California Institute of Technology)**

Starshades are a promising technology to enable the direct detection and spectroscopic characterization of Earth-like exoplanets. Two key aspects to advancing starshade technology are the demonstration of starlight suppression at science-enabling levels and validation of optical models at this high level of suppression. The Princeton Starshade Testbed was designed to perform the sub-scale tests of starshades needed to experimentally validate the optical models at a flight-like Fresnel number. The starshade masks are lithographically etched in a Silicon wafer and coated with a thin metallic layer. PRISM facilities are used to characterize the as-built masks to high precision to enable validation between experimental results and optical models. The facilities also provide the opportunity to explore additional manufacturing techniques that will enable the masks to be manufactured to the required tolerances.
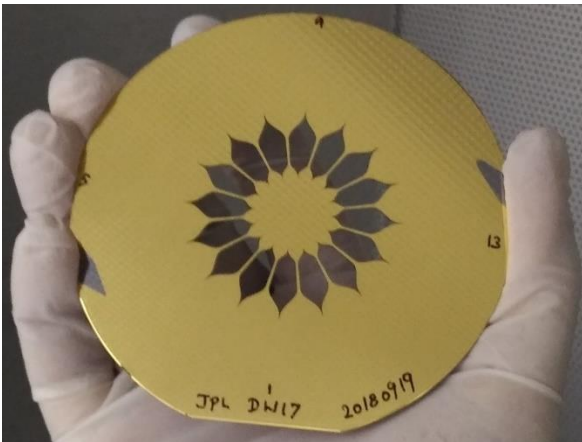
Figure 1: Starshade mask manufactured at the Microdevices Laboratory at JPL. The pattern etched through the Silicon wafer controls the diffraction of light to create a dark shadow; suppressing laser light by 9 orders of magnitude.

Figure 2: Princeton Starshade Testbed located on campus. This 80 meter long, 1 meter diameter tube provides a clean and dark environment for conducting optical tests on the starshade masks. Data from this experiment are used to validate optical models predicting the starshade's starlight suppression capabilities.

CITATIONS

➢ A. Harness, et al., Demonstration of 1e-10 contrast at the inner working angle of a starshade in broadband light and at a flight-like Fresnel number, Proc. SPIE 11117, 0L (2019).
➢ Y. Kim, A. Harness, N. J. Kasdin, et al., Optical demonstration of a starshade at flight Fresnel numbers in the laboratory, Proc. SPIE 10400, 43 (2017).
➢ K. Balasubramanian, et al., Recent progress in the fabrication of starshade masks for laboratory demonstration of concepts, Proc. SPIE 10698, 224 (2018).
➢ M. Galvin, Y. Kim, N. J. Kasdin, et al., Design and construction of a 76m long-travel laser enclosure for a space occulter testbed, Proc. SPIE 9912, 18 (2016).

Researcher: **Niki Abbasi**
Advisor: **Howard A. Stone (MAE)**
Sponsorship: **NSF**

We are studying dynamic equilibrium process of an aqueous two-phase system (ATPS), within a microfluidic device. ATPS are a mixture of two different polymeric solutions (or a mixture of a polymer solution and a salt solution), which phase separate and de-mix under certain conditions. Recently, Aqueous two-phase systems have been utilized instead of traditional water-in-oil systems for droplet generation. Some of the advantages of these systems, compared to traditional water-in-oil systems, are: 1- the slow growth of Rayleigh-Plateau instability, which allows for generation of a stable jet, making it ideal for fiber formation systems and 2-dynamic phase separation process.

Typically, ATPS are used when the system has reached its equilibrium, i.e. the solutions introduced into microfluidic devices are in equilibrium. However, if the solutions that are out-of-equilibrium are introduced within a microfluidic device, the ATPS would undergo a liquid-liquid phase separation process. As a result of this dynamic process, microstructures are evolved. Careful tuning of the initial composition of the system, and the flow parameters within the microfluidic device allow for generation of microstructured fibers. The microfluidic device utilized for this project is similar to that of Perrazo *et al* [1], shown below.
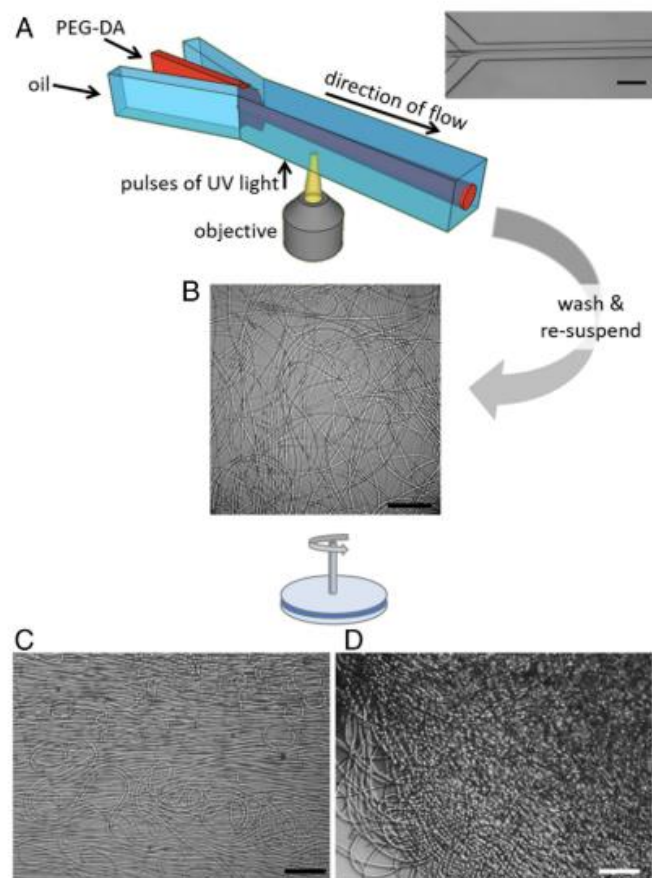
Figure 1: Figure adapted from the work of Perrazo et al. Schematic of the flow focusing microfluidic device, allowing for generation of a jet of PEGDa, surrounded by an oil phase and on-chip solidification of the chip based on UV polymerization.

CITATIONS

➤ [1] Perazzo, A., Nunes, J. K., Guido, S., & Stone, H. A. (2017). Flow-induced gelation of microfiber suspensions. *Proceedings of the National Academy of Sciences,* 114(41), E8557-E8564.

Researcher: **Ya Gai**
Advisor: **Howard A. Stone (MAE) and Sabine Petry (MOL)**
Sponsorship: **Princeton Catalysis Initiative**

The proliferation of eukaryotic cells relies on spindle assembly, which ensures the precise segregation of genetic materials during cell division. Central to the spindle assembly is the spatial organization of microtubules (MTs). Most in-vitro assays for studying MT organization were performed in test tubes where cell-sized confinement was missing. In-vivo, however, such organization must occur within cell boundaries. Therefore, we ask: can physical confinement affect the MT organization?

We used droplet microfluidics for encapsulating in-vitro MT assays in monodisperse droplets. In particular, we used soft lithography techniques to fabricate PDMS microchannels in the PRISM cleanroom. We found that both the droplet size and concentration of encapsulated biochemical components regulate the structure of MT networks. Our results highlight the prominent role of cell confinement in organizing MTs and might have direct implication on nucleation-controlled soft material processing.
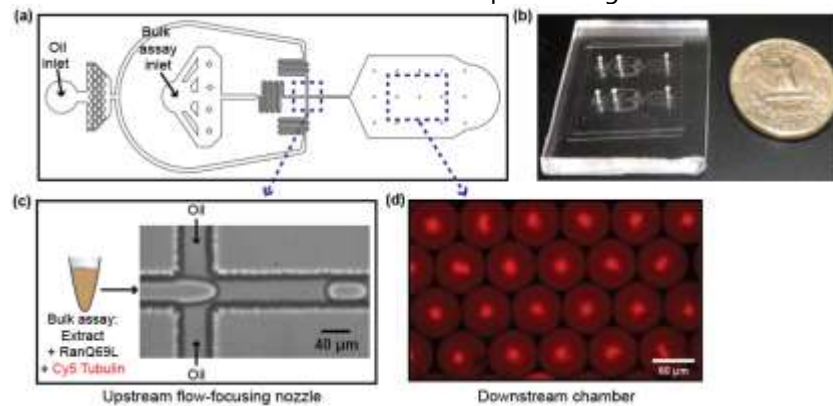
Figure 1: (a) A snapshot of microchannel design. (b) A picture of the microchannel fabricated in PRISM cleanroom. The blue dashed boxes in (a) highlight: (c) the upstream flow-focusing channel for generating monodisperse, extract-in-oil droplets; (d) the downstream chamber for collecting and imaging the droplets. (d) is a wide-field confocal image showing the structure of the MT network (red) in droplets.
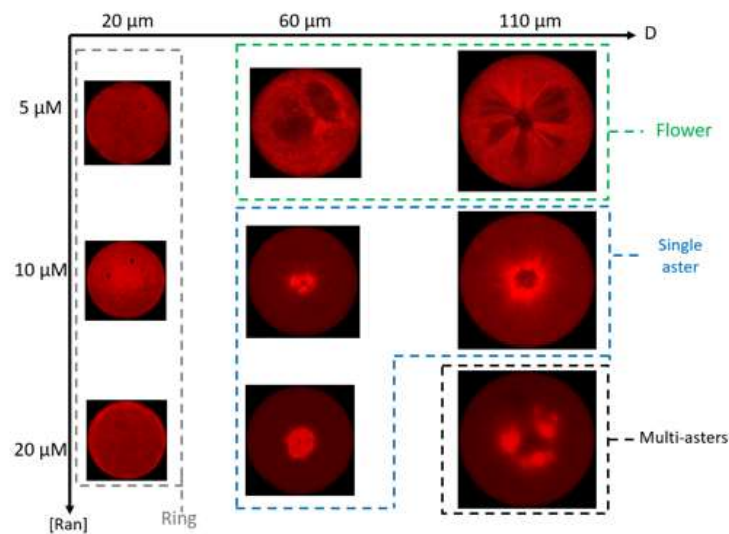
Figure 2: Regime maps summarizing the assembly of MT networks at time *t=14 min*. The horizontal axis denotes the droplet diameter *D*, and the vertical axis denotes the Ran concentrations *[Ran]*. The colored dashed boxes highlight different MT network architectures.

CITATIONS

➤ Ya Gai, Sagar Setru, Howard A. Stone, and Sabine Petry, "Confinement size determines the architecture of Ran-induced microtubule networks", in preparation for Biophysical Journal.60-63.

Researcher: **Suin Shim**
Advisor: **Howard A. Stone (MAE)**
Sponsorship: **NSF**

We investigate diffusiophoretic separation of negatively charged particles in a rectangular channel flow, driven by CO_2 dissolution from one wall. Since the negatively charged particles create an exclusion zone near the boundary where CO_2 is introduced, we model the problem by applying a shear flow approximation in a 2D configuration. From the form of the equations we define a similarity variable to transform the reaction-diffusion equations and particle distribution equations to ODEs.

The definition of the similarity variable suggests a characteristic length scale for the particle exclusion zone. We consider height averaged and different orientation of the flow behaviors in rectangular channels to rationalize and connect our experimental observations with the model. Our observations and the theoretical model provide design parameters such as flow rate, channel dimensions and CO_2 pressure for the in- flow water cleaning systems.
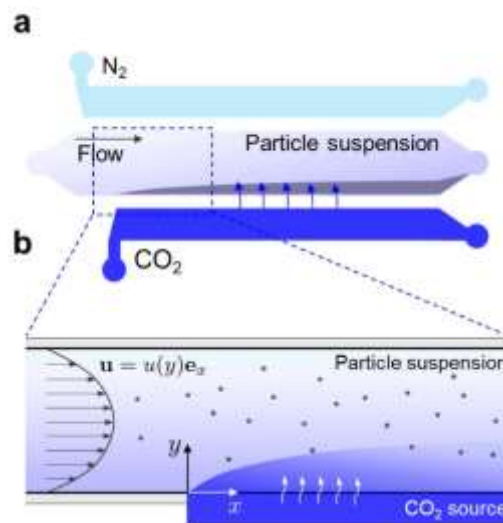
Figure 1: Schematic of CO_2 driven diffusiophoresis in a channel flow. (a) A particle exclusion zone is expected to form near the boundary, through which CO_2 enters the main channel. (b) A magnified view of the inlet of the channel. We study the diffusion of CO_2 to understand ion concentration gradient in the channel flow, which drives diffusiophoretic motion of charged particles.
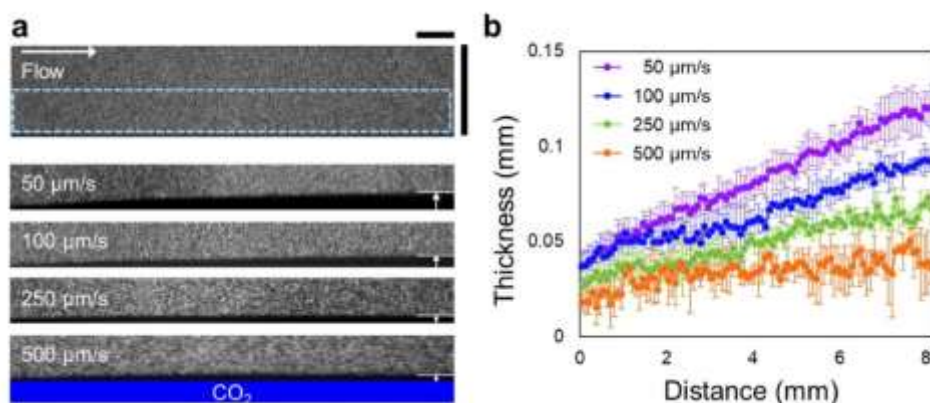
Figure 2: Effect of flow speed on the exclusion zone thickness. (a) Fluorescent images showing polystyrene particles flowing in the main channel and forming exclusion zones at different flow speeds. (b) Boundary of exclusion zone plotted versus distance along the channel.

CITATIONS

➤ O. Shardt, B. Rallabandi, S. Shim, S. Shin, P. B. Warren, and H. A. Stone, Driving diffusiophoresis by the dissolution gas under revision.

Researcher: **Malcolm Slutzky and Janine Nunes**
Advisor: **Howard A. Stone (MAE)**
Sponsorship: **NSF**

We characterize the production of hydrogel microfibers using continuous flow gelation with pulsed UV illumination. In this process, a photo-crosslinkable solution is focused into a uniform jet in a microfluidic device and exposed to UV light pulses, which converts the liquid jet into uniform cylindrical hydrogel segments. Precise control of the production of these uniform microfibers is achievable by understanding the relationships among process parameters (flow rate, UV intensity, solution composition, etc.), the reaction kinetics, and the fiber properties, such as length,

diameter and rigidity (Slutzky, 2019). These hydrogel microfibers are promising microscale soft materials for various applications. For example, suspensions containing high-aspect-ratio flexible hydrogel microfibers exhibit shear thickening. Such a property can be exploited to produce a biocompatible hydrogel by injecting the suspension from a standard needle and syringe without any chemical reactions (unlike a chemically cross-linked hydrogel) or chemical interactions (unlike a traditional physical hydrogel) (Perazzo, 2017).
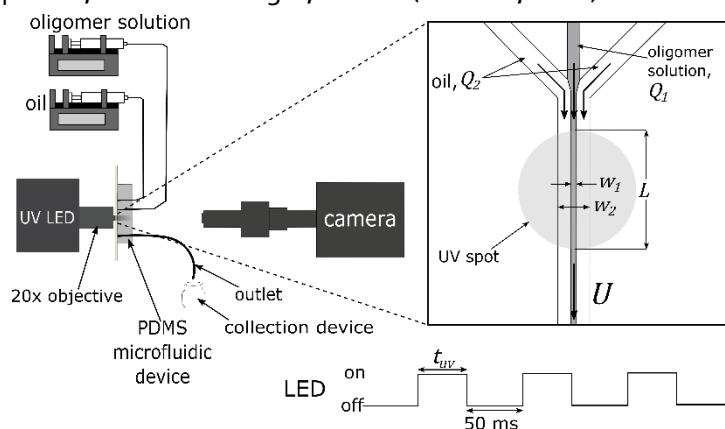
**Figure 1**: Illustration of the microfiber fabrication set-up, with the right inset panel showing a top view of the UV illumination section of the microfluidic device, where a jet of the oligomer solution flows with speed U in a UV light spot *L*.
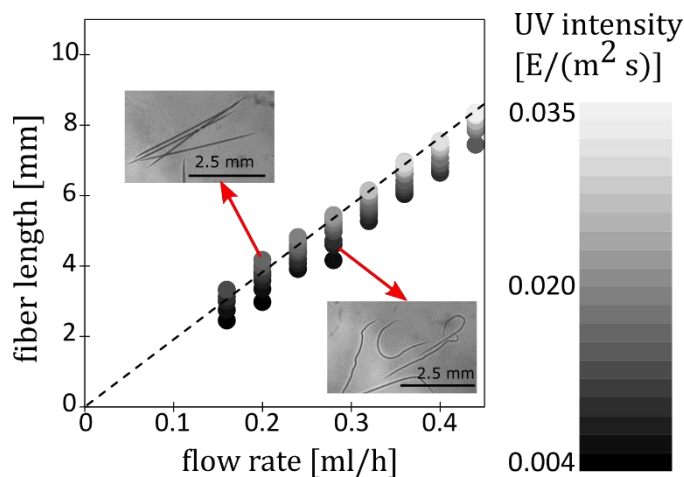
Figure 2: Graph showing the effect of oligomer flow rate and UV intensity on the fiber length. Inset images show the microfibers produced at the conditions indicated.

CITATIONS

➢ Perazzo, A.; Nunes, J. K.; Guido, S.; Stone, H. A. Flow-induced gelation of microfiber suspensions. Proc. Natl. Acad. Sci. U.S.A. 2017, 114, E8557-E8564.
➢ Slutzky, M.; Stone, H. A.; Nunes, J. K. A quantitative study of the effect of flow on the photopolymerization of fibers. Soft Matter. 2019, DOI: 10.1039/C9SM01485C.

Researcher: **Jessica Wilson**
Advisor: **Howard A. Stone (MAE)**
Sponsorship: **NSF**

We study the diffusiophoretic motion of negatively charged particles in one dimensional salt gradients using a dead-end pore geometry and various salt solutions. We estimate the diffusiophoretic velocities for particles for a range of background electrolytes such as multi-valent and asymmetric (non-z:z) electrolytes. Theoretical investigations of asymmetric electrolyte diffusiophoresis support our findings that the choice of electrolyte significantly influences the movement of particles, and in particular the chemiphoretic component of the diffusiophoretic velocity. By combining theoretical and experimental analysis, we present the relative importance of electrophoretic and chemiphoretic contributions in electrolyte solutions.

CITATIONS

➢ J. L. Wilson, S. Shim, Y. E. Yu, A. Gupta, and H. A. Stone. "Diffusiophoresis in Multivalent Electrolytes", *ACS Publications: Langmuir*. https://pubs.acs.org/doi/10.1021/acs.langmuir.9b03333.

Researcher: **Judy Yang**
Advisor: **Howard A. Stone (MAE)**
Sponsorship: **PEI**

The proposed research aims to characterize the influence of mineralogy, hydrology, and temperature on organic carbon content and microbial respiration rate in soils. The results will provide key constraints towards the development of accurate predictive models of soil carbon, the largest terrestrial carbon pool and a key, but poorly understood, feature of the Earth system. The proposed approach consists in developing a microfluidic model of an idealized soil (i.e., a soil on a chip) that will be used to examine the impact of hydrologic and mineralogical variables on carbon respiration rate.
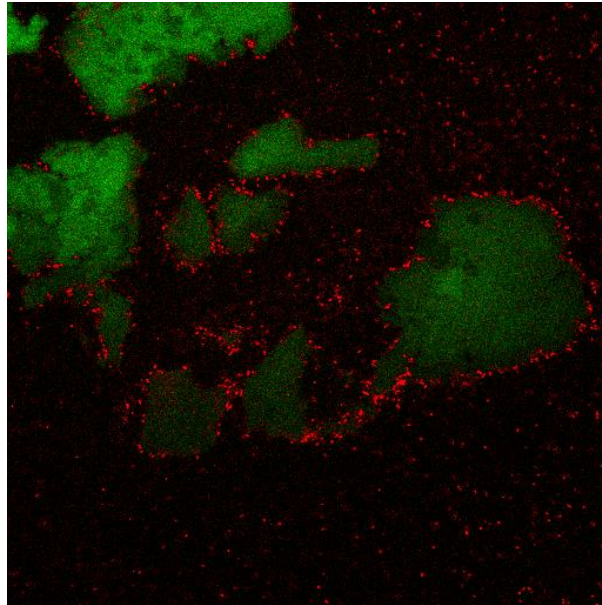
Figure 1: I am using microfluidics to visualize how bacteria interact with clays. Above is a confocal microscopy image showing how bacteria (labelled with red fluorescent protein) attach a clay with green organic matter absorbed.
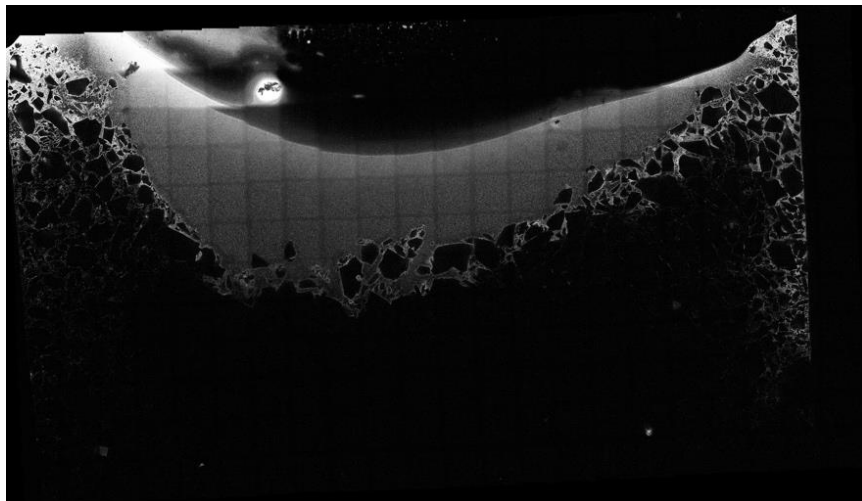
Figure 2: By incubating bacteria in a microfluidic device with transparent clays, I have found that clay cause bacteria to aggregate and slows down oxygen diffusion, and as such clay may reduce bacteria growth. Above is a confocal images showing that bacteria (indicated by white color) could not penetrate into the middle of the clay where there is a lack of oxygen.

CITATIONS

➢ This is a new pioneering project, so we do not have a publication yet

Researcher: **Salman Sohrabi**
Advisor: **Coleen T. Murphy (MOL)**
Sponsorship: **NIH**

Caenorhabditis elegans has a simple nervous system comprised of just 302 neurons. Learning and memory allow *C. elegans* to navigate, find food, and survive in a changing environment. *C. elegans* ability to associate nutritive states with chemical odors enabled creation of a positive olfactory learning paradigm. A standard population chemotaxis assay tests the worms' attraction to the odorant immediately or minutes to hours after conditioning. After synchronized day 1 hermaphrodites were starved for 1h, they will be transferred to OP50 seeded NGM plates and 2 μL of 10% butanone in ethanol on the lid and conditioned for 1hr. Trained population of worms then will be tested once for chemotaxis to butanone either immediately (0 h) or after being transferred to NGM plates with fresh OP50 for specified intervals before testing (30 min– 4 h). This manual assay is very laborious and extremely hard to master. It would take hours of preparation, testing and analyzing to get results of a STAM experiment. To overcome these limitations, our goal is to build a fully automated device to facilitate testing short-term associative memory (STAM) in *C. elegans*. Our platform comprised of four microfluidic chips, inter-connected system of valves, eight liquid reservoirs, motorized microscope stage, and worm counting software as demonstrated in Figure 1 and Figure 2. Each chip represent a time point which include four separate chambers providing four replica for each time-point. This fully automated platform can drastically expedite various researches related to memory such as Alzheimer's Disease mechanisms and potential treatment targets using C. elegans.

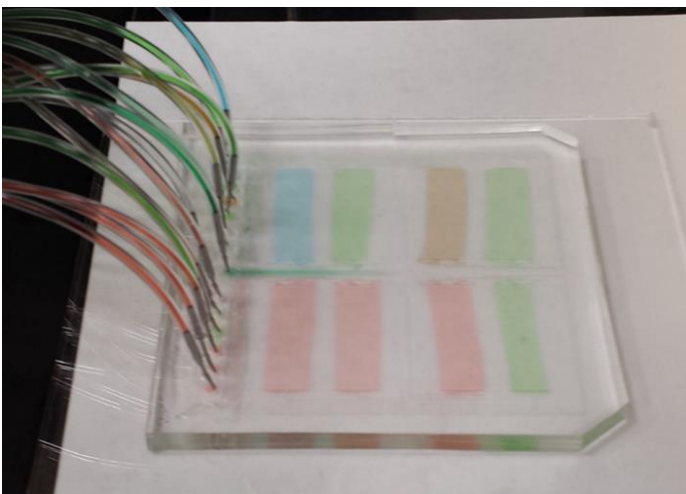
Figure 1: Each microfluidic chip represents a time point which include four separate chambers providing four replica for each time-point.

Figure 2: Device setup on a motorized microscope stage.

CITATIONS

➢ Princeton University

Researcher: **Brian Cook**
Advisor: **Sabine Petry (MOL)**
Sponsorship: **Princeton Catalysis Initiative**

We combine droplet microfluidics and cell-free biological systems to examine the effect of confinement and nucleation on the assembly of microtubule (MT) networks. Central to the spindle assembly is the spatial organization of MTs, a long tubular structure formed through the polymerization of tubulin dimmers. Such organization is regulated by RanGTP, a GTPase associated with chromosomal activities and acting as part of a major nucleation pathway for MTs. RanGTP has been explored using Xenopus egg extracts, a model cell-free system for probing spindle assembly. Most extract-based assays were performed in a test tube where cell-sized confinement was missing. Therefore, we asked whether confinement can affect the MT networks. We used droplet microfluidics for encapsulating extract-based assays by generating monodisperse, extract-in-oil droplets. By varying droplet diameters and encapsulated Ran concentrations, we demonstrate that these two physical factors regulate the assembly of MT networks. Together, the two factors yield MT networks with various steady-state architectures. Our results highlight the prominent role of MT nucleation in the self-organization of MTs in cell confinement and might have direct implications in nucleation-controlled soft material processing.
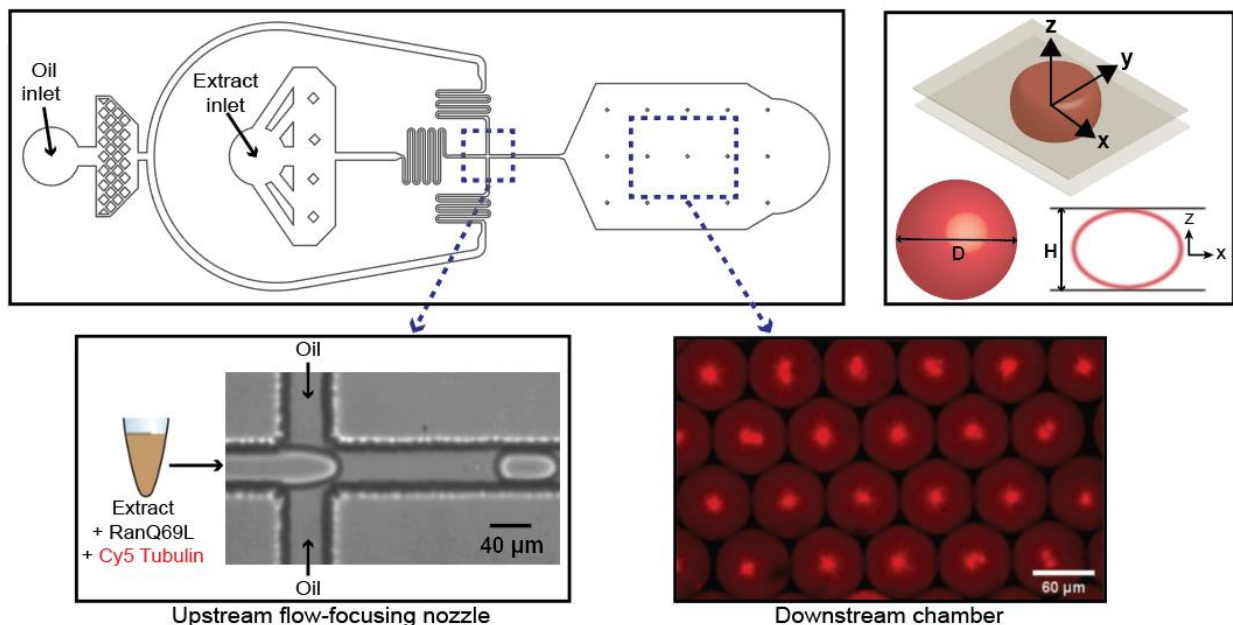
Figure 1: Encapsulation of *Xenopus* egg extract in oil droplets. (Top Left) Design of microfluidic device to encapsulate extract in oil. Top Right) Different design parameters effect droplet geometry. (Bottom Left) Image of flow-focusing nozzle generating oil droplets. (Bottom Right) Fluorescent microscopy images of biological components encapsulated in oil droplets.

CITATIONS

➢   Good, M. C., et al. Cytoplasmic Volume Modulates Spindle Size During Embryogenesis. Science, vol. 342, no. 6160, 2013, pp. 856 860.

Researcher: **Yimo Han**
Advisor: **Nieng Yan (MOL)**
Sponsorship: **Princeton University —Yan Lab**

Single particle cryogenic electron microscopy (cryo-EM) represents the cutting-edge technology for structural determination of bio-macromolecules. However, technical challenges associated with cryo-sample preparation limit cryo-EM from achieving higher resolution for broader range of targets. Here, we demonstrated a high yield, monolayer graphene supporting film improved the cryo-sample quality. Using this approach, we have achieved, so far, the highest resolution structure of the smallest protein by cryo-EM with the minimal number of datasets. Our technique paves the way for more general cryo-sample preparation for near-atomic resolution cryo-EM.
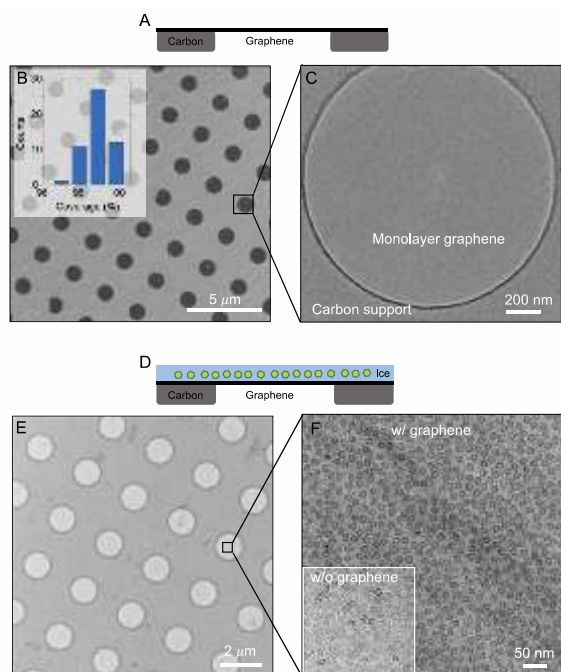
Figure 1: High yield graphene grids for cryo-EM. (A) Side-view schematic of graphene grids. (B) Large-scale SEM image of graphene film on holey carbon Quantifoil grids. The inset displays the statistics of graphene yield. (C) Zoomed-in TEM image of suspended graphene, showing its uniformity and cleanness. (D) Side-view schematic of cryo-EM sample on graphene grids. (E) Low-magnification image of a cryo-EM sample using graphene grids. (F) Cryo-EM micrograph of apoferritin on graphene grids, compared to the same sample on holey carbon grids (inset).
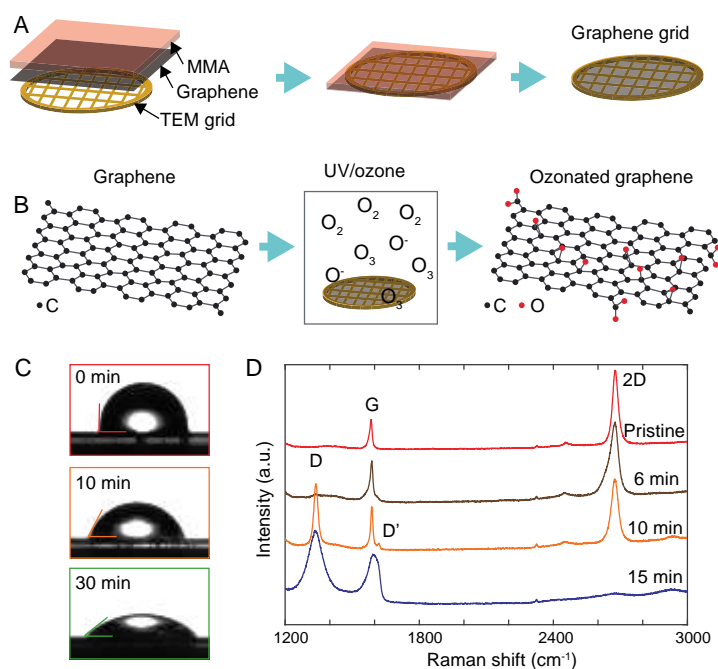
Figure 2: Fabrication of graphene cryo-EM grids. (A) Schematic summary of graphene grid fabrication process. (B) Schematic of surface treatment by UV irradiation. (C) Contact angle measurements showing that UV/ozone treatment increases the hydrophilicity. (D) Raman spectroscopy shows that 10-min UV/ozone treatment can convert graphene to oxygenated graphene by creating defects (indicated by the D peak in the orange curve). 15 min UV/ozone can effectively convert graphene into GO (blue curve).

CITATIONS

Y. Han et al. *PNAS* 2019 Dec 26, https://doi.org/10.1073/pnas.1919114117.

Researcher: **Mark Langstaff**
Advisor: **Cristiano Galbiati (PHY)**
Sponsorship: **NSF**

DarkSide-20k is a 30 tonne liquid argon time projection chamber that will search for galactic Weakly Interacting Massive Particles scattering from argon nuclei. The time projection chamber will be outfitted with over 10 square meters of silicon photomultiplier detectors sensitive to argon scintillation light. We are developing techniques for low-background die mounting suitable for cryogenic operation.
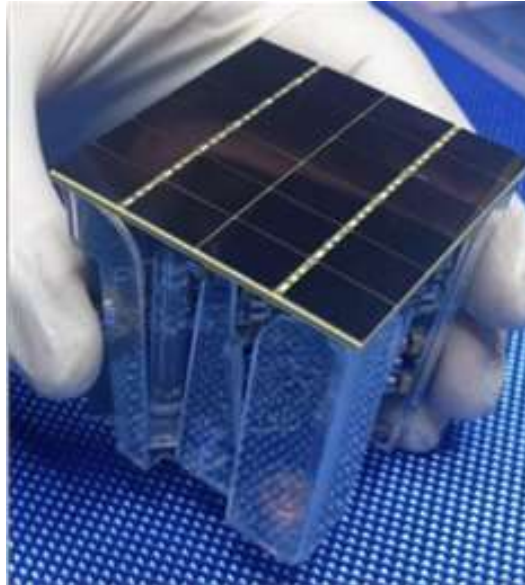
Figure 1: Completed SiPM based photodetector.
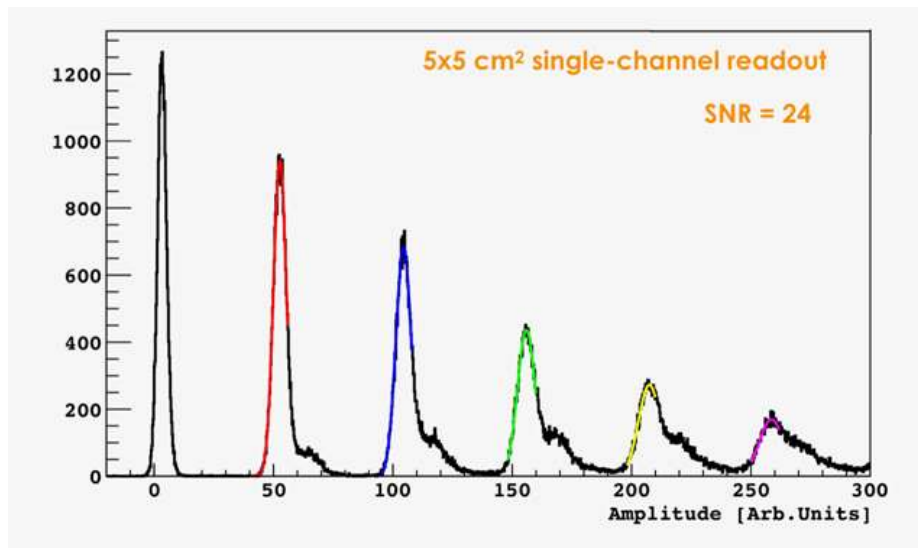
Figure 2: A photon spectrum collected with the SiPM based photodetector.

CITATIONS

➢ M. D Incecco et al., Development of a very low-noise cryogenic pre-amplifier for large-area SiPM devices, IEEE Trans. Nucl. Sci., vol. 65, no. 4 (2018).
➢ M. D Incecco et al., Development of a novel single-channel, 24 cm2, SiPM-based, cryogenic photodetector, IEEE Trans. Nucl. Sci., vol. 65 no. 1 (2018).
➢ C. E. Aalseth et al., Cryogenic Characterization of FBK RGB-HD SiPMs, J. Instrum. vol. 12 (2017).
➢ F. Acerbi et al., Cryogenic Characterization of FBK HD Near-UV Sensitive SiPMs, IEEE Trans. Electron Devices, vol. 64, no. 2 (2017).

Researcher: **Stephan Kim**
Advisor: **Nai Phuan Ong (PHY)**
Sponsorship: **MURI**

We study superconductivity of topological materials, such as Weyl semimetals, in order to discover and explore new physics.
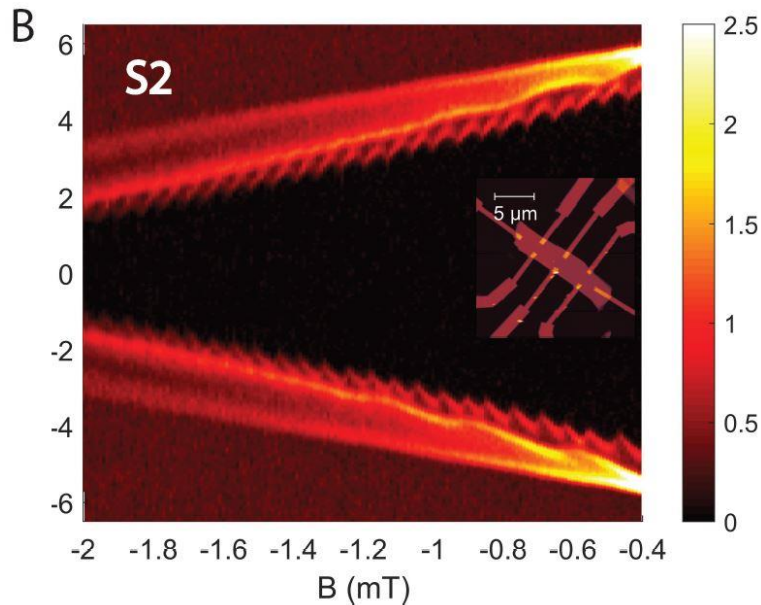
Figure 1: The periodic modulation of edge mode of MoTe2, which is the scalloped and fast oscillating mode. The period of the edge mode corresponds to the physical area of the sample that are not covered by gold electrodes. The insert is the atomic force microscope (AFM) image of the sample of interest.
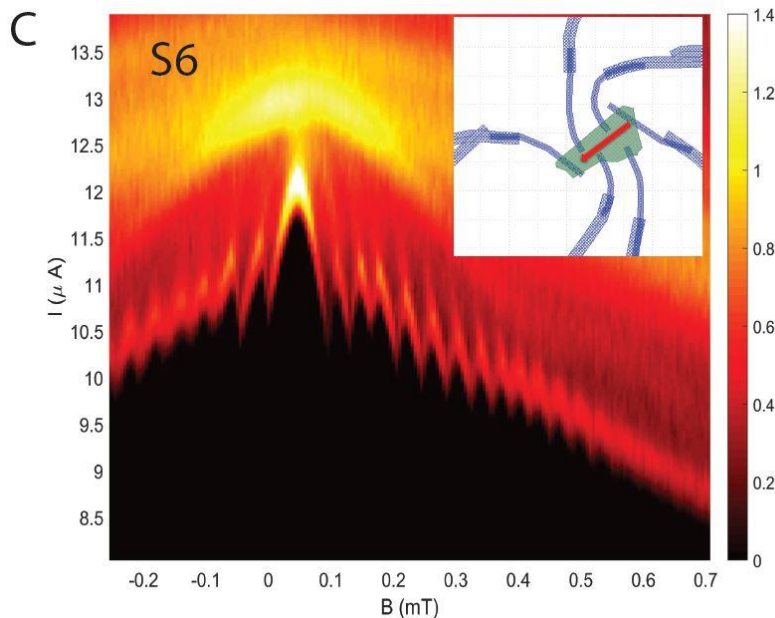
Figure 2: The periodic modulation of edge mode in a different MoTe2 sample. The period of oscillation also corresponds to the physical area of the sample, an evidence that the mode that results in the oscillation lies at the edge of sample.

CITATIONS

➢ Wudi Wang, Stephan Kim, Minhao Liu, F. A. Cevallos, R. J. Cava, N. P. Ong, *Observation of an edge supercurrent in the Weyl superconductor MoTe2* (2019), submitted to Science.

Researcher: **Nicholas Quirk**
Advisor: **Nai Phuan Ong (PHY)**
Sponsorship: **DOE**

I am studying the transport properties of topological semimetals that we machine into microscale lamellae using Focused Ion Beam microscopy (FIB) at the Imaging and Analysis Center (IAC). I have mainly been using the cleanroom to pattern electrodes onto substrates that I will use to make electrical devices in-situ in the FIB. I use the Raith e-line to define electrode patterns to make electrical contacts to these FIB-machined samples. I deposit the metals using the Oxford thermal evaporator.
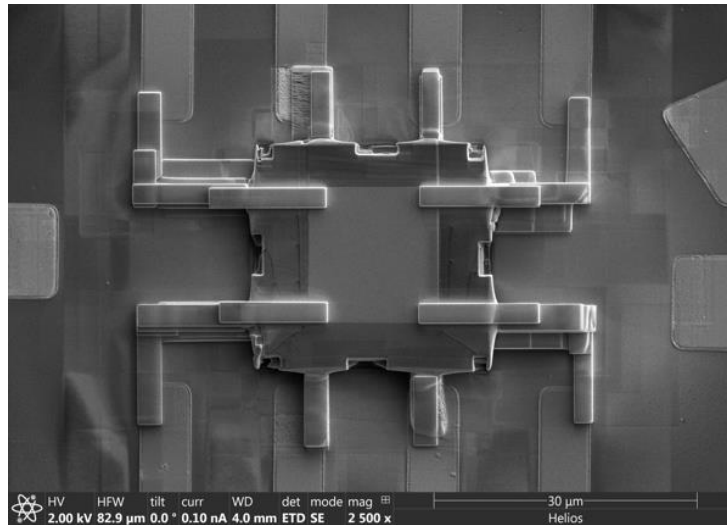
Figure 1: In the center of this image is a thin (1 μm-thick) lamella of a topological semimetal that we polished using FIB. The substrate is an Si/SiO$_2$ chip and the larger rectangles are Cr/Au electrodes that I patterned with photolithography techniques in the cleanroom.
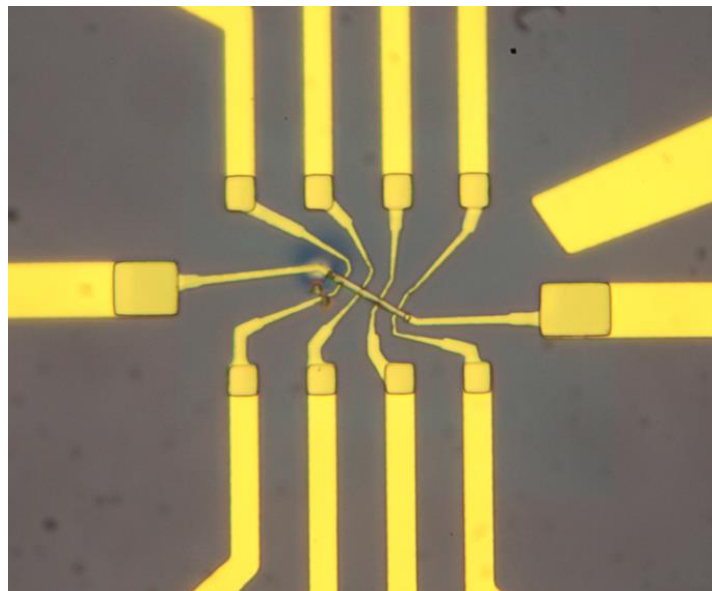

Figure 2: I placed a FIB-machined sample onto the same substrate as in Figure 1, but this time in lieu of the FIB-deposited Pt contacts I used thermal evaporation to make Ti/Au contacts that I patterned using e-beam lithography. The smaller electrode leads are these ebl-patterned contacts. In this way, I could make much smaller contacts and also not have to worry about over-exposing my sample with the ion beam.

CITATIONS

➢ None as of yet

Researcher: **Zheyi Zhu**
Advisor: **Nai Phuan Ong (PHY)**
Sponsorship: **DOE**

This project focuses on the transport properties of topological material. This includes making devices with exfoliated crystal of quantum spin liquid candidates, preparing substrates for experiments involving 3D topological insulators and Weyl/Dirac semimetals, and more.

CITATIONS
➢ N/A

Researcher: **Sarah Marie Bruno**
Advisor: **Suzanne T. Staggs (PHY)**
Sponsorship: **Simons Foundation**

The Simons Observatory (SO) is a new CMB experiment in its research and development stage. It will consist of several high-sensitivity polarization sensitive telescopes near the ACT site in Chile. The telescopes comprising SO will include a 6m primary large aperture cross-Dragone telescope coupled to a 2.4m diameter Large Aperture Telescope Receiver (LATR) as well as an array of 0.5m-primary cameras observing at large angular scales in frequency bands between 27 GHz and 270 GHz. SO is designed to measure the temperature and polarization of the Cosmic Microwave Background (CMB), the thermal radiation remaining from the Big Bang after billions of years of expansion. Today, the CMB is an extremely uniform ~2.7K microwave source filling the universe. We aim to constrain cosmological parameters and hope to detect evidence of primordial gravitational waves in the CMB polarization map across the celestial sphere. To accomplish these ambitious goals, we must build an instrument with extremely high sensitivity.
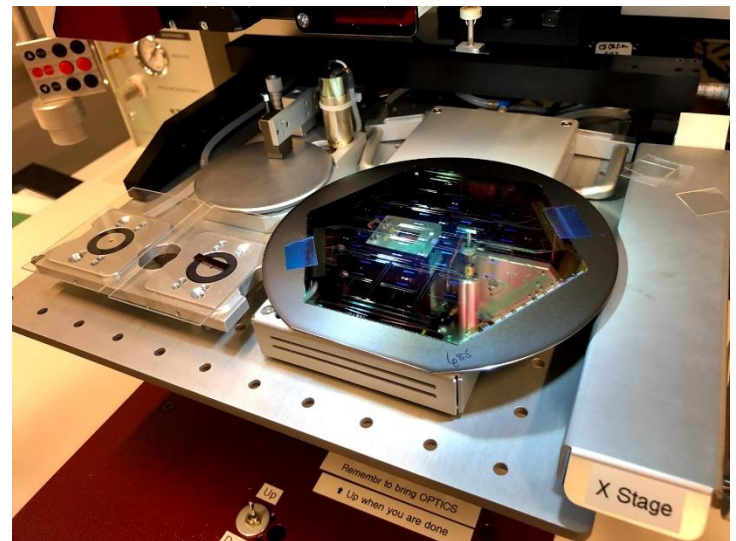

Figure 1: Example of a silicon wafer fabricated at the PRISM cleanroom used for mechanical validation of prototype designs of the Simons Observatory detector and readout wafer stack.

Figure 2: Multiplexing (MUX) chips are die bonded onto a readout wafer using the Tresky Flip Chip Bonder in the PRISM packaging lab.

CITATIONS

➤ https://arxiv.org/abs/1808.07445

➤ https://arxiv.org/abs/1710.04326

➤ Cooldown Strategies and Transient Thermal Simulations for the Simons Observatory, Coppi et al SPIE: https://www.spiedigitallibrary.org/conference-proceedings-of-spie/10708/2312679/Cooldown-strategies-and-transient-thermal-simulations-for-the-Simons-Observatory/10.1117/12.2312679.full?SSO=1 ARXIV: https://arxiv.org/abs/1808.07896

➤ Studies of Systematic Uncertainties for Simons Observatory: Detector Array Effects, Crowley et al SPIE: https://www.spiedigitallibrary.org/conference-proceedings-of-spie/10708/107083Z/Studies- of-systematic-uncertainties-for-Simons-Observatory--detector-array/10.1117/12.2313414.full ARXIV: https://arxiv.org/abs/1808.10491

➤ Cold optical design for the large aperture Simons Observatory telescope, Dicker et al SPIE: https://www.spiedigitallibrary.org/conference-proceedings-of-spie/10700/107003E/Cold-optical-design-for-the-large-aperture-Simons-Observatory-telescope/10.1117/12.2313444.full ARXIV: http://arxiv.org/abs/1808.05058

➤ The Simons Observatory: Instrument Overview, Galitzki et al SPIE: https://www.spiedigitallibrary.org/conference-proceedings-of-spie/10708/1070804/The-Simons- Observatory-instrument-overview/10.1117/12.2312985.full ARXIV: https://arxiv.org/abs/1808.04493

➤ Studies of Systematic Uncertainties for Simons Observatory: Optical Effects and Sensitivity Considerations, Gallardo et a SPIE: https://www.spiedigitallibrary.org/conference-proceedings-of-spie/10708/107083Y/Systematic-uncertainties-in-the-Simons-Observatory--optical-effects-and/10.1117/12.2312971.full?SSO=1 ARXIV: https://arxiv.org/abs/1808.05152

➤ BoloCalc: a sensitivity calculator for the design of Simons Observatory, Hill et al SPIE: http://spie.org/Publications/Proceedings/Paper/10.1117/12.2313916 ARXIV: https://arxiv.org/abs/1806.04316

➤ Simons Observatory large aperture receiver simulation overview, Orlowski-Scherer et al SPIE: https://www.spiedigitallibrary.org/conference-proceedings-of-spie/10708/107083X/Simons-Observatory-large-aperture-receiver-simulation- overview/10.1117/12.2312868.short ARXIV: https://arxiv.org/abs/1808.06648

➤ Studies of Systematic Uncertainties for Simons Observatory: Polarization Modulator Related Effects, Salatino et al SPIE: https://www.spiedigitallibrary.org/conference-proceedings-of-spie/10708/1070848/Studies-of-systematic-uncertainties-for-Simons-Observatory--polarization- modulator/10.1117/12.2312993.short?SSO=1 ARXIV: http://arxiv.org/abs/1808.07442

➤ Feedhorn development and scalability for Simons Observatory and beyond, Simon et al SPIE: https://www.spiedigitallibrary.org/conference-proceedings-of-spie/10708/2313405/Feedhorn-development-and-scalability-for-Simons-Observatory-and-beyond/10.1117/12.2313405.full?SSO=1 ARXIV: https://arxiv.org/abs/1809.07373

➤ Simons Observatory Large Aperture Telescope Receiver Design Overview, Zhu et al SPIE: https://spie.org/Publications/Proceedings/Paper/10.1117/12.2312871 ARXIV: https://arxiv.org/abs/1808.10037

➤ Magnetic Sensitivity of AlMn TESes and Shielding Considerations for Next Generation CMB Surveys - LTD 2017 Proceedings ARXIV: https://arxiv.org/abs/1710.08456

Researcher: **Martina Macakova**
Advisor: **Suzanne T. Staggs (PHY)**
Sponsorship: **Simons Foundation**

The Simons Observatory (SO) is a new cosmic microwave background experiment being built on Cerro Toco in Chile, due to begin observations in the early 2020s. We describe the scientific goals of the experiment, motivate the design, and forecast its performance. SO will measure the temperature and the polarization anisotropy of the cosmic microwave background in six frequency bands centered at: 27, 39, 93, 145, 225 and 280 GHz. The initial configuration of SO will have three small-aperture 0.5-m telescopes and one large-aperture 6-m telescope, with a total of 60,000 cryogenic bolometers. Our key science goals are to characterize the primordial perturbations, measure the number of relativistic species and the mass of neutrinos, test the deviations from a cosmological constant, improve our understanding of galaxy evolution, and constrain the duration of reionization.
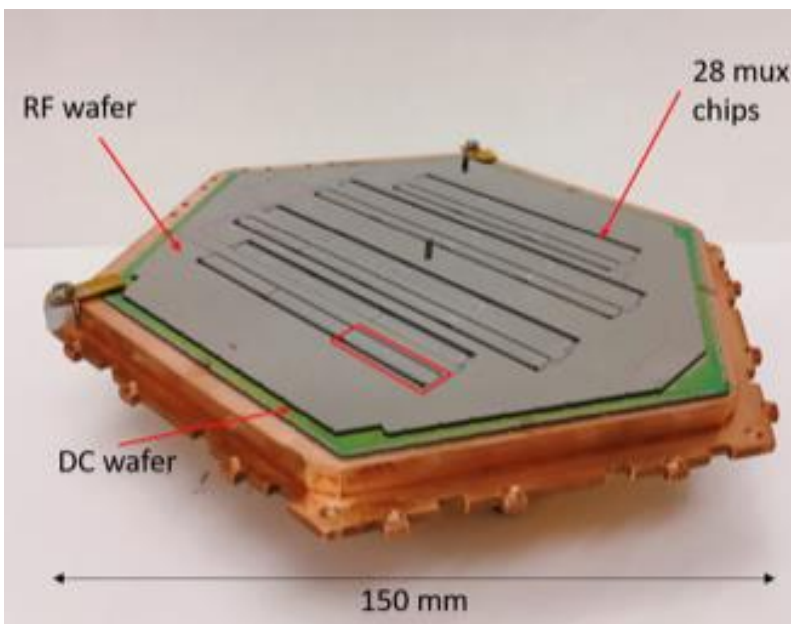
Figure 1: (left) Photograph of the prototype UMM. The 28 multiplexer chips are connected at the transmission and flux ramp lines by the RF wafer. The multiplexer chips and RF wafer sit on the DC wafer, which contains the TES bias circuitry. A single multiplexer chip is outlined in red.

Figure 2: (right) Photograph of the UMM assembled. The RF and DC connectors are mounted to the top of the package lid. The RF and DC flexible cables (flex) allow for the signals to enter away from sky-side.
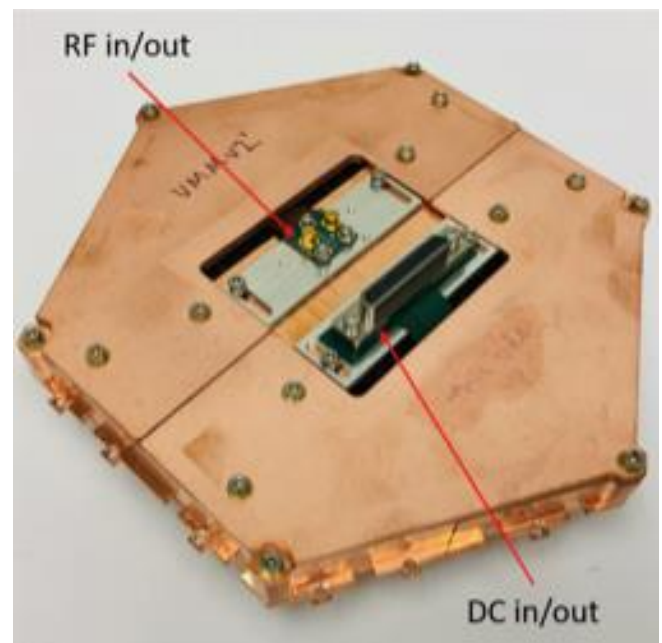
CITATIONS

➤ The Simons Observatory: Science goals and forecasts., The Simons Observatory Collaboration, arXiv: 1808.07445, 2018.

Researcher: **Fang Zhao**
Advisor: **Christopher G. Tully (PHY)**
Sponsorship: **Simons Foundation**

1. Graphene nanoribbon transistors with top and bottom gates are fabricated for the first time direct directional detection of MeV dark matter. The GNFET sensor has a tunable meV band gap, a full three orders of magnitude smaller than cryogenic germanium detectors. This sensitivity is used to switch on and off the conductivity of the GNFET channel by 10 orders of magnitude in charge carriers in response to the gate voltage shift from a single scattered electron. The width of GNs are from sub-10nm to 100nm. Single and ribbon array FETs will be fabricated for low temperature measurements.

2. Greyscale lens structure will be fabricated to coat on our photodetectors to increase the active area of dark matter detectors.

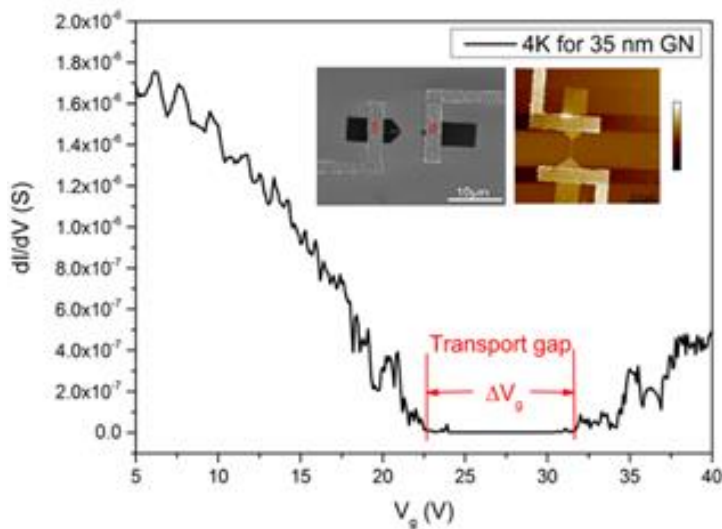**Figure 1:** dI/dV of a GNFET with W=35nm and L=2.5μm, plotted as a function of V_g. Right inset shows an SEM image and left inset shows an AFM image.
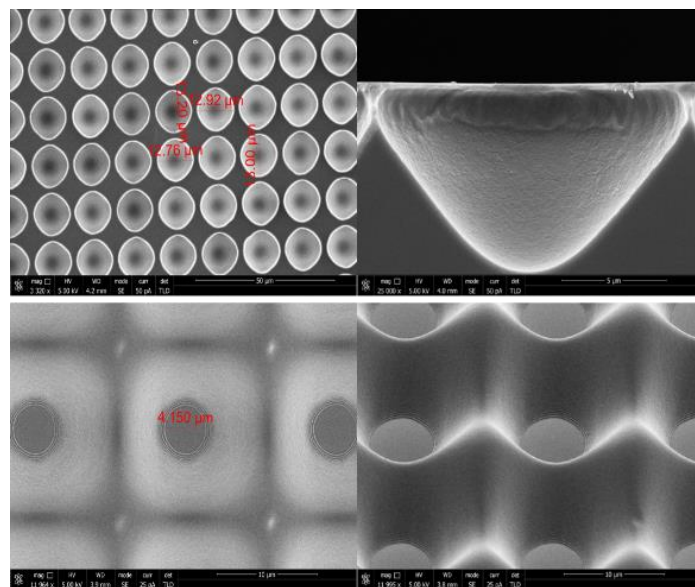
Figure 2: SEM images of lens and cone structure by greyscale lithography.

CITATIONS

➤ Have not published yet

Researcher: **Yanyu Jia**
Advisor: **Sanfeng Wu (PHY)**
Sponsorship: **Princeton Physics New Faculty Startup**

This project aims to fabricate quantum devices based on 2D materials, such as graphene, boron nitride and Tungsten ditelluride (WTe2), for quantum transport measurements. We will study the topological phases and novel superconducting states in these materials. To accomplish that, we will create nanoscale devices using equipment in MNFL, such as E-beam lithography, dry etch, metal evaporator and wire bonder.
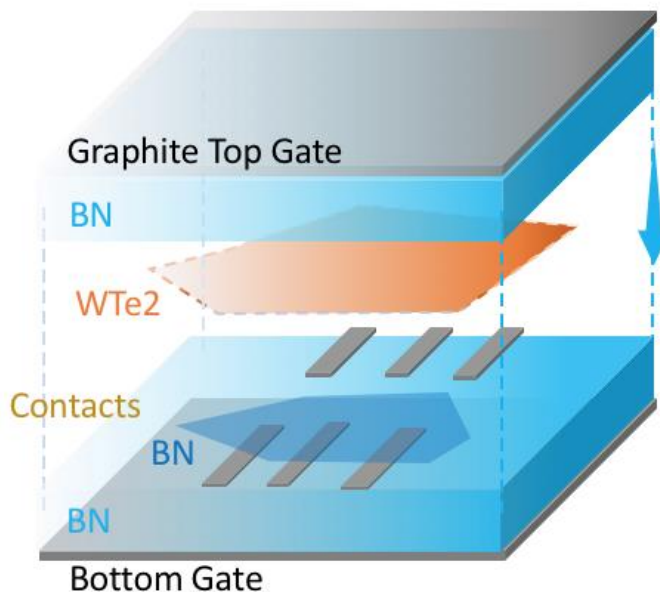
Figure 1: WTe2 Tunneling Device Design
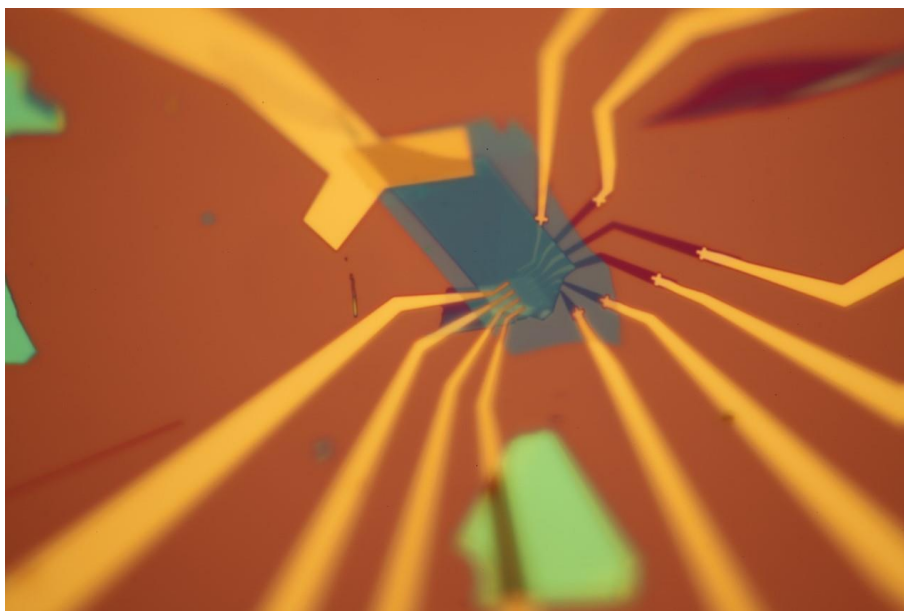
Figure 2: Bottom Pattern of Real Device

CITATIONS

➢   None

Researcher: **Mike Onyszczak**
Advisor: **Sanfeng Wu (PHY)**
Sponsorship: **Princeton Physics New Faculty Startup**

This project aims to fabricate quantum devices based on 2D materials, such as graphene, boron nitride, and transition metal dichalcogenides, for quantum transport measurements. We will study the interplay between the topological phases and novel superconducting states in these materials.
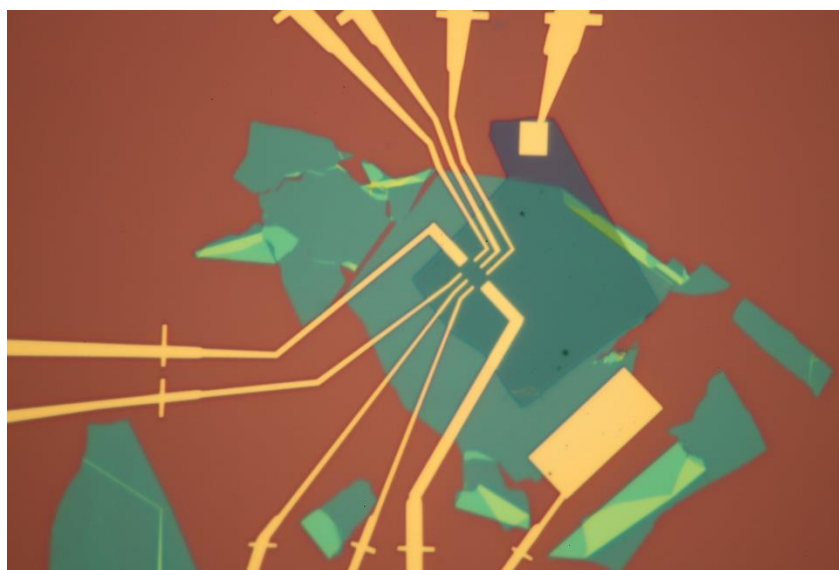
Figure 1: Bottom half of a nanodevice for measuring transport properties of 2D materials. Showing Au contacts deposited using the Angstrom Nexdep E-beam Evaporator.

- 2D Material
- Gold Contact
- Boron Nitride
- Graphite
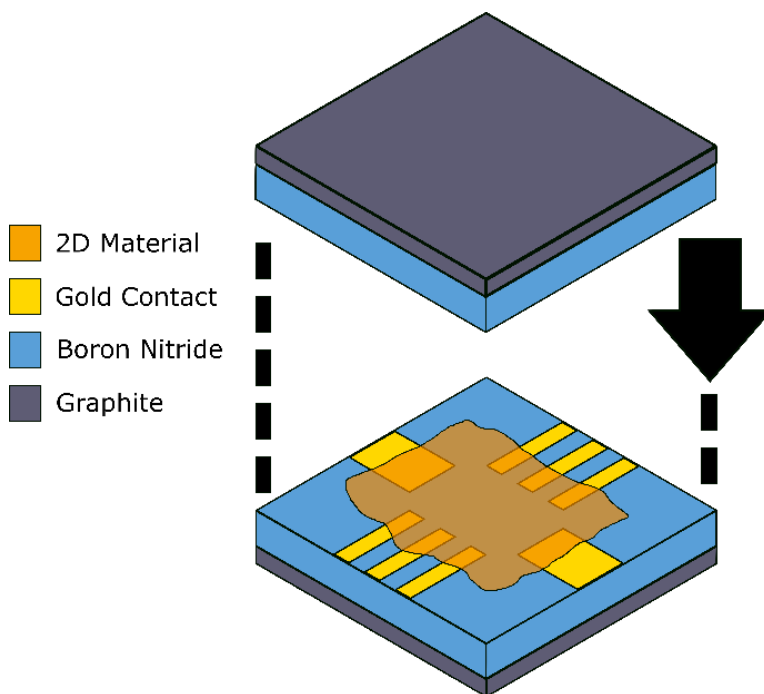
Figure 2: Cartoon representation of a typical nanodevice showing both the top and bottom gates for measuring transport properties such as resistivity and Hall voltage.

CITATIONS

- ➢ None

Researcher: **Pengjie Wang**
Advisor: **Sanfeng Wu (PHY)**
Sponsorship: **Princeton Physics New Faculty Startup**

This project aims to fabricate quantum devices based on 2D materials, such as graphene, boron nitride and Tungsten ditelluride (WTe2), for quantum transport measurements. We will study the topological phases and novel superconducting states in these materials. To accomplish that, we will create nanoscale devices using equipment in MNFL, such as E-beam lithography and metal evaporator.
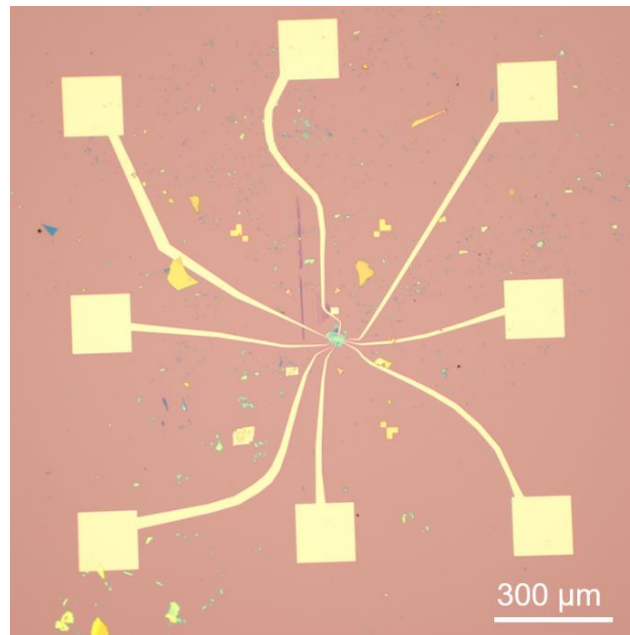

Figure 1: Overview of WTe$_2$ Device. The square pads are used for electrical connections to gates and contacts. The metal contacts are fabricated in PRISM cleanroom.
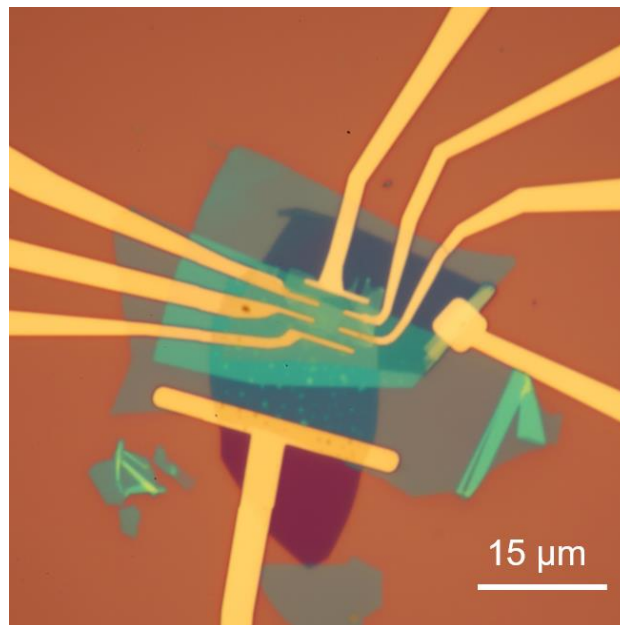
Figure 2: Zoom in of Figure 1. An hBN encapsulated WTe$_2$ Device with graphite top and bottom gate.

CITATIONS

- N/A

Researcher: **Guo Yu**
Advisor: **Sanfeng Wu (PHY)**
Sponsorship: **Princeton Physics New Faculty Startup**

This project aims to fabricate quantum devices based on 2D materials, including graphene, boron nitride (hBN) and Gadolinium tritelluride (GdTe3), for quantum transport measurements. We will study the novel electron states in these materials associated with their magnetic properties. To accomplish this, we will fabricate nanoscale devices using equipment in MNFL, such as E-beam lithography and metal evaporation.
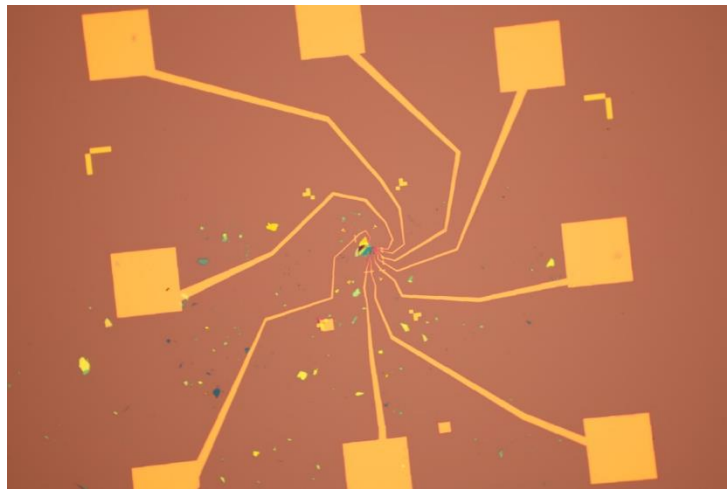
Figure 1: Optical image of a typical device under 5x objective, showing metal pads and electrode layout.

Figure 2: Optical image of same device under 100x objective, showing device geometry.

CITATIONS

➢ This is a new research topic so there is no previous publication

Researcher: **Cheng-Li Chiu**
Advisor: **Ali Yazdani (PHY)**
Sponsorship: **DOE**

In this project, we study the electronic structure of 2D heterostructures made by stacking van der Waal materials together. Because of the interlayer interaction between each layer, van der Waal heterostructures have very distinct electronic structure from its parent compound. Also, their properties are very tunable by electric dopin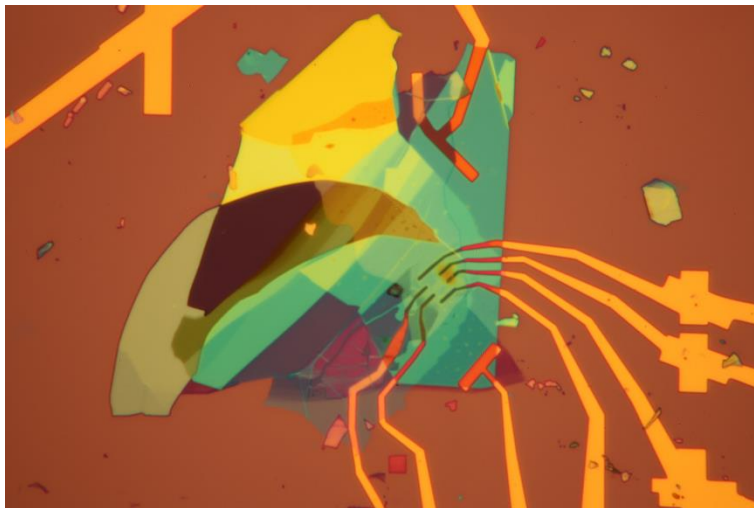g, displacement field and magnetic field. By tuning these physical nobs, several exotic quantum phenomena emerge. It has been shown that van der Waal heterostructures made by graphene or transition metal dichalcogenide can host superconductivity, correlated insulating state and ferromagnetism. Here we study van der Waal heterostructure by using scanning tunneling microscopy. We use microfabrication to making electric contact and bottom gate for our heterostructure. The contact is defined by optical lithography, and the gold is evaporated to create ohmic contact to our 2D material.
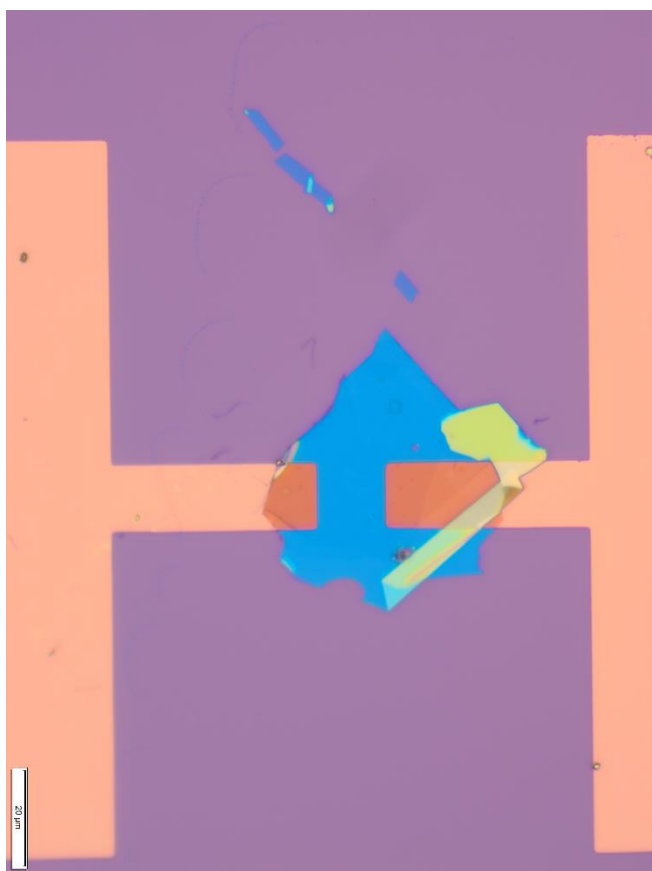
Figure 1: Optical image of a twisted bilayer graphene device, supported by hexagonal boron nitride. The contact is made in the clean room.
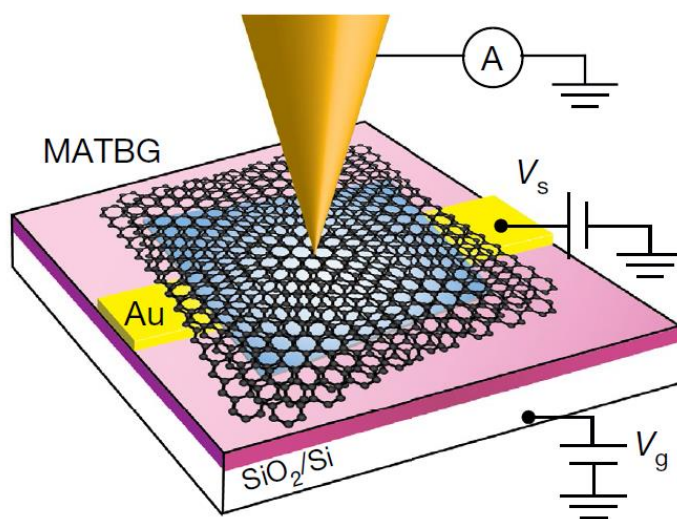
Figure 2: Schematic of our experimental setup. An atomic sharp tip is tunneling on a 2D heterostructure which is biased by gold contacts and gated by silicon underneath.

CITATIONS

➤ Xie, Y. et al. Spectroscopic signatures of many-body correlations in magic-angle twisted bilayer graphene. Nature 572, 101–105 (2019).

Researcher: **Gelareh Farahi**
Advisor: **Ali Yazdani (PHY)**
Sponsorship: **Exxon**

Inspired by the groundbreaking works on twisted bilayer graphene devices that exhibit unprecedented superconductivity, we are aiming to optimize the fabrication of pre-patterned devices of twisted bilayer transition metal dichalcogenide (TMD) WSe2 and studying emergent physical phenomena that occur by tweaking the electronic correlations through the twist angle. Due to their rich and yet complex unit lattice, twisted TMDs are theoretically predicted to host a vast variety of correlated and topological quantum states that could be utilized in fabricating a new generation of 2D devices.
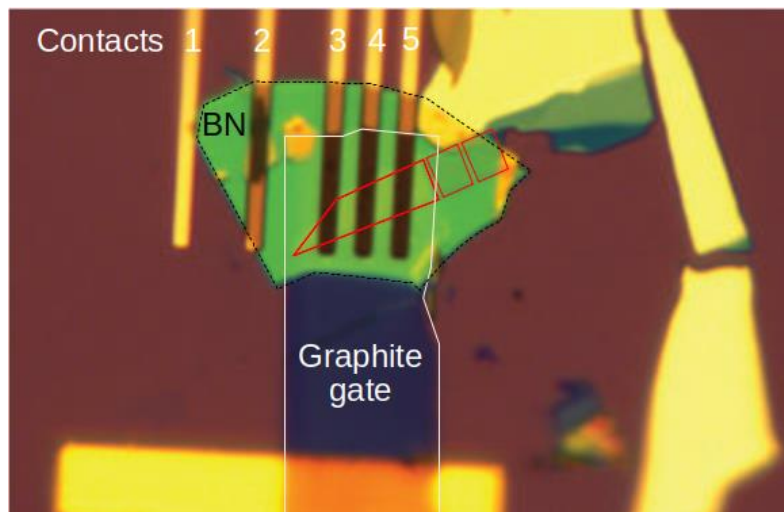
Figure 1: WSe2 bilayer (red boxes) on top of Pt contacts 3-5. The top Graphite gate (white solid line) is separated from the WSe2 flake by a 15 nm thin BN flake (black dashed line).
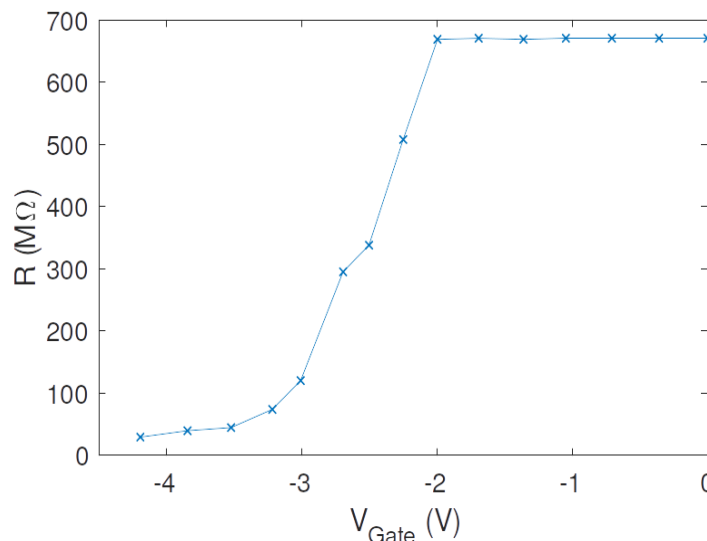
Figure 2: Contact resistance R of a representative test device as a function of applied gate voltage Vgate at room temperature.

CITATIONS

➢ Cao Y. et al. Unconventional superconductivity in magic-angle graphene superlattices. Nature 556, 43–50(2018).
➢ Wang L. et al. Magic continuum in twisted bilayer WSe2. arXiv:1910.12147(2019).

Researcher: **Brian Kraus**
Advisor: **Philip C. Efthimion (PPST)**
Sponsorship: **DOE through Lawrence Livermore National Library**

Short-pulse laser interactions with solid matter are small (microns), fast (picoseconds), hot (1 keV ~ 10^7 K) and complicated by relativistic electron kinetics, strongly-coupled plasma dynamics, and collisional atomic physics. Therefore, the diagnosis of essential parameters in this growing field is still in its infancy. A primary tool for measuring temperature, density, velocity, and composition in laser-heated materials is through x-ray emission spectroscopy, since fine structure x-rays from highly-charged ions are both high-energy enough to escape dense conditions and also representative of plasma conditions at the location of emission. Because the conditions can vary enormously in space and time during each laser interaction, it is necessary to restrict the measured signal to a localized region for meaningful interpretation. One solution is to embed "tracer layers" inside laser targets. The PVD equipment in PRISM was essential for creating such layered targets, consisting of Ti and MnAl tracer layers sputtered onto Al foil substrates, and subsequently sputtered with a tamp layer of Al. The suite of targets included fine scans of tracer layer thickness (0–1 micron) and tamp layer thickness (0–4 micron), made possible by the load lock design on the Angstrom Metal Sputterer. When heated with a short-pulse laser, each buried tracer layer quickly heats to extreme conditions, ionizing to H-like (Ti^{21+}) or He-like (Mn^{23+}) and emitting thermal x-rays; comparison of x-rays from tracers under different Al tamps shows plasma conditions changing as a function of depth. Detailed studies of collisional-radiative physics, lineshapes, and high-energy-density opacity are ongoing, building on decades of high-resolution crystal spectroscopy experience on low-density plasmas at the Princeton Plasma Physics Laboratory. The project was awarded four weeks of beamtime at the Jupiter Laser Facility at Lawrence Livermore National Laboratory (Sept. 2018) and three weeks at the Advanced Laser for Extreme Photonics at Colorado State University through the new Department of Energy initiative, LaserNetUS (Oct. 2019).
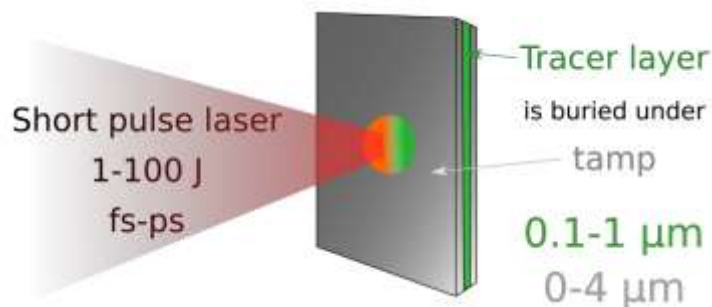

Figure 1: A cartoon showing the experimental setup with layered foil laser targets.
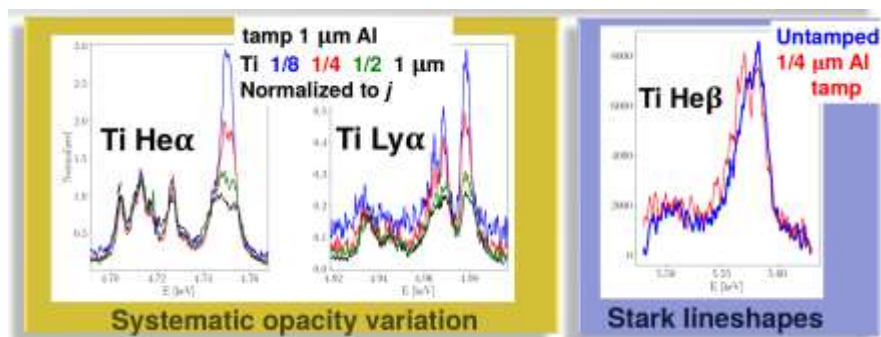

Figure 2: Two open areas of x-ray spectroscopy research are addressed by high-resolution x-ray spectroscopy measurements of precision-made layered targets.

CITATIONS

➤ (In preparation) Kraus, B. F., Gao, Lan, et al. "Plasma parameter profiles in short-pulse-heated solid targets" (2020).

II-VI, III-V SEMICONDUCTOR INTERSUBBAND DEVICES
Researcher: **Andres Correa Hernandez**
Advisor: **Claire F. Gmachl (ELE)**
Sponsorship: **NSF GRFP**

LATERAL TAILORING OF GAIN AND CURRENT PROFILE IN HIGH POWER EDGE EMITTING LASERS
Researcher: **Sara Kacmoli**
Advisor: **Claire F. Gmachl (ELE)**
Sponsorship: **Industrial**

QUANTUM OPTIMAL CONTROL
Researcher: **Zhaoqi Leng**
Advisor: **Andrew A. Houck (ELE)**
Sponsorship: **Industrial**

DEVELOPMENT OF NEW TRANSMON
Researcher: **Erik Porter**
Advisor: **Andrew A. Houck (ELE)**
Sponsorship: **ARMY**

TOP EMITTING PEROVSKITE LED
Researcher: **James Loy**
Advisor: **Barry P. Rand (ELE)**
Sponsorship: **AFOSR**

THz COUPLED OSCILLATOR ARRAYS
Researcher: **Hooman Saeidi**
Advisor: **Hoodman Saeidi (ELE)**
Sponsorship: **MURI**

PROGRAMMABLE TRANSMITTER SYSTEMS
Researcher: **Chandrakanth Reddy Chappidi**
Advisor: **Kaushik Sengupta (ELE)**
Sponsorship: **N/A**

VISITING RESEARCH SCHOLAR—MICROFAB OF MEMS AND/OR MICROFLUIDIC PLATFORMS
Researcher: **Mohamed Serry**
Advisor: **Kaushik Sengupta (ELE)**
Sponsorship: **SEAS**

TIME MODULATE ARRAY
Researcher: **Bingjun Tang**
Advisor: **Kaushik Sengupta (ELE)**
Sponsorship: **MURI**

INJECTION MOLDING: A COMPARISON OF MOLD MANUFACTURING TECHNIQUES FOR BOY 35E MACHINE
THz COUPLED OSCILLATOR ARRAYS
Researcher: **Nora Bradley**
Advisor: **Michael G. Littman (MAE)**
Sponsorship: **MAE Thesis Work**

ENGINEERING SPINDLE ASSEMBLY IN DROPLET MICROFLUIDICS
Researcher: **Syeda Ahmed**
Advisor: **Howard A. Stone (MAE)**
Sponsorship: **Princeton Catalysis Initiative**

A HOLOGRAPHIC LAB-ON-A-CHIP SYSTEM FOR THE LONG-TERM STUDY OF THE INTERPLAY AMONG
HYDRODYNAMICS, SURFACE CHEMISTRY, AND MICROBIOLOGY
Researcher: **Jiarong Hong**
Advisor: **Howard A. Stone (MAE)**
Sponsorship: **NSF**

WETTING AND MICROFLUIDICS
Researcher: **Amir Pahlavan**
Advisor: **Howard A. Stone (MAE)**
Sponsorship: **Industrial**

SIMONS OBSERVATORY
Researcher: **Yaqiong Li**
Advisor: **Suzanne T. Staggs (PHY)**
Sponsorship: **Simons Foundation**

VISUALIZING UNCONVENTIONAL SUPERCONDUCTIVITY IN TWISTED BILAYER GRAPHENE
Researcher: **Kevin Nuckolls**
Advisor: **Ali Yazdani (PHY)**
Sponsorship: **DOE**

Average Index for this partial citation listing is: 15
This partial citation listing includes 32 citations

N. C. Davy, M. Sezen-Edmonds, J. Gao, X. Lin, A. Liu, N. Yao, A. Kahn, and Y.-L. Loo, "Pairing of Near-Ultraviolet Solar Cells with Electrochromic Windows for Smart Management of the Solar Spectrum", *Nature Energy* 2, 17104 (*2017*).

F. Zang, Z. Su, L. Zhou, K. Konduru, G. Kaplan, and S. Y. Chou, "Ultrasensitive Ebola Virus Antigen Sensing via 3D Nanoantenna Arrays", *Advanced Materials*, Vol. 31. Iss. 30 (2019).

B. C. Rose, D. Huang, Z.-H. Zhang, P. Stevenson, A. M. Tyryshkin, S. Sangtawesin, S. Srinivasan, L. Loudin, M. L. Markham, A. M. Edmonds, D. J. Twitchen, S. A. Lyon, and N. P. de Leon, "Observation of An Environmentally Insensitive Solid-State Spin Defect in Diamond", *Science,* Vol. 361, Iss. 6397, 60-63 (2018).

 Y. Zhang, W. Fan, A. Y. Song, D. L. Sivco, and C. F. Gmachl, "Optoelectronic Plasmonic Metamaterials with a Quantum Cascade Structure", *CLEO* (2018).

T. M. Hazard, A. Gyenis, A. Di Paolo, A. T. Asfaw, S. A. Lyon, A. Blais, and A. A. Houck, "Nanowire Superinductance Fluxonium Qubit", *Phys. Rev. Lett.* 122, 010504 (2019).

A. Gyenis, P. S. Mundada, A. Di Paolo, T. M. Hazard, X. You, D. I. Schuster, J. Koch, A. Blais, and A. A. Houck, "Experimental Realization of an Intrinsically Error-Protected Superconducting Qubit", *Quantum Physics* (2019).

A. N. Tait, T. Ferreira de Lima, M. A. Nahmias, H. B. Miller, H.-T. Peng, B. J. Shastri, and P. R. Prucnal, "Silicon Photonic Modulator Neuron", *Phys. Rev. Applied* 11, 064043 (2019).

K. Roh, L. Zhao, W. B. Gunnarsson, Z. Xiao, Y. Jia, N. C. Giebink, and B. P. Rand, "Widely Tunable, Room Temperature, Single-Mode Lasing Operation from Mixed-Halide Perovskite Thin Films", *ACS Photonics* 6, 12, 3331-3337 (2019).

H. Kim, K. Roh, J. P. Murphy, L. Zhao, W. B. Gunnarsson, E. Longhi, S. Barlow, S. R. Marder, B. P. Rand, and N. C. Giebink, "Optically Pumped Lasing from Hybrid Perovskite Light-Emitting Diodes", *Advanced Optical Materials*, Vol. 8, Iss. 1 (2019).

X. Lu, S. Venkatesh, B. Tang, and K. Sengupta, "Space-Time Modulated 71-to-76GHz mm-Wave Transmitter Array for Physically Secure Directional Wireless Links" *IEEE ISSCC* (2020).

C. Zhu, L. Hong, H. Yang, and K. Sengupta, "Ingestible Bioelectronics: A Packaged, Bio-Molecular, Fluorescence-Based Sensor Array with Ultra-Low-Power Wireless Interface", *IEEE* (2019).

Md. S. Hossain, M. K. Ma, M. A. Mueed, D. Kamburov, L. N. Pfeiffer, K. W. West, K. W. Baldwin, R. Winkler, and M. Shayegan, "Geometric Resonance of Four-Flux Composite Fermions", *Phys. Rev. B*100, 041112(R) (2019).

L. E. Aygun, P. Kumar, Z. Zheng, T.-S. Chen, S. Wagner, J. C. Sturm, and N. Verma, "17.3 Hybrid System for Efficient LAE-CMOS Interfacing in Large-Scale Tactile-Sensing Skins via TFT-Based Compressed Sensing", *IEEE* (2019).

M. Ozatay, L. Aygun, H. Jia, P. Kumar, Y. Mehlman, C. Wu, S. Wagner, J. C. Sturm, and N. Verma, "Artificial Intelligence Meets Large-Scale Sensing: Using Large-Area Electronics (LAE) to Enable Intelligent Spaces", *IEEE* (2018).

Y. Mehlman, P. Kumar, M. Ozatay, S. Wagner, J. C. Sturm, and N. Verma, "Large-Area Electronics HF RFID Reader Array for Object-Detecting Smart Surfaces", *IEEE* (2018).

Y. Mehlman, C. Wu, S. Wagner, J. C. Sturm, and N. Verma, "Gigahertz Zinc-Oxide TFT-Based Oscillators" *IEEE Device Research Conference* (2019).

L. E. Aygun, P. Kumar, Z. Zheng, T.-S. Chen, N. Verma, S. Wagner, J. C. Sturm, and N. Verma, "Hybrid System for Efficient LAE-CMOS Interfacing in Large-Scale Tactile-Sensing Skins via TFT-Based Compressed Sensing", *International Solid-State Circuits Conference*, 280-282 (2019).

J. C. Sturm, Y. Mehlman, L. E. Aygun, C. Wu, Z. Zheng, P. Kumar, S. Wagner, and N. Verma, "Machine Learning and High-Speed Circuitry in Thin Film Transistors for Sensor Interfacing in Hybrid Large-Area Electronic Systems", *ECS Transactions*, Vol. 92, Iss. 4, 121 (2019).

M. Raha, S. Chen, C. M. Phenicie, S. Ourari, A. M. Dibos, and J. D. Thompson, "Optical Quantum Nondemolition Measurement of Solid-State Spin without A Cycling Transition" (2019).

C. M. Phenicie, P. Stevenson, S. Welinski, B. C. Rose, A. T. Asfaw, R. J. Cava, S. A. Lyon, N. P. de Leon, and J. D. Thompson, "Narrow Optical Line Widths in Erbium Implanted in TiO_2", *Nano Lett*, Vol. 19, Iss. 12, 8928-8933 (2019).

C. P. Byers, M. K. Fu, Y. Fan, and M. Hultmark, "Development of Instrumentation for Measurements of Two Components of Velocity with a Single Sensing Element", *Measurement Science and Technology* (2018).

A. Harness, S. Shaklan, N. J. Kasdin, M. Galvin, P. Willems, K. Balasubramanian, V. White, K. Yee, R. Muller, P. Dumont, and S. Vuong, "Demonstration of 1e-10 Contrast at the Inner Working Angle of a Starshade in Broadband Light and at a Flight-Like Fresnel Number", *SPIE* 11117 (2019).

K. Balasubramanian, S. Shaklan, V. White, K. Yee, R. Muller, S. Velling, S. Vuong, A. Harness, and N. J. Kasdin, "Recent Progress in the Fabrication of Starshade Masks for Laboratory Demonstration of Concepts", *Proc. SPIE* 10698, 10698-224 (2018).

Y. Gai, H. A. Stone, and S. Petry, "Confinement Size Determines the Architecture of Ran-Induced Microtubule Networks" [in preparation].

M. Slutzky, H. A. Stone, and J. K. Nunes, "A Quantitative Study of the Effect of Flow on the Photopolymerization of Fibers", *Soft Matter*, Vol. 15, Iss. 46 (2019).

N. B. Lu, C. A. Browne, D. B. Amchin, J. K. Nunes, and S. S. Datta, "Controlling Capillary Fingering Using Pore Size Gradients in Disordered Media", *Phys. Rev. Fluid.* 4, 084303 (2019).

J. L. Wilson, S. Shim, Y. E. Yu, A. Gupta, and H. A.Stone, "Diffusiophoresis in Multivalent Electrolytes", *ACS Publications: Langmuir* (2020).

Y. Han, X. Fan, H. Wang, F. Zhao, C. G. Tully, J. Kong, N. Yao, and N. Yan, "High-Yield Monolayer Graphene Grids for Near-Atomic Resolution Cryoelectron Microscopy", *PNAS* (2019).

W. Wang, S. Kim, M. Liu, F. A. Cevallos, R. J. Cava, and N. P. Ong, "Observation of an Edge Supercurrent in the Weyl Superconductor MoTe2", *Physics* (2019).

Y. Xie, B. Lian, B. Jäck, X. Liu, C.-L. Chiu, K. Watanabe, T. Taniguchi, B. A. Bernevig, and A. Yazdani, "Spectroscopic Signatures of Many-Body Correlations in Magic-Angle Twisted Bilayer Graphene", *Nature* 572, 101-105 (2019).

B. F. Kraus, L. Gao, K. Hill, M. Bitter, P. Efthimion, M. Schneider, and H. Chen, "Plasma Parameter Profiles in Short-Pulse-Heated Solid Targets" (2020). [In preparation]

C. R. Chappidi and K. Sengupta, "A 26-42 GHz Broadband, Back-Off Efficient and VSWR Tolerant CMOS Power Amplifier Architecture for 5G Applications" *IEEE VLSI* (2019).